Alma Mater Studiorum · Università di Bologna

Scuola di Scienze
Dipartimento di Fisica e Astronomia
Corso di Laurea Magistrale in Fisica

MonteCarlo simulation of the XENON1T experiment and first comparison with the Muon Veto data.

Relatore:

Dott. Marco Selvi

Correlatore:

Dott. Marco Garbini

Presentata da:

Arianna Rocchetti

Anno Accademico 2016/2017

Sommario

L'esperimento XENON1T, in acquisizione dati presso i Laboratori Nazioni del Gran Sasso, è una Time Projection Chamber (TPC) contenente 2 t di xeno liquido ed ha come obiettivo una sensibilità per sezioni d'urto WIMP-nucleone indipendenti dallo spin pari a circa $1.6 \cdot 10^{-47}$ cm^2, per WIMP di massa 50 GeV/c^2, in 2 t·y. A tale scopo è fondamentale la riduzione di tutte le sorgenti di segnali di fondo. Per abbattere il fondo esterno la TPC è inserita all'interno di una vasca cilindrica riempita di acqua, dotata di 84 fotomoltiplicatori (PMT), che funge sia da schermo passivo contro la radiazione esterna (gamma e neutroni), sia da veto per i muoni grazie alla rivelazione della luce Čherenkov da essi prodotta in acqua. In questo lavoro presentiamo uno studio sulle configurazioni di trigger del sistema di veto di muoni e sulla sua efficienza. Lo studio è basato sul confronto di simulazioni Monte Carlo con i primi dati del rivelatore. Si ottiene un'efficienza del 99.5% per eventi di muone e del 43% per sciami generati da interazioni del muone nella roccia che circonda la sala sperimentale, e conseguentemente una riduzione degli eventi di background attesi nell'attuale run scientifico a $1.3 \cdot 10^{-3}$ eventi. È già previsto dalla collaborazione il futuro upgrade dell'esperimento: XENONnT. Uno studio sulle possibili geometrie della TPC di XENONnT è stato effettuato mediante simulazioni Monte Carlo. Tra le possibili migliorie apportabili a XENONnT vi è la sostituzione degli attuali sensori di luce con fotomoltiplicatori al silicio (SiPM). Le simulazioni mostrano che, mediante una copertura totale della TPC con i SiPM, si ha un aumento dell'efficienza nella collezione di luce (LCE) del 20%. La LCE è un parametro fondamentale per la rivelazione del segnale di luce (S1) nella TPC; in questa configurazione si raggiunge una soglia in energia per rinculi nucleari di circa 3 keV, aumentando in modo significativo la sensibilità dell'esperimento, in particolare per WIMP di piccola massa.

Abstract

The XENON project aims at direct detection of Dark Matter through the scattering of WIMPs off the xenon nuclei. It consists of a time projection chamber (TPC) filled with liquid xenon both as target and detection medium. The XENON1T detector, installed at the Laboratori Nazionali del Gran Sasso (LNGS), is currently in its first science run. It aims at a sensitivity to spin-independent cross sections of $1.6 \cdot 10^{-47}$ cm^2 for WIMP masses of 50 GeV/c^2 in 2 t·y exposure. For this purpose it requires a very low background level. An active system able to tag muons and muon-induced backgrounds is thus critical for this goal. A water Cherenkov detector, the **Muon Veto**, has been developed, equipped with 84 8-inch photomultipliers (PMT) and cladded with a reflective foil. We present a study of the Muon Veto rate for different trigger configurations and of the corresponding efficiencies. The study has been carried out comparing a Monte Carlo simulation with the data from the detector.

The muon veto will reach a very high detection efficiencies for muons (99.5%) and showers of secondary particles from muon interactions in the rock (43%), reducing the background in the current science run to $1.3 \cdot 10^{-3}$ events in 1 tonne fiducial volume.

A next generation detector, XENONnT, is already foreseen by the collaboration. It will have a larger TPC with an increased xenon target ($\sim 6\,t$) which will improve the WIMP sensitivity by another order of magnitude. In this work a preliminary study on the geometry of the XENONnT TPC was carried out, together with the analysis of a possible replacement of PMTs with Silicon PhotoMultipliers (SiPM).

Instrumenting also the lateral walls of the TPC, our study shows an increase of 20% in the light collection efficiency (LCE). The LCE is one of the crucial parameters for the detection of the light signal S1 in the TPC. We showed that with a 4π TPC coverage of SiPMs we can reach a energy threshold for nuclear recoil of about 3 keV, increasing significantly the capability to detect low mass WIMPs.

Contents

A Enrico, amico e fratello Scout.

Introduction

The Dark Matter (DM) quest is today one of the most challenging and intriguing open questions in physics. During the last century, early as the measurements of unexpected rotational velocities of the Coma galaxy cluster, we became aware that with the known physics we are able to explain only a minimum part of the whole Universe composition. Nowadays, the scientific community agrees that the ordinary matter can not account for the total mass content of the Universe. Starting from this open question, remarkable efforts have been directed towards the search for the so-called Dark Matter (DM). Indeed the number of experiments aimed at detecting Dark Matter has continuously grown in the last decades. One interesting and promising candidate is the so-called **WIMP** (**W**eakly **I**nteraction **M**assive **P**article), a new corpuscle interacting with ordinary matter only through gravitation and, we hope, weak interaction.

In Chapter 1, we review the status of the search for Dark Matter, along with the present state-of-art of experimental and theoretical achievements. We describe the astrophysical evidences, from both galactic and cosmological scales, which led to the belief in the Dark Matter existence. The composition of Dark Matter is still quite uncertain, even though there are strong indications for DM to be non-baryonic; several candidate particles have been proposed within different theoretical frameworks: Standard Model (SM) and theories beyond SM, such as SUSY and Extra dimensions. The experimental research follows basically two detection techniques: direct and indirect. The former aims at detecting scatterings of Dark Matter particles off target nuclei, while the indirect strategy relies on searching DM annihilation products. We provide a general overview of the current Dark Matter experiments and of their main results.

In Chapter 2, a particular focus is dedicated to the experiments of the XENON project. The current experiment is XENON1T, which is in data acquisition at the Laboratori Nazionali del Gran Sasso (LNGS) and aims at a sensitivity to spin-independent WIMP-nucleon cross sections of $1.6 \cdot 10^{-47}$ cm^2 for WIMP masses of 50 GeV/c^2, in 2 t·y.
XENON1T is dual phase Time Projection Chamber (TPC) filled with ultra-pure xenon in liquid phase (LXe), with a small gap of gaseous xenon (GXe) on the top of the TPC.

Xenon is an excellent scintillator medium, ideal to detect rare scattering events; the scintillation light is collected by two arrays of Photo Multiplier Tubes (PMTs) placed on the two opposite ends of the TPC. The interactions of particles in xenon produce also ionization; by applying an electric field the electrons can be drifted towards the gas region on the top, and here be extracted and accelerated to produce a second signal through proportional scintillation. This kind of technology has been demonstrated to be the most powerful in the direct search for Dark Matter. The interaction of DM with ordinary matter is characterized by a very small cross section; hence an extremely low background level is mandatory as well as a large target mass. The XENON1T experiment has been designed to fulfill both these two requirements.
XENON1T is equipped with an active system around it, able to tag muons and muon-induced backgrounds, the Muon Veto. It consists of a water Čherenkov detector of $\sim$ 10 m height and diameter, equipped with 84 8-inch photomultipliers and cladded by a reflective foil.

Chapter 3 is dedicated to the description of the Muon Veto system of the XENON1T experiment: a detailed description of its design, electronics and data processing is reported. We present a study pf the Muon Veto rate for different trigger configurations and of the correspondinf efficiencies. The study has been carried out with a series of Monte Carlo simulations described in the second part of Chapter 3. The last section of the third chapter is dedicated to the validation of the Muon Veto simulation against experimental data. Then we evaluated the Muon Veto tagging efficiency in the configuration of the Muon Veto used in the first science run of XENON1T. We also calculate the residual background due to muon-induced neutrons.

In Chapter 4, we describe the physical and electronic working principles of a silicon photomultiplier (SiPM). The SiPM addresses the challenge of detecting, timing and quantifying low-light signals down to the single-photon level. It offers a highly attractive alternative to PMTs offering all the benefits of a solid-state device: low voltage operation, lower sensitivity to electric fields, mechanical robustness and excellent uniformity of response. In the framework of the XENON collaboration, we started a study of the possible use of a SiPM as an alternative to the current technique for the light collection, which consists of two arrays of PMTs placed at the top and bottom of the TPC.

In Chapter 5 we study the Light Collection Efficiency (LCE) for different future possible configuration of a TPC instrumented with SiPMs. The LCE is defined as the fraction of emitted photons reaching the sensors. The study of the LCE has been performed with the GEANT4 software. We first study a configuration with SiPMs only in the bottom and top of the TPC and secondly a TPC with also a lateral coverage of SiPMs. The improved LCE is then translated in the capability to detect low energy nuclear recoil, lowering thus the energy threshold of the detector. The sensitivity, expressed as number of WIMP interactions above threshold, is then estimated.

The results achieved in this work are gathered in the conclusive chapter and discussed in the context of the whole scenario of direct Dark Matter search.

Chapter 1

The Dark Matter quest

Dark matter is hypotised to be an unidentified type of matter, comprising, in the observable universe, approximately the 27% of the mass and energy that is not accounted for by dark energy, baryonic matter (ordinary matter), and neutrinos. The name refers to the fact that it doesn't emit or interact with electromagnetic radiation, such as light, and is thus invisible to the entire electromagnetic spectrum.

Although dark matter has not been directly observed, first evidences for the Dark Matter (DM) existence came from F. Zwicky observations of the Coma and Virgo clusters. He found that the velocity of the galaxies were about one order of magnitude higher than the expected one, as if there were non luminous mass acting on the gravitational field.

Many hypotheses have been formulated about DM properties. Currently it seems that the most viable candidates for this kind of matter rise from extensions of the particle Standard Model (SM). Such candidates are grouped under the common name of Weakly Interacting Massive Particles (WIMPs) that already introduces some of their characteristics. Indeed, such matter has to have only gravitational and weak interactions, thus being 'Weakly Interacting', and it has to be massive, thus being made of 'Massive Particles'. The most quoted candidate as WIMP comes from the Supersymmetry: the neutralino. Several experiments have been realized in the last years aiming at the discovery of the Dark Matter. They are based on two different techniques: direct (interaction of the WIMP with ordinary matter) and indirect detection (measurement of the products of the annihilation of two WIMPs), both allowing to search and test different values for the theoretical parameters which define the DM properties.

Figure 1.1: The Coma Cluster, which provided the first evidence for Dark Matter. This image combines data from the Spitzer Space Telescope with the Sloan Digital Sky Survey to show many of the thousands of galaxies in the Coma cluster.

1.1 Dark Matter evidences

During his studies on the Coma Cluster [1], Fig. 1.1, Zwicky faced gravitational problems while he was trying to measure its mass. A cluster is a set of galaxies that move together inside their own gravitational field. The dynamics of such objects is very complex and usually there is not a real center around which the galaxies move. In order to measure the mass of the Coma cluster, Zwicky first determined the galaxy velocities inside of it, by measuring the Doppler effect of their spectra. After that, using the Virial Theorem, he was able to extract the gravitational force acting on each one of them and, finally, to obtain the mass of the system. Then, he measured the total light output of the cluster to determine the light to mass ratio. Comparing this value to the one from the nearby Kapteyn stellar system, he found a value for the Coma cluster that was 100 times lower compared to a single Kapteyn star.

Since Zwicky's results, other experimental observations showed a discrepancy with respect to what expected from a universe without the Dark Matter:

- anomalies in the rotational curves of spiral galaxies;
- observations of the Bullet Cluster;
- gravitational lensing effects;
- anisotropies in the Cosmological Microwave Background (CMB);

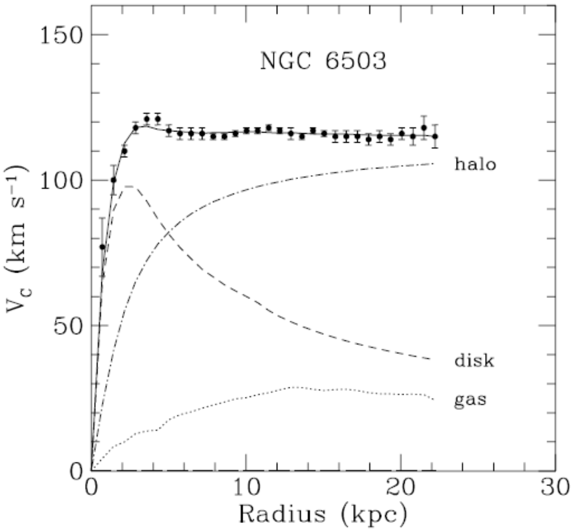

Figure 1.2: Velocity distribution of the dwarf spiral galaxy NGC 6503 [2], located in the region of space called the Local Void. The black dots are the observation results, while the dashed line is the expected shape from the only disk contribution. The contribution from the galaxy gas (dotted line) and halo (dash-dotted line) are also reported.

1.1.1 Galaxy scale evidences

Spiral galaxies, such as the Milky Way, are excellent probes to test the DM hypothesis. Such systems are said rotationally sustained since, for them, it is possible to define a clear rotational motion. To measure the velocity distribution until the edge of a galaxy, different techniques can be used depending on the used probe; for instance, the velocity of the hydrogen clouds is evaluated by measurements of the 21 cm line of the neutral hydrogen (HI), exploiting its low level of absorption in the interstellar medium. Usually, spiral galaxies are considered as made of a central core (disk+bulge), which is supposed to contain almost all the galaxy mass, and of an outer region. Their motion is described as a rigid body, hence, following the Newtonian gravitational law, the velocity distribution is given by

$$\frac{v^2(r)}{r} = G\frac{M(r)}{r^2} \qquad \rightarrow \qquad v(r) = \sqrt{G\frac{M(r)}{r}} \tag{1.1}$$

The mass can be obtained integranting the density in the sphere centered in the the center of the galaxy and of radius r

$$M(r) = 4\pi \int_0^r \rho(x) x^2 dx \tag{1.2}$$

where $\rho(x)$ is the density of visible matter in the galaxy. If we consider the mass as a function of the radius, $M(r)$, to be constant outside the core of the galaxy, we have

$$v(r) \propto \frac{1}{\sqrt{r}} \tag{1.3}$$

as predicted by the Newtonian theory. However, experimental data show that, outside the disk and much beyond, the velocity distribution no longer follows the expected behavior, but it remains constant (see Fig. 1.2). Such evidence points out the presence of matter (physical entity gravitationally interacting) characterized by a density that scales with the root square of the distance: $\rho \propto r^{1/2}$.
Such result is explained assuming that the spiral galaxies are enclosed in dark halos with a matter distribution that expands much beyond the distribution of the luminous matter and whose effect dominates in the outer region of the galaxies. One of the most popular density profile for the Dark Matter halos is the Navarro-Franck-White (NFW) profile :

$$\rho(r) = \frac{\rho_s}{(r/r_s)(1 + r/r_s)^2} \,, \tag{1.4}$$

where r_s is the halo scale radius and ρ_s is the characteristic density.

1.1.2 The Microlensing effect

Several studies on the Dark Matter abundance and composition have been based on the microlensing effect. Generally speaking, the lensing effect can take place whenever between a distant observed object and the observer there is a source of gravitational field (such as stars, galaxy clusters, etc.) intense enough to bend the light along the path from the source to the observer. According to the theory of general relativity, postulated by A. Einstein in 1915, the light is expected to follow exclusively the geodesics in curved spacetime. The matter distribution modifies the metric and consequently the path followed by the light varies in proximity of a mass. The mass which generates the gravitational field represents 'the lens'. As a result of the lensing effect, the observer can see multiple images or a distorted image of a unique source.

The microlensing effect was used to test the hypothesis that the DM was made of the so called Massive Compact Halo Objects (MACHOs) i.e. astronomical bodies, as brown dwarfs or black holes. Experiments for MACHOs' detection are based on the *gravitational microlensing* tecnique: if a MACHO interpones between the star and the observer, the star can be seen as brighter for a limited amount of time, from few days to few months for bigger bodies. Such an effect is observed for lenses with small masses ($10^{-6} \leq M/M_{\odot} \leq 10^{6}$) in systems that extent on the Kpc scale.

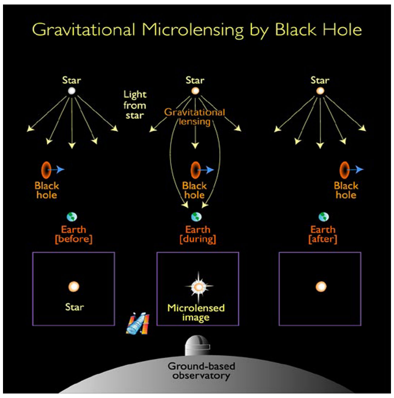

FIGURE 1.3: Illustration of the *microlensing* effect, i.e. the magnification of a light source due to astrophysical bodies acting as gravitational lens.

Unlike the Strong Lensing, where multiple images of the source are observed, in the microlensing what is observed is a time modulation of the luminosity curve of the source due to the relative motion between it and the lens (an illustration is given in Fig. 1.3). Hence, the observed luminosity is

$$\tau = \frac{1}{\delta\Omega} \int \mathrm{d}V \cdot n(D_L) \cdot \pi \cdot \theta_E^2 \,, \tag{1.5}$$

where $\delta\Omega$ is the observation solid angle, $n(D_L)$ is the micro-lens density as function of the lens distance D_L and $\pi\theta_E^2$ is the micro-lens cross section, $\theta_E = \sqrt{\frac{4GM}{c^2}\frac{D_{LS}}{D_L D_S}}$ is the so-called Einstein radius, where D_S is the distance of the source. Assuming a flat space-time and constant density along the line of sight, we have

$$\tau \approx \frac{2\pi}{3}\frac{G\rho}{c^2} D_S^2 \,, \tag{1.6}$$

where D_S is the source distance. For a galaxy like the Milky Way one finds

$$v^2 \approx \frac{GM_g}{r} \rightarrow M_g = \frac{rv^2}{G} \tag{1.7}$$

and

$$\rho \approx \frac{3M_g}{4\pi r^3} \approx \frac{3}{4\pi G}\left(\frac{v}{r}\right)^2 . \tag{1.8}$$

Thus, the optical depth is given by

$$\tau \approx \frac{1}{2}\left(\frac{v}{r}\right)^2 . \tag{1.9}$$

For the Milky Way $\tau \approx 10^{-6}$. This means that roughly one out of a million stars in the nearby galaxies would be lensed. In this way, counting the micro-lenses in a particular direction it is possible to characterize the lens population. The possibility of detect such

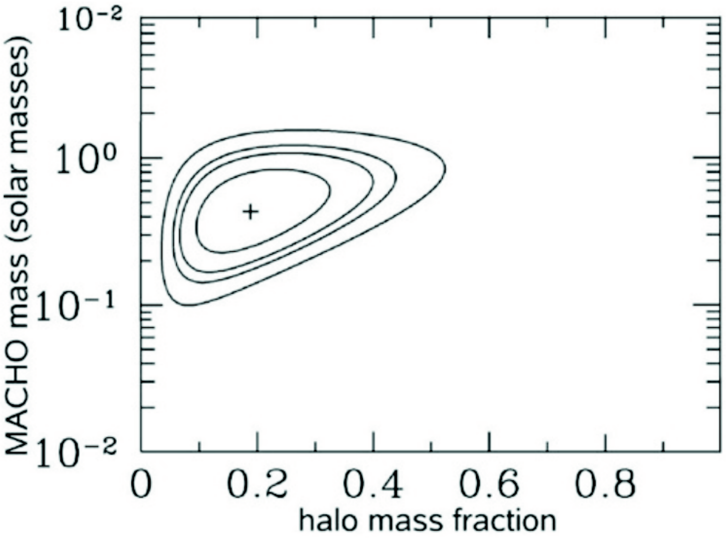

FIGURE 1.4: Likelihood contours obtained from the MACHO experiment. [3] The abscissa is the fraction of the halo mass contained in MACHOs, the ordinate is the MACHO mass. The contours shown correspond to the 60%, 90%, 95% and 99% confidence level.

events depends on their duration (the Einstein crossing time). This is determined by the transverse velocity $v_\perp$ and by the lens mass. For micro-lenses in the halo of the galaxy ($D_L \sim 10$ kpc) with velocity ~ 200 km/s, one has

$$t_E \approx 6 \cdot 10^6 \ s \left(\frac{M}{M_\odot}\right)^{0.5} \approx 0.2 \ \mathrm{yr} \left(\frac{M}{M_\odot}\right)^{0.5} \tag{1.10}$$

If all events had the same time scale, then the number of expected events, N, in the monitoring time Δt is:

$$N = \frac{2}{\pi} n \tau \frac{\Delta t}{t_E} \ , \tag{1.11}$$

where n is the total number of considered sources.

Several research groups worked on the identification of lenses in the Milky Way's halo looking at sources in the Large and Small Magellanic Clouds (LMC and SMC). After the analysis of data collected during several years [3], few microlensing events were observed, leading to the conclusion that MACHOs can account only for less than 20% of the halo mass (Fig. 1.4).

New observation campaigns are currently on going aiming at the observation of microlensing events in the M31 galaxy (Andromeda galaxy). Due to its larger distance compared to the L/SMC galaxies, it is not possible to distinguish single stars and this drastically changes the observation strategy. In this case, the total luminosity of the galaxy should change and, consequently, only high magnification events gives appreciable signal. There are several advantages in looking at M31: due to its inclination along

FIGURE 1.5: Image of the M31 galaxy.

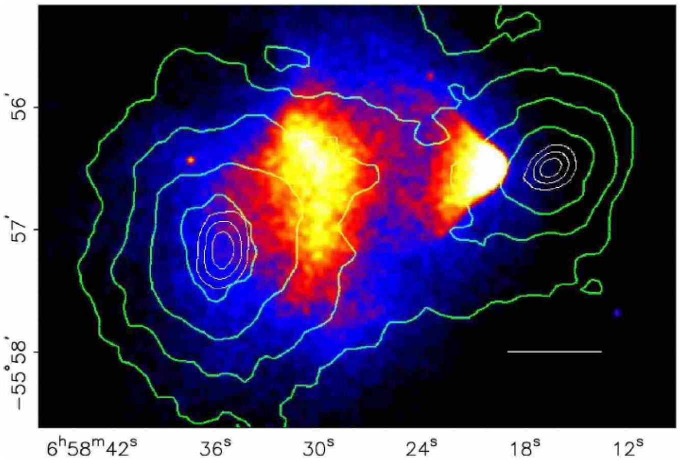

FIGURE 1.6: X-Ray image of the Bullet Cluster. The mass distribution from weak lensing measurements (green lines) is shown together with the baryonic matter distribution (red points). The Dark Matter distribution is drawn as the blue region.

the line of sight (see Fig. 1.5), it is possible to accurately measure its rotation curve. Moreover, the lensing effects show an asymmetry that is not possible to explain only with the stars self-lensing.

1.1.3 Bullet Cluster

Other strong evidences for the DM existence come from the study of the Bullet Cluster (1E0657-558)[4]. It is defined as the collision of two clusters of galaxies (Fig. 1.6). Strictly speaking, the name Bullet Cluster refers to the smaller subcluster, moving away from the larger one. Both clusters have a stellar and gaseous component that interacts in different ways: the stellar component is slowed down by the gravitational field of the other cluster while the two gaseous components behave as a fluid. The gas interactions result in a X-ray emission that can be measured and used to trace the baryonic matter distribution.

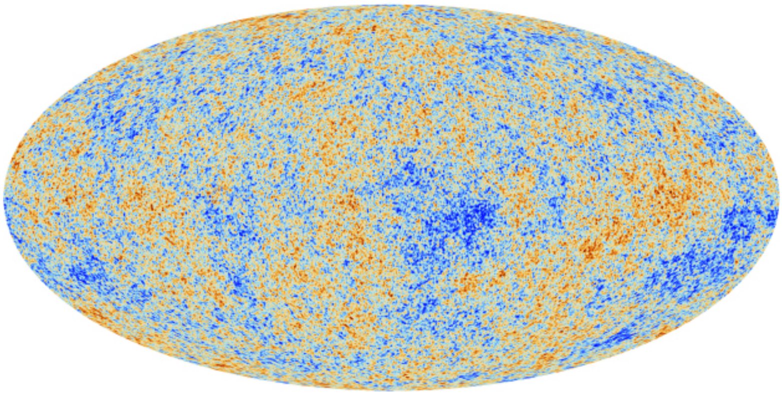

FIGURE 1.7: The anisotropies of the Cosmic Microwave Background (CMB) as observed by Planck. The CMB is a snapshot of the oldest light in our Universe, imprinted on the sky when the Universe was just 380 000 years old. It shows tiny temperature fluctuations that correspond to regions of slightly different densities, representing the seeds of all future structure: the stars and galaxies of today [6].

Experimental measurements show up a discrepancy between the baryonic matter distribution, measured from the X-ray emission (red points in Fig. 1.6), and the gravitational field distribution obtained from lensing measurements (green lines). The blue points in Fig. 1.6 represent the hypothetical Dark Matter distribution. It is based on its characteristics of weak interaction, which let DM particles to pass through each other without being disturbed along their path. Conversely, this is not the case for the hot gas and stellar component. As the Dark Matter can continue to move on its trajectory, it is placed in the outer region of the Bullet Cluster.

1.2 Cosmological scale evidences

The lensing studies showed that, even if the Dark Matter exists, it is mainly composed by *non-baryonic* matter. Further convincing experimental evidences that sustain such a scenario come from the *Cosmic Microwave Background* (CMB) power spectrum analysis, but also from the Big Bang Nucleosynthesis (BBN).

The Cosmic Microwave Background, discovered by Arno Penzias and Robert Wilson in 1964 [5], provides important hints about the Dark Matter existence, composition and, in particular, about its abundance in the Universe. The CMB consists of relic photons from the early Universe stage at which the temperature dropped to about 3000 K, allowing electrons to recombine with protons. Hence, the Universe became transparent to the photons as they had not enough energy to ionize the hydrogen. The CMB almost perfectly follows an ideal black body spectrum with a temperature of $T = 2.726$ K. However, it shows temperature anisotropies (Fig. 1.7), at a level lower than 10^{-5}, that can give crucial information on the Universe composition.

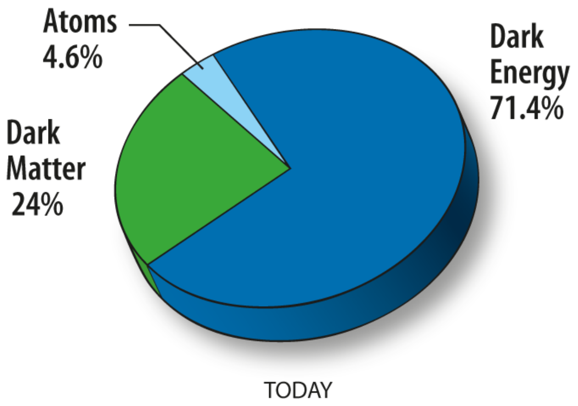

FIGURE 1.8: Representation of the contributions to the overall Universe content.

The CMB spectrum is characterized by a peak structure, shown in Fig. 1.9, as a consequence of two opposite effects: the gravitational force attracted the photons into the higher density regions, while the gas pressure pushed them apart. The angular power spectrum is obtained by decomposing the anisotropy map into spherical harmonics and taking into consideration various distortions such as emissions from galaxies. These anisotropies can be described as

$$\frac{\delta T}{T}(\theta,\phi) = \frac{T(\theta,\phi) - \langle T(\theta,\phi)\rangle}{\langle T(\theta,\phi)\rangle} = \sum_{l=2}^{+\infty}\sum_{m=-l}^{+l} a_{lm} Y_{lm}(\theta,\phi)\,, \tag{1.12}$$

where $Y_{lm}(\theta,\phi)$ are the spherical harmonics.

The size and the position of the peaks of the CMB spectrum provide valuable information on cosmological parameters, such as the curvature and the energy-matter composition of the universe: Ω_{tot}, Ω_b and Ω_{DM}. From the CMB study [7, 8] it is then possible to extract an estimate of the non-baryonic Dark Matter abundance in the Universe:

$$\begin{aligned}
\Omega_\Lambda &= 0.707 \pm 0.010\,; \\
\Omega_m &= 0.293^{\pm 0.056}_{\pm 0.010}\,; \\
\Omega_b h^2 &= 0.02211 \pm 0.00034\,; \\
\Omega_{DM} h^2 &= 0.1162 \pm 0.0020\,.
\end{aligned}$$

From the values of cosmological parameters results that the dark energy, Λ, accounts for about 70% of the Universe energy content, while the majority of the matter content is in the form of non-baryonic Dark Matter (see Fig. 1.8).

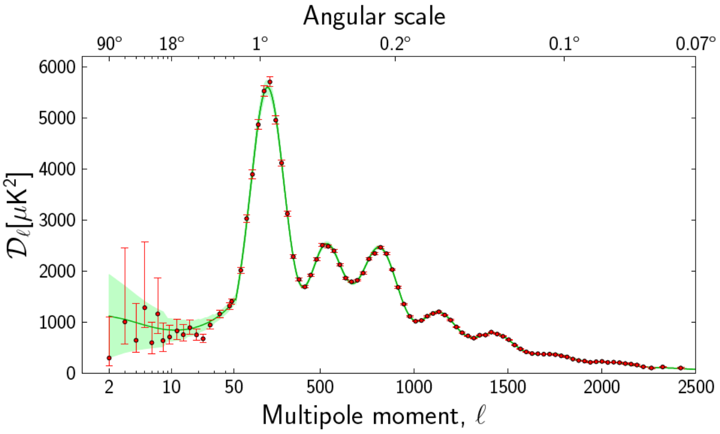

FIGURE 1.9: The 2013 Planck CMB temperature angular power spectrum [6]. The error bars include cosmic variance, whose magnitude is indicated by the green shaded area around the best fit model.

1.3 Dark matter composition

The Dark Matter identification is an open question still widely debated. There is a great variety of hypotisized DM candidates, none of them has been proved without a doubt, but one of the most studied is the WIMP. Nevertheless, it is worth recalling some of the main DM candidates that have been proposed to date. The dark matter can be divided in **barionic** dark matter and **non barionic**. The barionic dark matter is found in MACHOs (Massive astrophysical compact halo object), bodies that emits little or no radiation and drifts through interstellar space unassociated with any planetary system. The non-barionic dark matter instead is divided into Hot Dark Matter (*HDM*) and Cold Dark Matter (*CDM*), respectively composed by particles in relativistic motus or not and they represent a residual of the matter-radiation decoupling.

1.3.1 Barionic Dark Matter

The main characteristic of Dark Matter is the undetectability through direct observation. Since MACHOs are not luminous, they are hard to detect. MACHOs include black holes or neutron stars as well as brown dwarfs. This scenario predicts a diffuse γ-ray emission from the Milky Way's dark halo. A flux, whose properties are in a quite good agreement with the theoretical prediction, has been observed by the EGRET detector [9] mounted onto the CGRO satellite. Nonetheless, from microlensing studies and cosmological observations, we know that the majority of the Dark Matter is non-baryonic and MACHOs can account for not more than 20% of the total Dark Matter amount. The experiment EROS (*Experience pour la Recherche d'Objets Sombres*) at La Silla (Cile) observed for a time window of 5 years, about 30 million of stars belonging to the Magellanic Clouds individuating 8 possible MACHO. The data confirm a fraction of barionic dark matter, but, as already mentioned, not sufficient to explain totally the dark matter amount.

1.3.2 Non-barionic dark matter

About the non barionic dark matter there are two possible scenarios. The first one was hypothesized by Zeldovich, and it is named Hot Dark Matter, where the Dark Matter particles are relativistic. It implies a top-down structure formation history of the Universe where the big structures, such as galaxies, came first. However, the evolution of such systems were too slow if compared with the time scale of the primordial galaxy formation. Moreover, the high energy of the DM particles was in contrast with the formation of such big structures since relativistic particles would be dispersed in the space. The second scenario, which is also accepted and supported, is called Cold Dark Matter (CDM), in which Dark Matter is not relativistic. First evidences for the CDM came from the N-body simulations by Jeremiah Ostriker and James Peebles [10], in the 1970s. They simulated the interactions of a distribution of mass points, that represented stars moving in a galaxy, rotating around a central point. To get the correct interactions between the mass points, they used the Newton's law. They found that, in a time less than an orbital period, most of the mass points would have collapsed to a bar-shaped dense concentration, close to the center of the galaxy, with only few mass points at larger radii. This result is clearly in contrast with the elegant spiral or elliptical shape of the galaxies that we observe. But when they added a static and uniform distribution of mass, from 3 to 10 times the size of the total mass of the mass points, they found more recognizable structures. Thus, Ostriker and Peebles had solid numerical evidence that cold Dark Matter was necessary to form the types of galaxies we observe in the universe.

In the following sections we outline the main proposals for CDM candidates arose so far. Candidate particles have been hypothesized in different theoretical frameworks, starting from the Standard Model but also in the Supersimmetry (SUSY) and in the Extra dimensions models context.

The present work will mainly concentrate on the WIMP dark matter candidate and its possible nature.

1.3.3 The MOND Theory

Before describing the possible WIMP candidate, there is also an alternative theory that must be mentioned. The MOND (*MOdified Newtonian Dynamics*) theory was proposed in 1981 by the israelian physicist Mordehai Milgrom. The theory's original motivation was to explain the fact that the velocities of stars in galaxies were observed to be larger than expected based on Newtonian mechanics. Milgrom noted that this discrepancy could be resolved if the gravitational force, experienced by a star in the outer regions of a galaxy, was proportional to the square of its centripetal acceleration (as opposed to the centripetal acceleration itself, as in Newton's Second Law), or alternatively if gravitational force came to vary inversely with radius (as opposed to the inverse square of the radius, as in Newton's Law of Gravity). In MOND, violation of Newton's Laws occurs at extremely small accelerations, characteristic of galaxies yet far below anything typically encountered in the Solar System or on Earth. The Newton's second Law, modified according to the MOND theory, becomes:

$$F = ma\mu\left(\frac{a}{a_0}\right) \tag{1.13}$$

where for values of the accelleration not big it is possible to approximate as follow

$$\mu\left(\frac{a}{a_0}\right) \simeq \frac{a}{a_0}. \tag{1.14}$$

where a_0 is a constant and has a numerical value of $10^{-10}\mathrm{m/s^2}$ and $\mu(x) = 1$ if $|x| \gg 1$ and $\mu(x) = x$ if $|x| \ll 1$.

Using the Newton's law modified and the classical gravitational law it is possible to determine the acceleration acquired by stars as a function of the distance from the center of the galaxy. From this relation, is it possible to determine the evolution of the velocity for bigger distances (smaller accelerations):

$$\frac{GM}{r^2} = \frac{a^2}{a_0} \qquad \rightarrow \qquad a = \frac{\sqrt{GM}}{r} \qquad \rightarrow \qquad v = (GMa_0)^{1/4}.$$

The constant trend of the velocity corresponds thus to the what observed, and for this reason the MOND theory represent an alternative to the explanation of the rotational velocity trend of galaxies. This theory results unefficient in the attempt to explain phenomena such as the bullet cluster or the gravitational lensing, but it was the first competitive theory with the Dark Matter one.

1.4 Standard Model candidates

The Standard Model (SM) of particles offers some viable candidates in the framework of the HDM, while no SM particles seem to be able to account for the larger part of cold Dark Matter.

1.4.1 Relic Neutrinos

The cosmic neutrino background ($C\nu B$) is the universe's background particle radiation composed of neutrinos, which are known as relic neutrinos. Like the cosmic microwave background radiation (CMB), the $C\nu B$ is a relic of the big bang; while the (CMB) dates from when the universe was $\sim 379 \cdot 10^3$ years old, the $C\nu B$ decoupled from matter when the universe was one second old. It is estimated that today, the $C\nu B$ has a temperature of roughly 1.95 K. Since low-energy neutrinos interact only very weakly with matter, they are notoriously difficult to detect, and the $C\nu B$ might never be observed directly. There is, however, compelling indirect evidence for its existence.

From the cosmology, we have that their relic density, under the hypothesis of massive and non relativistic neutrinos, is given by

$$\Omega_\nu h^2 = \sum_i^3 \frac{m_i}{93eV} \tag{1.15}$$

where h is the Hubble constant in units of 100 km/s/Mpc, the number 3 accounts for the neutrino's flavours and m_i is the mass of the i-th neutrino. Neutrinos as the main source of dark matter are experimentally excluded. The most stringent constraints on their masses come from the combination of PLANCK data with large scale structure information

$$\sum m_\nu < 0.18eV \quad (95\% C.L.) \tag{1.16}$$

Given this upper bound on the neutrino mass, the resulting relic density is not enough to explain the Dark Matter as mainly composed by them.

1.4.2 Axions

Remaining in the SM scenario, the *axion* is another Dark Matter candidate. This particle is a Nambu-Goldstone boson which corresponds to the phase of a complex field, the Peccei-Quinn field, which breaks the $U(1)_{PQ}$ symmetry. The $U(1)_{PQ}$ field is a global $U(1)$ symmetry, which carries QCD anomalies, proposed by Peccei and Quinn as solution to the strong CP problem [11]. This symmetry is broken at the scale of f_a which is the axion decay constant, also called PQ scale. The relic abundance of the axions [12] can be expressed, using the QCD scale $\Lambda_{QCD} \sim 200$ MeV, as

$$\Omega_a h^2 = \theta^2 \left(\frac{f_a}{10^{12}\text{GeV}} \right)^{1.175} . \tag{1.17}$$

With $\theta \sim 0.1$ and $f_a \sim 10^{12}$ GeV axions can represent an important percentage of the CDM which might consist only of axions. They can be detected through the *Primakoff effect* [13] where an axion is converted into a photon under a proper magnetic field. The CERN Axion Solar Telescope (CAST) [14] and the PVLAS experiment [15] are searching these particles. While the former looks for solar axions, the latter fires polarized light through a long vacuum region with a 5.5 T magnetic field and searches for anomalous rotations of polarization; according to the theory, the vacuum becomes birefringent, thus photons with polarization aligned with the magnetic field are delayed as they are preferentially transformed into axions which travel slower than the speed of light.

The PVLAS collaboration initially claimed the detection of an irregular rotation corresponding to an axion mass of 1-1.5 meV, but retracted their results upon obtaining a null result after upgrades. The current strongest limits, on the axion mass, have been set by the XENON100 experiment [16].

1.4.3 Interacting Massive Particles (WIMPs)

Concerning SUSY, many interesting features make it attractive, including its role in understanding the fundamental distinction between bosons and fermions and the problems of hierarchy for neutrinos. In this framework, Dark Matter particles are identified with the general definition of: Weakly Interacting Massive Particles (WIMPs). They are stable, cold, non-baryonic and interact only through gravitational and weak forces. If WIMPs are stable, there is a cosmological relic abundance produced during the Big Bang. Assuming for such particles a mass m_χ, one has that for temperature $T > m_\chi$ they were in thermal equilibrium while at temperatures below m_χ they decoupled and their abundance started to lower. Finally, when the expansion rate of the Universe became larger than the annihilation rate ($\Gamma < h$), where h is the Hubble constant, the WIMP abundance "freezed out", resulting in the current relic abundance.

The annihilation cross section of a new particle interacting at the weak scale can be estimated as: $\langle \sigma \rangle \sim 10^{-25}$ cm^3 s^{-2}. Such value is close to the one derived from cosmological arguments. This strongly suggests that if a stable particle associated with the electro-weak scale interactions exists, then it is likely to be the dark matter particle. This coincidence has provided strong motivation for finding WIMPs.

There are several WIMP candidates; the most promising is the Lightest Supersymmetric Particle (LSP), which is the *neutralino.*

1.4.4 Neutralino

The Minimal Supersymmetric Standard Model (MSSM) contains the smallest possible field content necessary to give rise to all the Standard Model (SM) fields. All of the SM particles have R-parity equal to 1 and all *sparticles*, their superpartners, have R = -1. Thus, from R-parity conservation (first introduced to suppress the rate of proton decay), *sparticles* can only decay into an odd number of *sparticles* (plus Standard Model particles). The Lightest Supersymmetric Particle is, therefore, stable and can only be destroyed via pair annihilation, making it an excellent Dark Matter candidate. Among few alternatives, the most promising LSP is the lightest neutralino, which is uncharged under electromagnetic and strong interactions. In the MSSM, binos ($\tilde{B}$), winos ($\tilde{W}_3$) and higgsinos ($\tilde{H}_1^0$, $\tilde{H}_1^0$) states mix into four Majorana fermionic mass eigenstates, called neutralinos. The four neutralinos are labeled as: $\tilde{\chi}_1^0$, $\tilde{\chi}_2^0$, $\tilde{\chi}_3^0$ and $\tilde{\chi}_4^0$. The first of them is the lightest one and it is referred as the neutralino, $\chi = \tilde{\chi}_1^0$. The most relevant neutralino interactions for Dark Matter searches are self annihilation and elastic scattering with nucleons. At low velocities, the leading channels for neutralino annihilations are into fermion-antifermion, gauge bosons pairs and final states containing Higgs bosons. All the possible annihilation processes are of interest for indirect Dark Matter searches, while direct detection techniques are based on the elastic scattering processes. The WIMP interaction with the matter can be divided into two types: spin-independent (SI) and spin-dependent (SD). A scalar interaction, i.e. SI, with quarks can be expressed as

$$\mathscr{L} = a_q \chi\bar{\chi}\bar{q}q \tag{1.18}$$

where a_q is the WIMP-quark coupling. The scattering cross section is given by

$$\sigma_{scalar} = \frac{4m_r^2}{\pi} f_{p,n}^2 \tag{1.19}$$

where m_r is the reduced mass of the nucleon and $f_{p,n}^2$ is the coupling to protons and neutrons. The total scalar cross section for interactions with a nucleus, in the case of zero transfer momentum, is given by the sum over all the nucleons:

$$\sigma = \frac{4m_r^2}{\pi} \Big(Z f_p + (A - Z) f_n \Big)^2 . \tag{1.20}$$

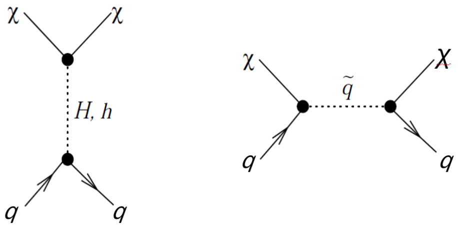

FIGURE 1.10: Feynman diagrams for neutralino-quark scalar (**spin-independent**) elastic scattering interactions [17].

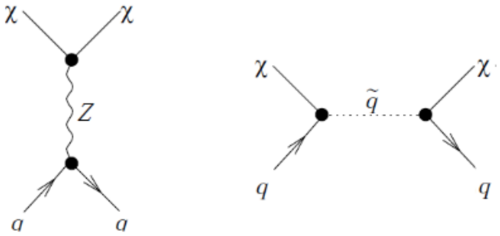

FIGURE 1.11: Feynman diagrams for neutralino (**spin-dependent**) axial-vector interactions [17].

A spin-dependent interaction, i.e. axial-vector interaction, between WIMPs and quarks can be expressed as

$$\mathcal{L}_{AV} = d_q \overline{\chi} \gamma^\mu \gamma_5 \chi \overline{q} \gamma^\mu \gamma_5 q \,, \tag{1.21}$$

where d_q is the generic coupling. The Feynman diagrams for both SI and SD neutralino interactions are shown in Fig.1.10 and 1.11.

The cross section for SD interactions is given by [18]

$$\frac{d\sigma}{d|\vec{v}|^2} = \frac{1}{2\pi v^2} \overline{|T(v^2)|^2} \,, \tag{1.22}$$

where v is the WIMP velocity relative to the target and T(v^2) is the scattering matrix element. At zero transfer momentum, one has

$$\begin{aligned} \overline{|T(0)|^2} = \frac{4(J+1)}{J} |(d_u \Delta_u^p + d_d \Delta_d^p + d_s \Delta_s^p) \langle S_p \rangle + \\ + (d_u \Delta_u^n + d_d \Delta_d^n + d_s \Delta_s^n +) \langle S_n \rangle|^2 \,, \end{aligned} \tag{1.23}$$

where J is the total nuclear spin of the target nucleus, $\Delta_{u,d,s}^{n,p}$ are the fractions of the nucleon spin carried by a given quark and $\langle S_{p,n} \rangle$ are the expectation values of the total spin of protons and neutrons, respectively. For target nuclei with even numbers of protons and neutrons, the total spin is equal to 0. Thus, for such nuclei, the spin-dependent cross section vanishes.

Another kind of interaction to be considered is the WIMP-quark vector interaction:

$$\mathcal{L}_V = b_q \overline{\chi} \gamma_\mu \chi \overline{q} \gamma_\mu q \tag{1.24}$$

where b_q is the WIMP-quark vector coupling. The zero transfer momentum cross section can be expressed as [19],

$$\sigma = \frac{m_\chi^2 m_N^2 [2Zb_p + (A-Z)b_n]^2}{64\pi(m_\chi + m_N)^2} \;, \tag{1.25}$$

with $b_q = G_F(T_q^3 - 2e_q \sin^2\theta_W)/\sqrt{2}$, where G_F is the Fermi constant, T_q^3 and e_q are the weak isospin and electric charge of the quark q, respectively, and θ_W is the Weinberg angle.

1.4.5 Sneutrino, Gravitino and Axino

In the SUSY context the sneutrino and gravitino, the superpartners of the SM neutrino and graviton, have been considered as DM candidate. The **sneutrino** is a viable candidate if its mass were in the range [550 , 2300] GeV/c^2 . Despite this possibility, it has been rejected since its cross section would be higher than the current found limits. The **gravitino** interacts only through the gravitational force and this makes it very hard to detect. Gravitinos can be produced in 2 → 2 processes such as scalar-fermion-gravitino or gaugino-gauge boson-gravitino vertices [20].

The Axino, $\tilde{a}$, is the superpartner of the axion and it is a Majorana chiral fermion. Its mass is strongly model-dependent meaning that it could be the lightest particle, thus stable, in SUSY models. A production channel for $\tilde{a}$ is the decay of nonthermal particles. An example of this process is the decay of the lightest stau mass eigenstate $\tilde{\tau}_2$.

1.4.6 Wimpzillas

The Super heavy Dark Matter, also named wimpzillas, has been proposed as a non-thermal Dark Matter candidate. The masses of this kind of particles range from 10^{12} up to 10^{16}GeV/c^2. In the early Universe there were different available channels to produce such particles as the gravitational production at the end of inflation, resulting from the expansion of the background space-time. The interaction cross section of such particles with ordinary matter, covers a wide range of hypotheses, from very weak to strong coupling (in the latter case super-massive particles are sometimes called simpzillas). The wimpzillas have been proposed as a first explanation for the observed ultra high energy cosmic rays, above the GZK cut-off ($\sim 5 \cdot 10^{19}$ eV). Above this energy the Universe, on cosmological scale (≥ 50 Mpc), is opaque to protons. Since sources for such energetic protons have not been observed yet, a possible explanation for their existence is that they are produced in the decay or annihilation of super heavy Dark Matter particles. (top-down cosmic-ray models [21]).

1.4.7 Kaluza-Klein particle

In the **Extra dimensions model**, the space is considered to have four dimensions needed to include electromagnetism into a 'geometric' theory of gravitation. Also in this scenario, the lightest particle, called **Kaluza-Klein** (KK) particle, is a viable candidate for the Dark Matter. If Standard Model particles propagate in such Extra dimensions and the KK parity is conserved, the lightest KK particle is stable, becoming an excellent candidate for DM. The mass of the first stable KK particle ranges from several hundreds of GeV up to few TeV, and can be detected via elastic scattering in the Dark Matter direct search experiments, or indirectly via annihilation products, such as positrons from the galactic halo, gamma rays from the galactic center, high energy neutrinos from the core of the Sun or the Earth, and antiproton. Due to their characteristics, a tonne-scale detector is required to detect their interactions that makes suitable experiments as XENON1T.

1.5 Experiments searching for WIMPs

In the last few decades the dark matter search has been one of the most active and interesting field in physics, that is why a great variety of experiments were constructed for dark matter detection. The DM experiments can be divided in two main classes: **direct detection**, based on DM scatterings off target nuclei, and **indirect detection**, searching for DM particles annihilation products inside and outside the galaxy. Different choices of the detection technique and target material allow to scan different ranges of the parameter space of DM models. The indirect detection looks for the products of the interactions among dark matter itself. According to the type of the particle produced, the detector technology is different and specific to that particle detection, as, for instance, the observation of the gamma radiation must be done outside the terrestrial atmosphere, which is opaque to. This kind of observation is made with Čherenkov telescopes. Neutrinos and antineutrinos, producted by the annihilation of the dark matter inside massive bodies, are observed with large area telescope such as the submarine telescope KM3NeT in Sicily or ICECUBE at the south pole. It is also possible to observe the radio waves producted by the charged particles as a result of the annihilation. A measurements of dark matter through the listening of these radio waves could be done

only if we know the distribution of dark matter in the galaxy questioned.
Lastly, it is particularly interesting the analysis of the production of couples particle-antiparticle, such as $p\bar{p}$ and e^-e^+: **AMS-02**, a satellite of the International Space Station ISS saw a unxepected abundance of antimatter that can be attributed to dark matter annihilation. Unfortunately the provenience of these particle is still unknown because the charged particles are deflected by the galactic electomagnetic fields.
The story of the best results for WIMP masses above 8 GeV/c^2 sees at first what has been obtained in 2012 by **XENON100** [22], reaching the best SI limit of $2 \cdot 10^{-45}$ cm^2 at 55 GeV/c^2 mass, then LUX [23] in 2013 with $7.6 \cdot 10^{-46}$ cm^2 for 33 GeV/c^2 WIMPs and finally an update of the **LUX** result that states a WIMP-nucleon spin-independent cross sections above $2.2 \cdot 10^{-46}$ cm^2 ((90%$C.L.$) confidence level. When combined with the previously reported LUX exposure, this exclusion strengthens to $1.1 \cdot 10^{-46}$ cm^2 at 50 GeV/c^2. [24] At lower masses, other experiments, as **CoGeNT** and **CDMS**, are more sensitive.
In the next sections we browse through the main Dark Matter experiments based on both direct and indirect detection techniques.

1.5.1 Direct detection experiments

Dark Matter interactions with ordinary nuclei are characterized by very small cross sections. The direct detection of WIMP-nucleon scatterings requires very large target masses and an extremely low level of radioactivity. Hence, an ultrapure detector is mandatory as well as its placement into underground laboratories in order to properly reduce the background rate. The detection technique aims to the observation of WIMP with velocity lower than the escape velocity from the Milky Way, thus the particles trapped inside the galactic halo. The collisions between WIMPs and nuclei are both elastic and not-elastic and there might be a spin dependance. Due to the very small cross section, the exposition times are very long, according to some theoretical model, a sample of 2kg ($\sim 10^{25}$ atoms) undergoes an interaction with a WIMP only once in a year through elastic diffusion. [25]

In the next part of this chapter we go through the variuos experiment for the direct dark matter detection.

DAMA/LIBRA The DAMA/LIBRA detector, placed in the **LNGS** (**L**aboratori **N**azionali del **G**ran **S**asso) underground laboratory, is the upgrade of the previous DAMA/NaI detector. The experiment aims to find an annual variation of the number of detection events, caused by the variation of the velocity of the detector relative to the dark matter halo as the Earth orbits the Sun. Its sensitive part is made of 25

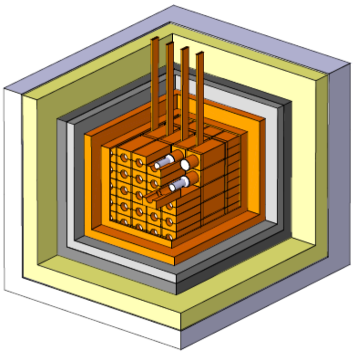

Figure 1.12: DAMA/LIBRA detector: schematic view of the 25 highly radio-pure NaI(Tl) scintillator crystals within the passive shield. It is made of a sealed copper box flushed with highly pure nitrogen; to reduce the natural environmental background the copper box is surrounded by a low background multi-ton shield. In addition, 1 m of concrete, made from the Gran Sasso rock material, almost fully surrounds this passive shield. The installation has a 3-level sealing system which prevents environmental air reaching the detectors.

highly radio-pure NaI(Tl) crystals, each one of 9.70 kg, arranged in a 5 x 5 matrix. For the Dark Matter search, the modularity of DAMA/LIBRA is very useful since WIMPs are expected to give only one interaction in the entire stuck of detectors. Moreover, the characteristics of the scintillators allow to reject noise events. With the exception of the noise rejection, in DAMA/LIBRA it is not possible to distinguish between nuclear and electromagnetic recoils.

DAMA/LIBRA has observed a signal modulation that could be explained as due to the modulation of the Dark Matter flux. [26] Several explanations for the modulation signal have been proposed to investigate a possible background as source of this signal. For example, since DAMA/LIBRA does not have a muon veto, it was hypothesized that it was the modulation of the muon flux to generate the signal [27]. However, recently it was shown that the muon flux is too low to explain the observed signal [28].

CoGeNT The CoGeNT Dark Matter Experiment is a direct search for signals from interactions of dark matter particles in a low-background germanium detector located atthe *Soudan Underground Laboratory* in Minnesota.

The CoGeNT Experiment uses a single, 440 gr, high-purity germanium crystal cooled to liquid nitrogen temperatures in its measurements. The CoGeNT detector has the advantage of a very low energy threshold (∼ 0.5 keV) which allows it to search for nuclear recoil events due to dark matter particles of relatively low mass ($> 5\,\mathrm{GeV/c^2}$). In addition to a low-background configuration, the detector is capable of distinguishing and rejecting background events from the surface through measurement of the risetime of the detector's signals. The CoGeNT detector senses only ionization charge from nuclear recoils and places limits on the mass and interaction cross-section of dark matter

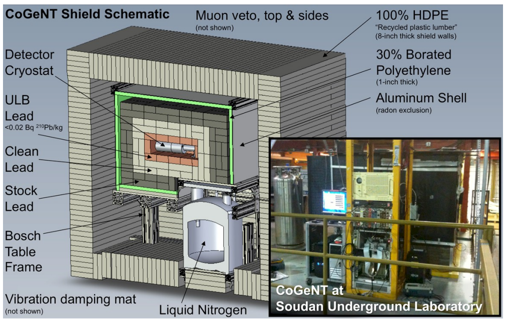

FIGURE 1.13: Schematic view of the CoGeNT structure with its passive shield.

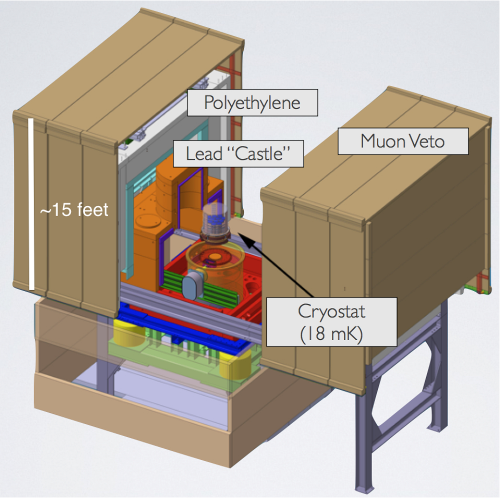

FIGURE 1.14: Schematic view of the EDELWEISS-II experiment.

particles by excluding any candidate mass and cross-section pair that would result in a signal above the background of the detector. In 2010 CoGeNT observed an excess of events at low energies, in the bulk of the Ge crystal [29]. Several analyses have been performed to explain this excess as due to Dark Matter interactions. Assuming a Maxwellian velocity distribution with $v_0 = 230$ km/s^{-1}, and $v_{esc} = 500$ km/s^{-1} for a spin-independent model, with equal coupling to protons and neutrons and without any unknown background, the WIMP hypothesis gives a nice agreement, especially in the very low energy region, with the observed data. The best results were obtained for $m_\chi = 9.4$ GeV and $\sigma = 0.84 \cdot 10^{-40}$ cm^2 . However, such results are excluded by other experiments such as CDMS-Si.

EDELWEISS II The EDELWEISS-II detector (Fig. 1.14), at the *Laboratoire Souterrain de Modane* under 4800 m.w.e., is enclosed in a passive shield, covered by a muon veto system for throughgoing muons. The core of the detector is based on ten bolometers of hyper-pure Ge crystals of cylindrical shapes with a diameter of 70 mm and a height of 20 mm, all inside a cryostat. For each event, two signals are recorded: one from the temperature increase, measured using neutron transmutation doped (NTD)-Ge thermometric sensors glued on each detector, and one from the charges produced in the interaction that are recorded by proper electrode wires on both side of the Ge bolometers. In 2012, the collaboration carried out an analysis on low-energy ($E < 20$ keV) WIMP-induced nuclear recoils [30]. For a WIMP mass of 30 GeV/c^2, three events have been found as possible candidates. The data indicated no evidence for an exponential distribution of low-energy nuclear recoils that could be attributed to WIMP elastic scattering after an exposure of 113 kg · days. For WIMPs of mass 10 GeV/c^2, the observation of one event in the WIMP search region results in a 90% CL limit of $1.0 \cdot 10^{41}$ cm^2 on the spin-independent WIMP-nucleon scattering cross section. [30]

SuperCDMS The SuperCDMS detector is a bolometer at the Soudan Underground Laboratory. To operate, a cryogenic system based on He_3/He_4 dilution refrigerator has been realized. The core of the detector is made of 15 600 gr Ge crystals from which it is possible to extract the phonon and the charge signals. The crystals have cylindrical shape with a diameter of 76 mm and height of 25 mm. The phonon sensor is a superconducting 174 W film held in the transition state from the superconducting to the normal state (therefore called Transition Edge Sensor or TES). A small change in the temperature leads to a large variation in the measured resistance. In 2016, the collaboration carried out the analysis of a run characterized by an exposure of 612 kg· days [31]. This yielded minimum WIMP-nucleon spin-independent scattering cross-section limits of $1.8 \cdot 10^{-44}$ and $1.8 \cdot 10^{-41}$ cm^2 at 90% confidence for 60 and 8.6 GeV/c^2 WIMPs, respectively.

CRESST-CRESST II-CREST III The CRESST experiment searches directly for dark matter particles via their elastic scattering off nuclei. The nuclei are in the absorber of a cryogenic detector, capable of detecting the small energy of the recoiling nucleus which has been hit by an incoming dark matter particle. CRESST-II is the upgrade that includes a new neutron shield and a muon veto. CRESST uses simultaneously two independent detectors for revealing heat/phonon and light. The core of the detector is made of modules that consist of a $CaWO_4$ 300 g crystal, the target, and a silicon-on-sapphire (SOS) wafer used for measuring the scintillation light. In their interaction inside the crystals, WIMPs lose energy producing phonons and a small amount of scintillation light. The reading of signals from crystals and SOS is obtained by a Transition Edge Sensor (TES) attached to them. All these elements are enclosed in a reflective and scintillating case (Fig. 1.15).

The use of two detectors allows for precise measurements of the deposited energy and background discrimination. For example, the electromagnetic background rejection can be achieved using the scintillation to phonon signals ratio.

In 2016, the CRESST-II collaboration has published its results from the analysis of a 52 kg · days exploring masses down to 0.5 GeV/c^2, a novelty in the field of direct dark matter searches. [32].

In Fig. 1.16 the exclusion limits from several DM experiments in the low WIMP mass region are shown. .

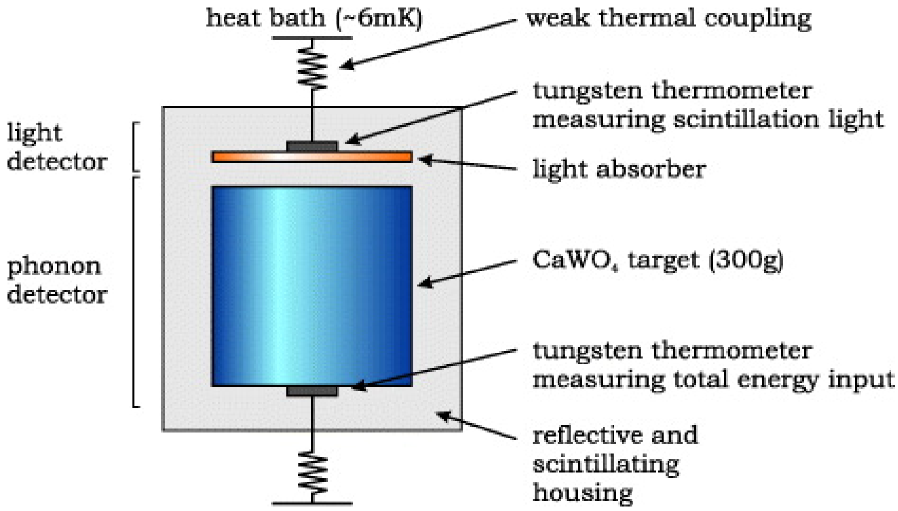

FIGURE 1.15: Scheme of the CRESST-II module.

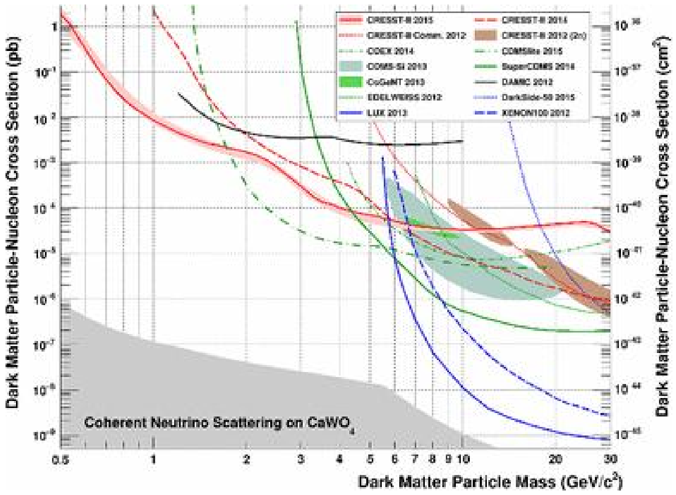

FIGURE 1.16: Parameter space for elastic spin-independent dark matter-nucleon scattering. The result from a blind analysis is drawn in solid red together with the expected sensitivity (1σ confidence level (C.L.)) from the data-driven background-only model (light red band). The remaining red lines correspond to previous CRESST-II limits [33]. The favored parameter space reported by CRESST-II phase 1, CDMS-Si[34] and CoGeNT [35] are drawn as shaded regions. For comparison, exclusion limits (90 % C.L.) of the liquid noble gas experiments are depicted in blue, from germanium and silicon based experiments in green and black. In the gray area coherent neutrino nucleus scattering, dominantly from solar neutrinos, will be an irreducible background for a CaWO4-based[36] dark matter search experiment WIMP parameter space for spin-independent WIMP-nucleon scattering.

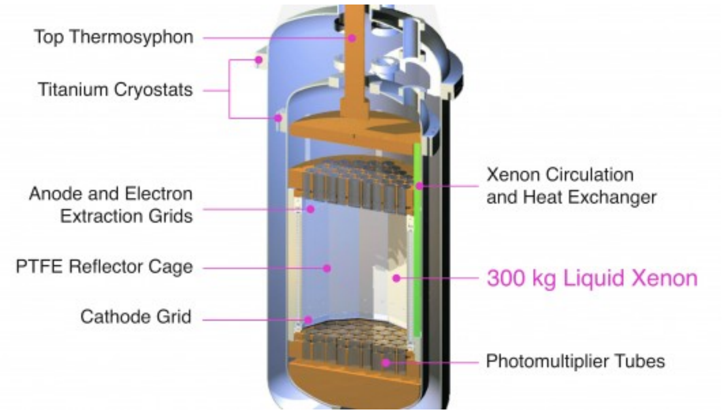

FIGURE 1.17: LUX cryostats and TPC structures.

XENON The XENON Collaboration faces the direct search for WIMPs through a scalable LXe detector arranged in a double-phase TPC. The first stage was the XENON10 experiment, successively upgraded to XENON100. The further extension is represented by the XENON1T experiment, which is currently in data acquisition phase. We describe in detail this experiment in the next Chapter.

LUX The Large Underground Experiment (LUX) is also based on a double phase Time Projection Chamber (TPC) which contains Xe in liquid and gaseous phases. The TPC, which contains an active volume of LXe of about 300 kg, is hosted in a double vessel structure that guarantees thermal isolation (Fig. 1.17). The detector is placed at the Stanford Underground Research Facility (SURF) at a depth of ~ 1500 m and it is surrounded by a water tank that acts as muon veto. The TPC has a diameter of 47 cm and a height of 48 cm. The prompt scintillation signal, **S1**, and the electroluminescence one, **S2**, are read by two array of PMTs.

LUX published its last results in 2016. After a $3.35 \cdot 10^4$ kg/ day, there were no evidence of WIMP nuclear recoils. At a WIMP mass of 50 GeV c^{-2} , WIMP-nucleon spin-independent cross sections above $2.2 \cdot 10^{-46}$ cm^2 are excluded at the 90% confidence level. When combined with the previously reported LUX exposure, this exclusion strengthens to $1.1 \cdot 10^{-46}$ cm^2 at 50 GeV c^{-2}. After the selection of a 118.3 kg fiducial volume for the analysis, 160 events have been observed in the WIMP search region. From the likelihood analysis, all the events have been found to be compatible with the background-only hypothesis resulting in new upper limits for the DM spin-independent cross section, whose minimum has been found at $7.6 \cdot 10^{-46}$ cm^2 for a WIMP mass of 33 GeV/c^2 [37].

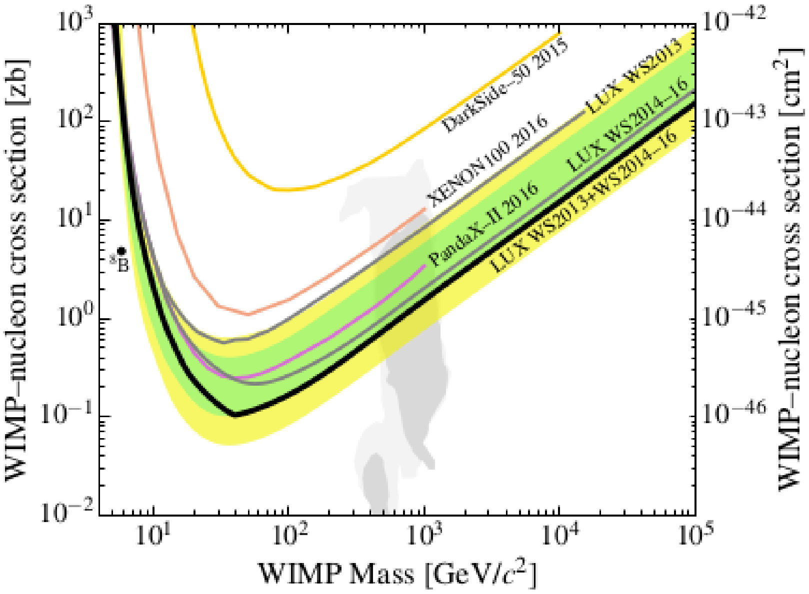

FIGURE 1.18: Upper limits on the spin-independent elastic WIMP- nucleon cross section at 90% CL. The solid gray curves show the exclusion curves from LUX WS2013 (95 live days) and LUX WS2014-16 (332 live days). These two data sets are combined to give the full LUX exclusion curve in solid black ('LUX WS2013+WS2014-16'). The 1- and 2-σ ranges of background-only trials for this combined result are shown in green and yellow, respectively; the combined LUX WS2013+WS2014-16 limit curve is power constrained at the -1σ level. Also shown are limits from XENON100 (red), DarkSide-50 (orange), and PandaX-II (purple). The expected spectrum of coherent neutrino-nucleus scattering by ^{8}B solar neutrinos can be fit by a WIMP model plotted here as a black dot. Parameters favored by SUSY before this result are indicated as dark and light gray (1- and 2-σ) filled regions.

1.5.2 Indirect detection experiments

Indirect techniques aim to detect DM decay or annihilation products. It is usually assumed that WIMPs can annihilate in SM particles. Viable signatures for such kind of processes are thus the production of neutrinos, γ-ray, positrons, anti-protons and anti-deuterons.

General Antiparticle Spectrometer (GAPS) GAPS (General Antiparticle Spectrometer) is a proposed experiment to search for the anti-deuteron particle in the cosmic rays. Astrophysically produced anti-deuterons have never been detected and so the unambiguous detection of even a single event would be very significant. Antideuterons may also be a telltale signature of dark matter annihilations. Secondary antideuterons can be produced in collisions of cosmic rays (CR) with the interstellar medium (IM). Due to the mass of such nuclei, low energy productions are quite disadvantaged leading to a reduced background in the search for low energy nuclei.

FIGURE 1.19: View of the VERITAS telescope array.

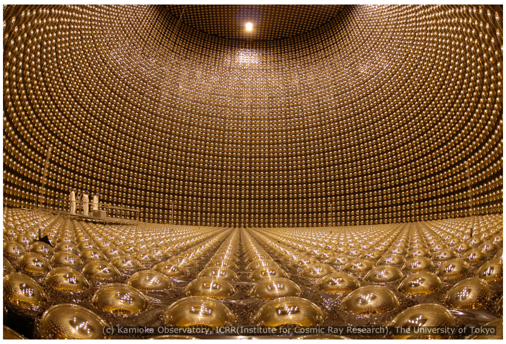

FIGURE 1.20: Internal view of the Super-Kamiokande detector.

GAPS will detect anti-deuterons with an effectively background-free method. Antideuterons, produced by the annihilation of weakly interacting massive particles (WIMPs), will be captured in the GAPS target material, resulting in an exotic atom in an excited state. This exotic atom will then quickly decay, producing X-rays of precisely defined energies and a correlated pion π signature from nuclear annihilation. The GAPS method has already been successfully tested in an accelerator environment at KEK in 2004 and 2005. A balloon prototype experiment with a TOF system and 6 Si(Li) detectors was successfully flown in June 2012. The first data acquisition is planned for 2017.

VERITAS The VERITAS telescope consists of four, 12 m diameter Davies-Cotton optical reflectors (Fig. 1.19). They focus the light from γ ray air showers, in the energy range 100 GeV-50 TeV, onto four 499 pixel PMT cameras. Its observations are mainly directed to dSph galaxies (dwarf spheroidal galaxy), they are gravitational-bound objects and are believed to contain up to $\mathcal{O}(10^3)$ times more mass as Dark Matter than as visible matter, making them widely discussed as potential targets for indirect Dark Matter observations. One of the most important results from VERITAS comes from the observation of the gamma-ray flux, perhaps originated by annihilation or decay of Dark Matter [38]. Since no signal above the background has been observed, only upper limits on the gamma-ray flux have been set considering different annihilation channels.

Super-Kamiokande The Super-Kamiokande (SK) detector, Fig. 1.20, is a kton water Čherenkov detector of cylindrical shape with height of 36.2 m and radius of 16.9 m. It is located in the Kamioka-Mozumi mine in Japan under about 1000 m rock. It consists of a inner detector with 11146 inward-facing 50 cm PMTs and an outer detector equipped with 1885 outward-facing 20 cm PMTs, serving as a cosmic ray veto counter. This detector is able to search for Dark Matter through the detection of an excess of upward-going muons (upmu). These muons are generated by the muon neutrinos (generated in DM annihilations in the Sun) which interacts with rocks that surround the detector. Muon events in the detector have been divided into three categories: **stopping**, i.e. muons with the lowest energy that stop in the detector ($E_\nu \ll 10$ GeV); **showering**, i.e. muons that produce showers in the detector and **non-showering**, which don't produce any shower. For their last results, the collaboration used data acquired in 3903 days to search for the contribution of neutrinos from WIMP annihilation in the Sun. No significant excess over expected atmospheric-neutrino background has been found and the result is interpreted in terms of upper limits on WIMP-nucleon elastic scattering cross sections under different assumptions about the annihilation channel. The current best limits on the spin-dependent (SD) WIMP-proton cross section for WIMP masses below 200 GeV/ c^2 is $1.49 \cdot 10^{-39}$ cm^2 for $\chi\chi \rightarrow b\bar{b}$ and $1.31 \cdot 10^{-40}$ cm^2 for $\chi\chi \rightarrow \tau^+\tau^-$ annihilation channels, also ruling out some fraction of WIMP candidates with spin-independent (SI) coupling in the few-GeV/c^2 mass range. [37]

Large Area Telescope The Fermi-Large Area Telescope (Fermi-LAT) is a γ-ray telescope, placed on board the Fermi Observatory, sensitive to energies from 20 MeV up to over 300 GeV. One of the goals of this telescope is to find a DM signature in the diffuse γ-ray emission. At galactic level, it is believed that the signal comes from annihilation of WIMPs in a smooth halo around the galaxy while the extragalactic signal arises from DM annihilation processes throughout the universe. For the galactic halo study, the Fermi-LAT collaboration explored the energy range $[1, 400]$ GeV. Limits were set both for annihilation and decay of DM particles [39].

IceCube IceCube is a neutrino telescope placed at the south pole that aims at the detection of the Čherenkov light emitted by muons, created by neutrinos interacting with the Antarctica ice. The neutrinos of interest are generated by Dark Matter annihilations in the Earth and in the Sun. The telescope consists of 86 vertical strings equipped with Digital Optical Modules (DOMs), Fig. 1.21, that contain a digitizer board and a PMT. Part of these strings (78) carry 60 DOMs, placed at intervals of 17 m from a depth of 1450 m up to 2450 m below the ice surface. The other 8 strings are infill-specialized for a sub-array dubbed DeepCore, placed in the central region of the telescope. IceCube is sensitive to neutrinos in the energy range from 100 GeV up to 1 TeV, while DeepCore can reach sensitivity down to 10 GeV neutrinos. This means that the entire telescope is sensitive to neutralinos down to masses of about 50 GeV.

The main background of the telescope is due to muons and neutrinos produced by cosmic rays interacting in the atmosphere. To take into account all the possible background variations, the dataset used in the last analysis was divided into three parts: summer season, focused on low energy neutrinos, and winter season which is, in turn, divided into

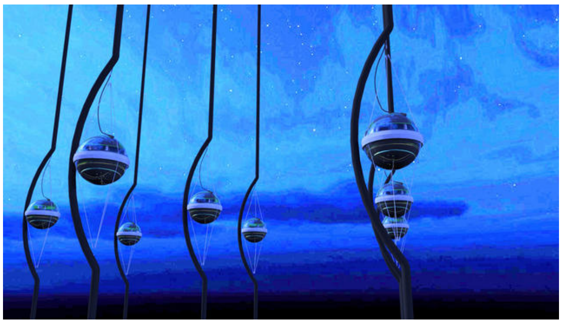

FIGURE 1.21: Representations of IceCube's DOMs.

a low and high energy sample. After all the cuts and track selection criteria, the observed distributions of the event directions have been compared with the expected background distributions from atmospheric muons and neutrinos [40] finding compatibility with the only-background hypothesis. The obtained upper limits on the expected number of signal events, μ_s^{90}, can be translated into upper limits for the annihilation rate, Γ_a, of WIMPs in the Sun that, in turn, can be converted into limits on the spin-dependent, $\sigma_{SD,p}$ and spin-independent, $\sigma_{SI,p}$, WIMP-proton scattering cross-sections. For dark matter masses between 200 GeV and 10 TeV, results on the cross-section reach a level of 10^{-23} cm^{3}s^{-1}. The IceCube data have been also used to infer information and set limits on the super heavy Dark Matter, i.e. for $m_\chi > 100$ TeV/c^2 [41]. These values of masses imply a much lower density of Dark Matter which results in a reduced sensitivity for direct detection experiments. Due to the low density, this kind of search is based on the detection of the decay products such as high energy neutrinos. Considering Dark Matter with $m_\chi \approx 100$ TeV that decays into two neutrinos, IceCube already set limits on the lifetime giving the strongest limit: $\tau > 10^{27}$ y [42].

AMS-02 The Alpha Magnetic Spectrometer (AMS), currently in its second phase AMS-02, is an antimatter search experiment placed on the International Space Station (ISS), (Fig. 1.22). In its latest results [43], the AMS collaboration found an excess in the positron fraction, at energies $>$ 8 GeV, above the expected background due to secondary positrons originate in the spallation of cosmic rays on the interstellar medium. The positron fraction excess stops at $\sim$ 275 GeV and this excess seems to be isotropic within 3%, suggesting that the energetic positrons may not be coming from a preferred direction in space.

Considering also the antiproton results from PAMELA [44], where the antiproton flux is compatible with the expected background, a scenario that consider a leptophilic Dark Matter, as possible source of positrons, is viable [45].

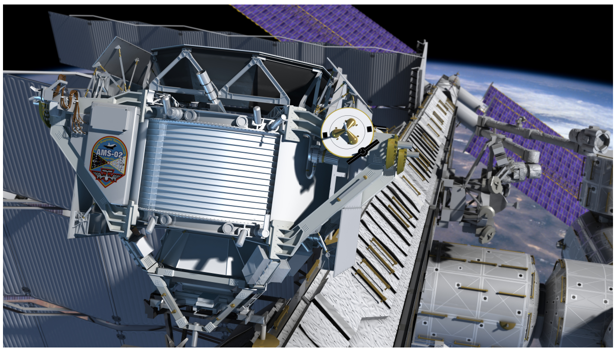

Figure 1.22: AMS-02 experiment on the International Space Station.

This kind of candidates annihilates predominately into leptons producing a large amount of energetic positrons while the antiproton flux remains suppressed. Using this kind of WIMP and considering masses above 500 GeV/c^2, the AMS-02 collaboration has evaluated the annihilation cross section for leptophilic channels that can explain the observed positron fraction [45]; the value for the annihilation cross section is of the order $10^{-23} \div 10^{-22}$ cm^{3}s^{-1} that is about 10^3 times larger than the thermal cross section.

Chapter 2

The XENON project

Among the various experimental strategies for the direct detection of Dark Matter (DM) particles, detectors using liquid xenon have demonstrated the highest sensitivities. This is the case of the dark matter experiments realized by the *XENON Collaboration*.
The first detector of the XENON project was XENON10 [46]. The main goal of this experiment was to test the possibility to realize a dual phase, LXe/GXe, detector on the kg scale to detect DM interactions. The results obtained in 2007 pushed towards the realization of a new and larger detector, XENON100 [47], based on the same detection and working principles.
Both detectors, have been placed in the interferometer tunnel at the Laboratori Nazionali del Gran Sasso (LNGS), Italy, at an average depth of 3600 m water equivalent.

The XENON100 experiment published upper limits on the spin-independent [22] and spin-dependent [48] coupling of WIMPs to nucleons in 2012 and 2013. Recently, the LUX experiment which employs a larger amounts of xenon, has confirmed and improved upon these results [23].
To significantly improve experimental sensitivities, the XENON collaboration is now focusing on the XENON1T experiment [49]: with a 30 times larger target mass, and a background reduction of a factor hundred, the maximal sensitivity to spin-independent WIMP-nucleon cross sections is expected to improve by two orders of magnitude.
The detector has been built between 2013 and 2016 and it is now in data acquisition phase.

2.1 Detection principle of a dual phase TPC

The detectors of the XENON project are based on a dual phase *Time Projection Chamber* (TPC), containing xenon in the liquid phase (LXe) and gaseous xenon (GXe). In this section we review the main properties of xenon as target and detection medium together with the Xenon dual phase TPC working principles.

2.1.1 Liquid xenon as target

The choice of LXe as active target for the DM direct detection implies several advantages:

- Self-shielding power against external background sources, due to its high density, equal to 2.96 g/cm^3;
- Xenon is not extremely demanding from the cyogenic point of view;
- The large atomic number of Xenon ($A = 131$) increases the expected WIMP interaction rate, since the WIMP-nucleus cross section scales with A^2;
- Xenon has about ten stable isotopes, while instable ones are very short-lived. Hence, it is a rather pure material, which is a mandatory requirement for a search of very rare events like WIMP scatterings. There are two isotopes with nonzero spin: ^{129}Xe (spin 1/2) and ^{131}Xe (spin 3/2). This allows to study also the dependence of the WIMP-nucleus cross section on the spin, thus providing more information about the Dark Matter nature;
- Xenon is an excellent scintillator, since emits about $5 \cdot 10^4$ photons per MeV deposited, ($\lambda = 177.6$ nm, i.e. VUV photons) and has also a good ionization yield ($6 \cdot 10^4$ electron-ion pairs per MeV). Therefore, an interaction produces both a large amount of both charges and photons.

2.1.2 Xenon scintillation light

The xenon scintillation is ruled by de-excitation of excimers, i.e. excited xenon dimeric molecules (Xe_2^*), which are formed after recoil events through direct excitation or recombination of ionization products. In the direct excitation process an excited state Xe* is promptly formed, leading to scintillation through the following decay chain:

$$\begin{aligned} \mathrm{Xe}^* + \mathrm{Xe} + \mathrm{Xe} &\rightarrow \mathrm{Xe}_2^* + \mathrm{Xe} \\ \mathrm{Xe}_2^* &\rightarrow 2\mathrm{Xe} + h\nu\ . \end{aligned} \tag{2.1}$$

After ionization in the xenon target, the Xe^+ ions can form a molecular state and a freed electron can recombine, producing scintillation at the end of the chain:

$$\begin{aligned} \mathrm{Xe}^+ + \mathrm{Xe} &\to \mathrm{Xe}_2^+ \\ \mathrm{Xe}_2^+ + e^- &\to \mathrm{Xe}^{**} + \mathrm{Xe} \\ \mathrm{Xe}^{**} &\to \mathrm{Xe}^* + \mathrm{heat} \\ \mathrm{Xe}^* + \mathrm{Xe} + \mathrm{Xe} &\to \mathrm{Xe}_2^* + \mathrm{Xe} \\ \mathrm{Xe}_2^* &\to 2\mathrm{Xe} + h\nu\,. \end{aligned} \tag{2.2}$$

Due to the different configuration of the energy levels of dimers and atoms, the photons emitted by dimers are not re-absorbed by the atoms making LXe transparent to its own scintillation light. The scintillation light in LXe has two decay components characterized by two different decay times: the singlet (S) and triplet (T) states of the excited dimers Xe_2^*. The fast scintillation component is due to the S state and its decay time can vary under intense electric fields. For instance, with a 4 kV/cm electric field, the decay times after the interaction of relativistic electrons with xenon atoms are: (2.2 ± 0.3) ns from the singlet states decays and (27 ± 1) ns from triplet states [50].

2.1.3 Signals produced in the TPC

A schematic view of the TPC structure is shown in Fig. 2.1 left; starting from the bottom the TPC is closed by the Cathode (at negative voltage) while on its top it is closed by the Gate mesh (grounded). This structure encloses the LXe active region, called *sensitive volume*, that represents the volume used to detect the interactions and which is available for the electron drift. Along the vertical axis equally spaced thin copper rings are properly distributed, together with the Cathode and the Gate mesh, to generate a uniform electric field.

Above the Gate mesh there is the Anode and the LXe/GXe interface is set between them. Gate mesh and Anode produce the extraction field which has a strength of $\mathcal{O}(10)$ electrons kV/cm, that guarantees an extraction efficiency close to 100%.

Particles interacting in LXe produce a prompt scintillation signal, called **S1**, through excitation, and ionization electrons. The electrons can recombine, participating to the S1 signal, or can be drifted by an appropriate electric field towards the liquid-gas interface where they are extracted by the strong extraction field, and a light signal, named **S2**, is generated by proportional scintillation in the gas. The S2 signal is delayed by the time occurring in the drift from the interaction site to the liquid/gas interface.

Two PMT arrays, one on top of the TPC inside the GXe and one at its bottom below

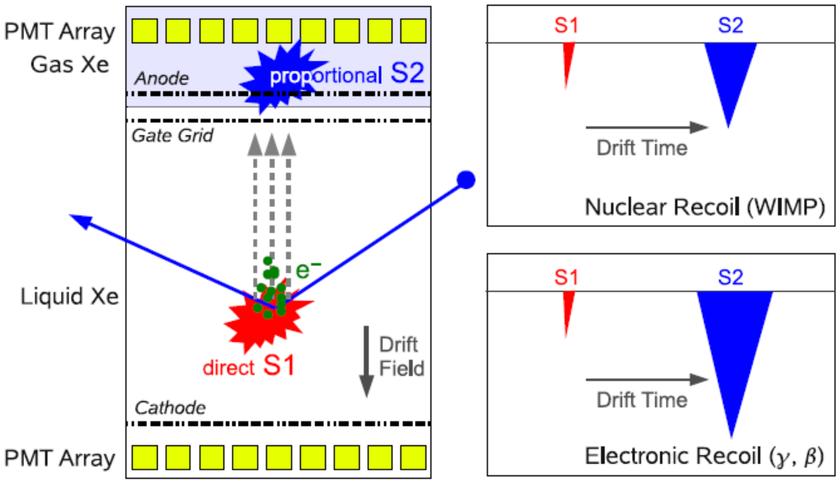

FIGURE 2.1: (Left) Schematic view of the XENON TPC along with its working principle. (Right) Illustration of characteristic wave forms due to different kinds of events, NR and ER.

the cathode, in LXe, are used to detect the scintillation light. From the pattern of the hit PMTs in the S2 signal, the (x, y) position of the events is determined, while from the time difference between S1 and S2 signals it is possible to infer the z coordinate. Combining all these informations, a 3D vertex reconstruction can be achieved. The knowledge of the interaction point allows the selection of those events located in the inner part of the LXe, usually called *fiducial volume* (FV). Since the majority of background events are expected to be found in the outermost part of the TPC, using the most external volume as shield, the background from external sources can be remarkably reduced.

The S1 and S2 signals are also used to lower the background, thanks to their different distribution in case of either electronic (ER) or nuclear recoils (NR). From the measured S1 and S2 it is possible to achieve a satisfying discrimination power between ER and NR events. Moreover, single scatter interaction (expected from WIMPs) can be distinguished from multiple scatters thanks to the presence of more than one S2 signal in the latter case.

The scintillation efficiency, i.e. the light output per unit energy deposited, for ER and NR is significantly different; therefore it is usual to define two energy scales: keV_{ee} (or keV_e) for ER events and keV_{nr} (or keV_r) for NR events. They are defined so as to avoid misinterpretation of the event energy in the case it is an ER or NR.

An example of the S_1 and S_2 signals pattern from NR and ER is shown in Fig. 2.1 (right).

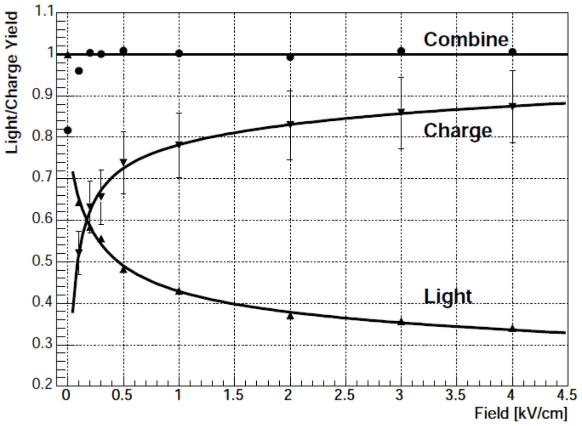

Figure 2.2: Light and charge yield as a function of drift field for 662 keV$_{ee}$ γ-rays from ^{137}Cs [51].

2.1.4 Discrimination of ER and NR

The ability to discriminate among different particles is essential for a Dark Matter experiment. WIMPs are expected to produce NR while most of the background radiation produces ER. Particles with different Linear Energy Transfer (LET), dE/dx, have different S2/S1 ratio and this allows to discriminate among them. Indeed, a NR has a higher recombination rate, due to its higher LET, than an ER. A higher recombination gives a lower S2 and a higher S1 and ultimately a lower S2/S1 ratio. This characteristic of the signals implies the anti-correlation between ionization and scintillation signals, which is experimentally observed (Fig. 2.2).

Hence, using the ratio of the signals S1 and S2 as discrimination parameter, it is possible to distinguish between the two types of recoil. Having such a separation between the ER and NR bands, in the S2/S1 parameter, it is possible to set a discrimination level for the ER which allows to reach the desired background level.

The detector response to ER and NR events is studied through calibration with sources of photons (for ER) or neutrons (for NR). As example, the XENON100 performance is shown in Fig. 2.3 [22], where the ER band (blue) is clearly distinguished from the NR band (red).

With the separation achieved by XENON100, it is found that a 99.5% ER discrimination corresponds to a 50% acceptance of NR events, while 99.75% ER discrimination gives 40% NR acceptance [22].

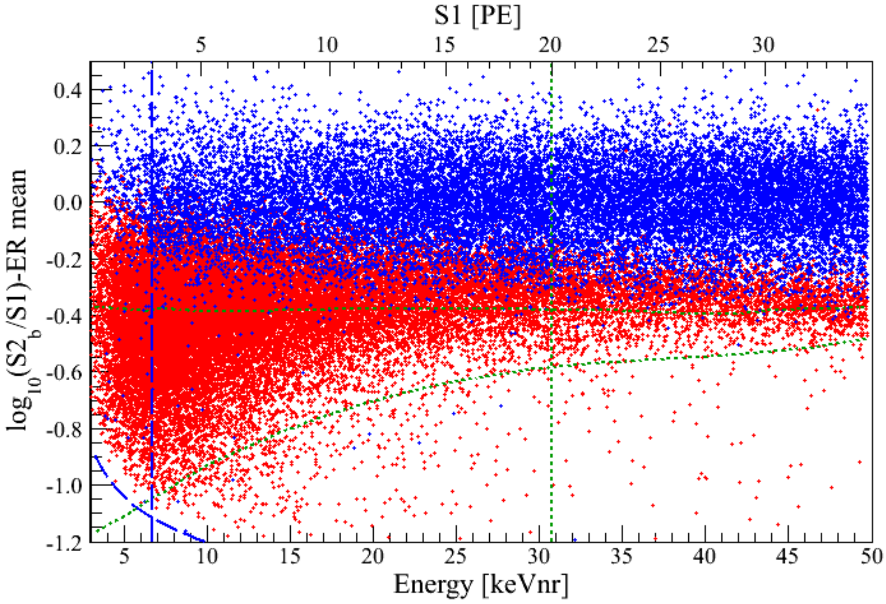

FIGURE 2.3: Distribution of the flattened discrimination parameter, $\log_{10}$(S2/S1), as function of the recoil energy achieved with the XENON100 experiment [22]. The ER band (red points), obtained from ^{60}C and ^{232}Th calibration data, is showed together with the NR band (blue points), from the ^{241}AmBe calibration.

2.2 The XENON experiments

The XENON project started with the XENON10 experiment, with a target mass of the order of 10 kg.

The XENON10 experiment has been followed by XENON100, whose xenon mass is about 170 kg. The mass of the XENON1T experiment has been increased of a further factor 10. Finally, an upgrade to a xenon mass to about 7 tonnes, named XENONnT is already foreseen by the Collaboration.

In the following, we briefly review the main results of XENON10 and XENON100, while a more detailed discussion is dedicated to XENON1T.

2.2.1 XENON10

The XENON10 experiment [46], installed in 2005, has been in operation until October 2007. The TPC was made of a PTFE cylinder with an inner diameter of 20 cm and a height of 15 cm. The amount of LXe contained inside the TPC was 15 kg, with 5.4 kg used as fiducial volume. In 2008, the Collaboration published the results of the 58.6 days run, setting upper limits on both SI and SD WIMP-nucleon cross section. XENON10 reached a sensitivity at 90% confidence level to SI cross sections of 8.8×10^{-44} cm^2 for a 100 GeV/c^2 WIMP mass and 4.5×10^{-44} cm^2 for $m_\chi = 30$ GeV/c^2 [52] (see Fig. 2.4).

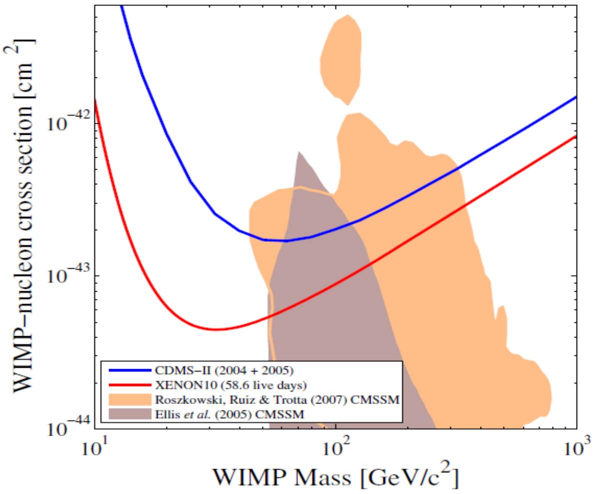

FIGURE 2.4: Cross section limit, 90% CL, on spin-independent WIMP interactions (red line), from the XENON10 58.6 live-days dataset [52]. The blue line is the best limit from CDMS experiment [53]. The shaded areas represent the allowed parameter region in the constrained minimal supersymmetric models.

Concerning the SD case, a limit for neutron couplings of 5×10^{-39} cm^2 was set for 30 GeV/c^2 WIMP mass [54]. The XENON10 sensitivity plot for SD WIMP interactions is shown together with the result of XENON100 in fig. 2.6.

2.2.2 XENON100

The XENON100 experiment [47] started in 2008 at LNGS. The XENON100 TPC has a radius of 15.3 cm and a height of about 30.5 cm. The LXe amount was increased to 161 kg, with 62 kg used as active volume in the TPC and the remaining as an outer active veto; In order to be sensitive to a DM interaction, one of the goals of this experiment was to lower the sensitivity by two orders of magnitude with respect to XENON10. Such result has been achieved thanks to a larger target, but also thanks to a factor 100 of background reduction through an accurate screening and selection program for all detector construction materials.

One of the most important results has been obtain with a run of 225 live-days. The analysis showed no evidences for Dark Matter. Two events have been found in the energy region of interest for the WIMP search, but this number is compatible with the expected background (1.0 ± 0.2) events. A second data analysis was carried on combining three runs summing up to 477 live days from January 2010 to January 2014. A blind analysis was applied to all the runs prior to combining the results. A profile likelihood analysis using an energy range of $(6.6 - 43.3)$keV$_{nr}$ sets a limit on the elastic, spin-independent WIMP-nucleon scattering cross section for WIMP masses above 8 GeV/c^2, with a minimum of $1.1 \cdot 10^{-45}$ cm^2 at 50 GeV/c^2 and 90% confidence level. The

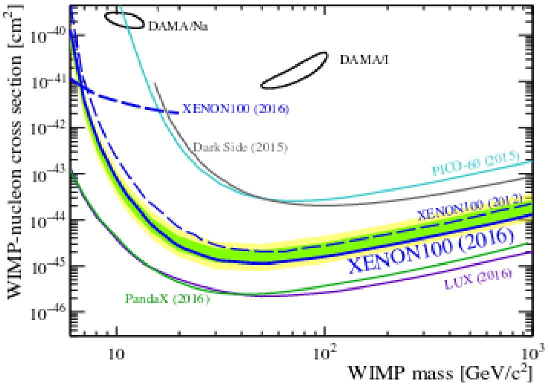

FIGURE 2.5: Spin-independent cross section limit (blue line) and 1σ (green band) and 2σ (yellow band) expected sensitivity regions at 90 % C.L. from the combined analysis of the three XENON100 science runs. For comparison, a subset of other experimental limits (90 % C.L.) and detection claims (2σ) are also shown.[55].

constraints on the elastic, spin-dependent WIMP-nucleon cross sections were obtained with the same data set upper limits on the WIMP-neutron (proton) cross section with a minimum of $2.0 \cdot 10^{-40}$ cm^2 ($53 \cdot 10^{-40}$cm^2) at a WIMP mass of 50 GeV/c^2 at 90 % confidence level [58]. The exclusion limits as function of the WIMP mass are shown in Fig. 2.5 and 2.6.

2.2.3 XENON1T

The XENON1T experiment [49] is located in the Hall B, shown in Fig. 2.7(a), of the Gran Sasso Underground Laboratory (LNGS). The construction of the experiment started in 2013 and has been terminated in 2015. After several months of commissioning, XENON1T (Fig. 2.7(b)) is now in science data taking and first results are expected by summer 2017.

The total amount of about 3 tonnes of LXe is contained in a double vessel vacuum insulated cryostat made of low activity stainless steel (SS), 5 mm thick. The dimensions of the inner cryostat are chosen to host the XENON1T TPC (Fig. 2.8), while the outer one is increased in order to host also the future enlarged version of the experiment, XENONnT. Both vessels are composed by a cylindrical part and two domes; the top dome is connected to the central part through a flange whose thickness is 50 mm. The upper domes have a central port from which the cryostat is connected to the XENON1T cryogenics system, via a long double-wall vacuum insulated tube.

The target consists of about 2 tonnes of LXe, defined laterally by an almost cylindrical structure of 24 polytetrafluoroethylene (PTFE) interlocking panels: the radius of the TPC is 479 mm. The target volume is viewed by two arrays of PMTs: one made of 121 PMTs in a compact hexagonal structure directly immersed in LXe in the bottom,

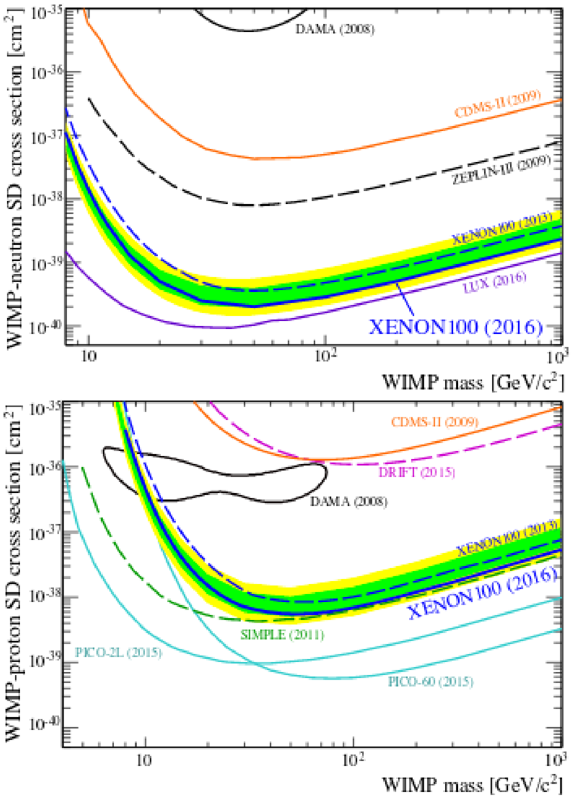

FIGURE 2.6: Spin-dependent cross section limit (blue line) and 1σ (green band) and 2σ (yellow band) expected sensitivity regions at 90 % C.L. from the combined analysis of the three XENON100 science runs. The top (bottom) panel shows the individual neutron (proton) only cross sections. For comparison, other experimental limits (90 % C.L.) and detection claims (2σ) are also shown. CDMS [56], ZEPLIN-III [57].

and one made of 127 PMTs placed in concentric rings in the gas phase above the target volume.

The radius of the bottom array is the same as the TPC, while the top one is slightly larger to guarantee a good position reconstruction even at the edge of the TPC. The space among the PMTs is covered with PTFE to reflect the UV light and ensure a good light collection efficiency. The structure of the TPC is reinforced on the outside region through PTFE pillars and copper rings. Additional PTFE and copper disks support the two PMT arrays.

The electric fields in the TPC are generated through electrodes made of SS meshes welded onto SS rings. There are two electrodes on the bottom of the TPC: the cathode and a second one to screen the bottom PMT array. At the liquid gas interface there is a stack of two electrodes, ground and anode, separated by 5 mm; another mesh is used to protect the top PMTs. The distance between the cathode and the ground meshes, which defines the active region, where both the light and charge signals can be generated, is 967 mm. A stack of 74 field shaping rings, made of copper and placed just outside the PTFE lateral panels, assures the uniformity of the electric field along the TPC.

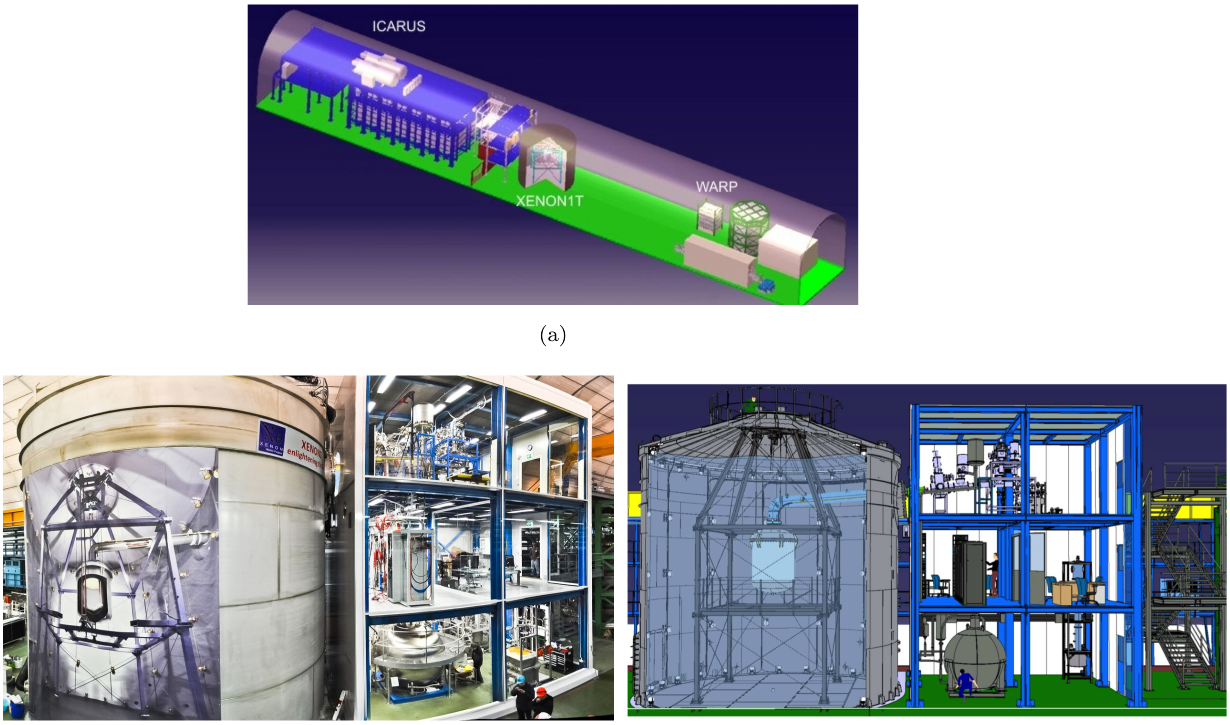

(a)

(b) (c)

FIGURE 2.7: (a) Schematic overview of the Hall B of the LNGS, (b) and (c) picture and drawing of the XENON1T detector: the Muon Veto water tank containing the TPC, the Service Building which hosts the cryogenic and purificiation system, the DAQ equipment, the distillation column, and the emergency recovery system.

The liquid level in the proportional amplification region is adjusted between the gate and the anode electrode, and kept constant, by using the concept of a diving bell with an adjustable overflow tube coupled to a linear motion feedthrough [47]. The bell closing the gas phase region is made of SS, 5 mm thick on the top and 3 mm in the lateral part. This solution has the advantage that the LXe outside the bell can rise above the top PMT array.

In this way we have a layer of LXe, about 5 cm thick, above the Bell and all around the TPC (outside of the field cage, between the rings and the cryostat wall); a 3 cm LXe layer is kept below the bottom PMT array. In the initial operation phase of the experiment this LXe layer will act as a passive shield to reduce the background from outside; in a second phase it can be instrumented with 1” PMTs and PTFE panels to be operated as an active veto.

2.2.3.1 The background

In order to increase the sensitivity of WIMP-nucleus cross section it is necessary to reduce the background sources.

The principal sources of backgroud signals are:

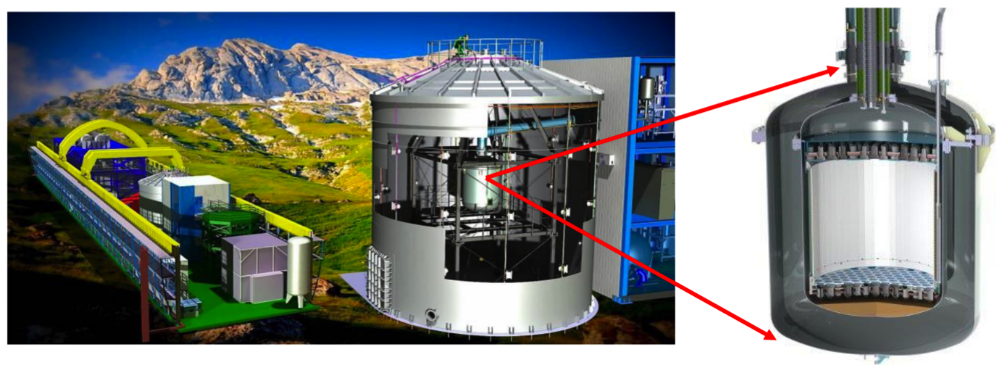

FIGURE 2.8: Picture of the XENON1T TPC and cryostat inside the Muon Veto System.

- Internal background
- Intrinsic background
- External background

2.2.3.2 Internal background

The internal background is due to the radioactivity of materials constituiting the detector. For the construction of XENON1T a screening campaign was carried on, the materials with the lowest contaminations from radioactive nuclei were chosen.
The most dangerous electromagnetic backgrounds comes from the γ emitted in the ^{238}U and ^{232}Th chains and from the decay of ^{60}Co, ^{40}K and ^{137}Cs. The γ emitted might cause electron recoil. An optimized choice of the fiducial volume of xenon used in the TPC using its external part as a shield, allows the reduction of the internal background. From Monte Carlo simulations it was estimated that, using part of the xenon as a shielding, the number of background events expected is 0.07 ev/ton/yr [59].
The nuclear recoil due to reactions of the type (α, n) are another source of background. These reactions are produced by the decay chain of U and Th, which are present in the material of the detector. Neutrons produce multiple interactions, a detailed Monte Carlo simulation shows a number of expected events of 0.6 ev/ton/yr.
To conclude, the total expected internal background is lower than the number of events, $\sim$ 20 ev/ton/yr, expected for a WIMP of mass 100 GeV and cross section 10^{-47} cm^2.

2.2.3.3 Intrinsic background

The intrinsic background is another source of dangerous events. It is due to some radioactive isotopes that are uniformly distributed in LXe (^{85}Kr , ^{222}Rn).
Kr decays β with an energy of 687 keV and half life of 10.76 years. We require a Kr

contamination lower than 1 ppt. The commercial xenon has a contamination of 1 ppm and requires to be purificated through a dedicated distillation column.
Also Rn can be a potential source of intrinsic background since it is mixed inside the LXe and among its daughters there is ^{214}Pb, a beta emitter. We require to have a Rn contamination inside the LXe less than 1 μBq/kg.

2.2.3.4 External background

The external background is due to different factors:

- Natural radioactivity: low energy ($<$ 10 MeV) γ and neutrons from the rock;
- Neutrons at high energy (up to the order of tens GeV) inducted by the cosmic muons.

Both can be reduced surrounding the detector with a thick water layer, contained in the so called *Water Tank*. The layer of water is about four meters thick in each direction around the detector and, for gammas, it is equivalent to the shielding of 20 cm of lead. The presence of water allows a reduction of the γ flux of a factor 10^5 (Fig. 2.9) and makes negligible the contribution of neutrons produced in the (α,n) reaction induced by ^{238}U and ^{232}Th decay in the rock and concrete of the experimental hall. As an example, one meter of water is enough to lower the value of the neutron flux with energy in the scale of MeV of a factor 10^6.
Neutrons induced by cosmic muons have an energy up to tens of GeV and they might cross the Water Tank, enter the TPC and mimic a WIMP-like interaction. This is the reason why the TPC is surrounded by a Water Tank instrumented with photo multipliers (PMTs): during their path in water muons emit light through Čherenkov effect. If a muon-like event is seen, a trigger is sent to the TPC, in this way it is possible to veto that specific event.
This system is called **MuonVeto** and will be described in detail in Chapter 3. A Monte Carlo simulation [59] showed that with 4 meters of water, up to the 99.5% of neutrons are moderated and stopped.
The last categories of neutrons are the ones producted by the interactions of muons with the materials of the detector. These neutrons, if the corresponding muons aren't detected in the Water Tank, are extremely dangerous . From the simulation it was also shown that the biggest part of this kind of neutrons is generated in the cryostat.

To conclude, a Water Tank instrumented with PMTs is enough to reduce the γ and neutrons background up to the desirable levels. The total background expected from the Monte Carlo simulation is about 4 event in the 1 tonne fiducial volume in 2 years of

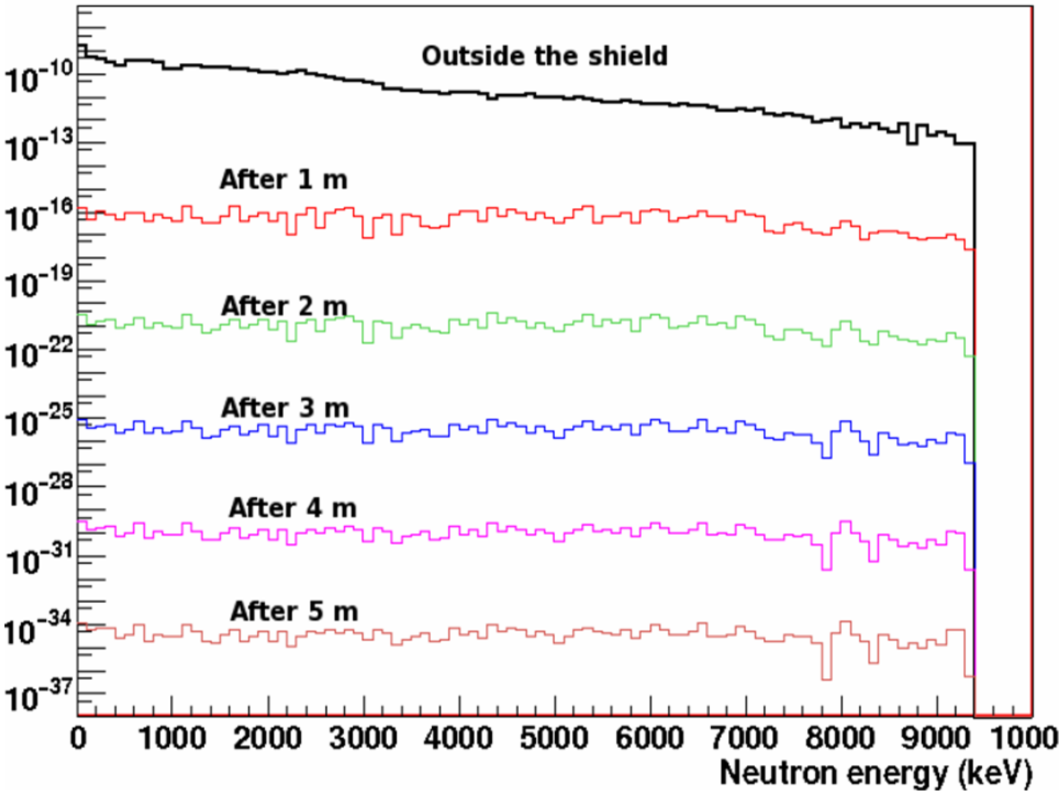

FIGURE 2.9: Flux of neutrons coming from the concrete measured in the HallB al LNGS (black line) and MonteCarlo simulation of the energetic spectrum of neutron for different thickness of the layer of water. [60].

exposure, mostly coming from the intrinsic Rn contamination [61]. With this background prediction, the XENON1T experiment will be sensitive to WIMP-nucleon scattering cross section of $1.6 \cdot 10^{-47}$ cm^2 at $m_\chi = 50$ GeV/c^2 , with 90% CL, one order of magnitude better than the best limit of LUX [24]; A final comparison, between the limits from various experiments is shown in Fig. 2.10. The orange dashed line represents the neutrino coherent bound, below which the NR from neutrinos will be the dominant background process. It represents an irreducible source of events since it mimics a WIMP-nucleon interaction and new detection techniques (exploiting the event direction) will be required to probe lower values of the cross section.

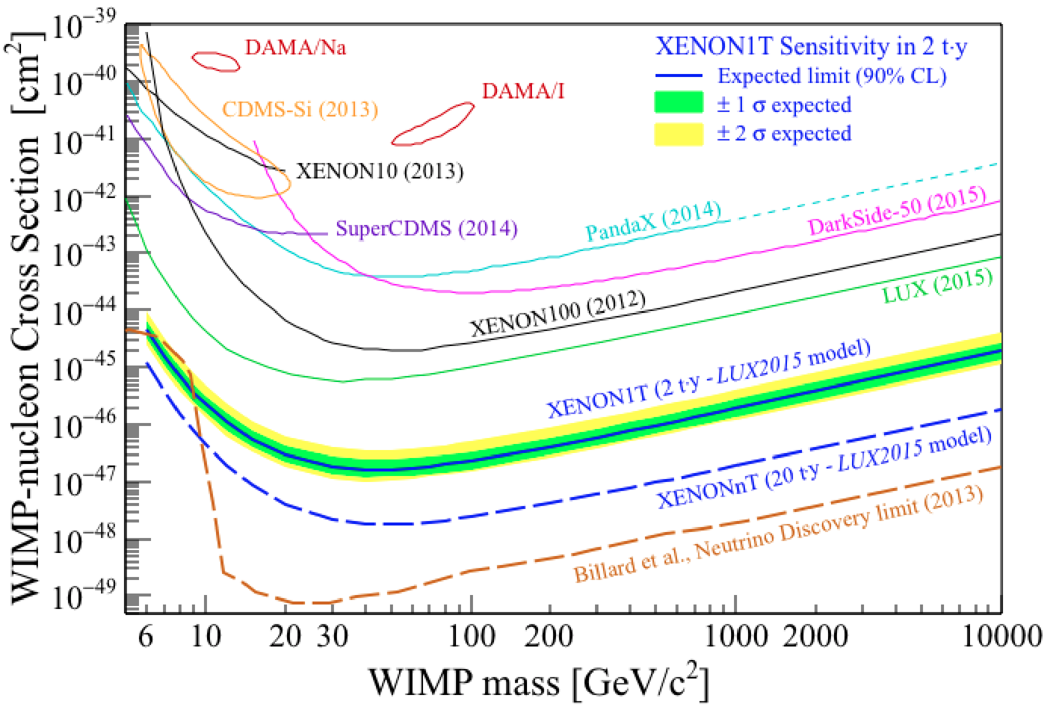

FIGURE 2.10: Comparison between sensitivities, at 90% CL from different experiment: DAMA exclusion region (dark red), PandaX (light blue), XENON100 (black), DarkSide-50 (purple), LUX (green), XENON1T (blue), XENONnT (blue dashed) and the neutrino bound (orange dashed). Also superimposed is the XENON1T sensitivity (yellow and green bands with the solid blue curve inside).

Chapter 3

The Muon Veto

This chapter is dedicated to the description of the Muon Veto system of the XENON1T experiment.

In the first section a detailed description of the Muon Veto design, electronics and data processing is reported. In the second section, we describe the Monte Carlo simulation of the Muon Veto. The last section of this chapter is dedicated to a comparison between the Muon Veto simulation and experimental data and to the evaluation of the Muon Veto tagging efficiency.

3.1 The Muon Veto

3.1.1 Design

The XENON1T experiment is located at Gran Sasso Underground Laboratory at average depth of 3600 meter water equivalent.

Due to the overlaying rock, the flux of cosmic muons is reduced by a factor $\sim 10^6$ to $(3.31 \pm 0.03) \cdot 10^{-8}$ $\text{cm}^{-2}\text{s}^{-1}$ [62], with mean muons energy of $\sim$ 270 GeV [63]. Such particles, together with their cascades, generated in the rock and concrete of the laboratory, can produce both ER and NR background for XENON1T. The nuclear recoil background is more dangerous since neutrons, produced by muons in the spallation processes on nuclei or in electromagnetic and hadronic showers, have energies up to tens of GeV. They can thus penetrate also large shields and mimic a WIMP signal in the TPC. Therefore, several efforts have been dedicated in designing a Muon Veto system that can tag and reject events possibly related to muons. [59]

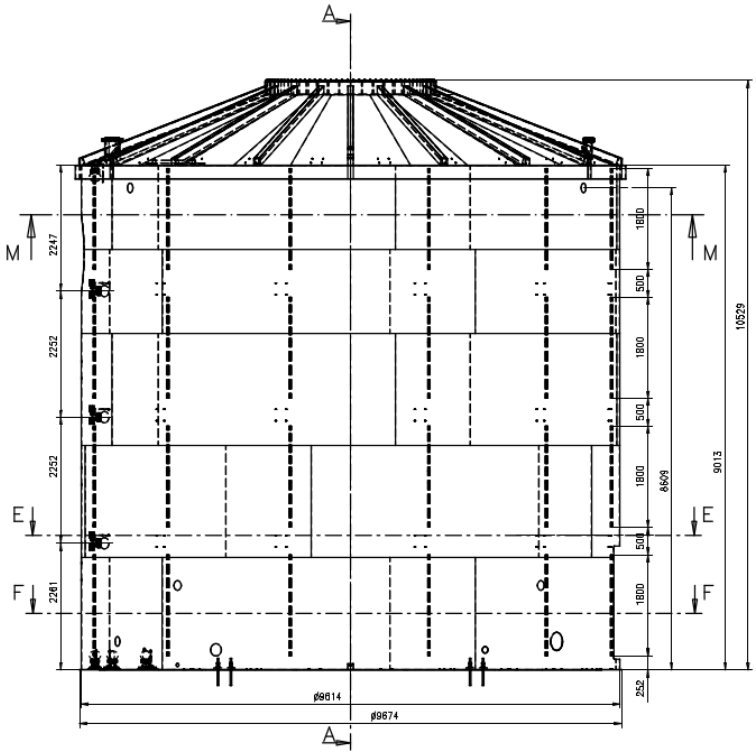

Figure 3.1: Schematic view of the XENON1T Muon Veto water tank.

The Muon Veto of XENON1T is a water Čherenkov detector made of a tank with a cylindrical body, 4.8 m of radius and 9 m height, with a truncated cone roof, for a total height of 10.5 m, (Fig. 3.1), filled with purified water.

The XENON1T TPC is placed in the center of the Water Tank (Fig. 3.2), thus resulting surrounded by $\sim 4\,m$ of water in all directions. The Muon Veto system is based on the detection of the Čherenkov light emitted by particles passing through the water. The light is seen by 84 PMTs, model Hamamatsu R5912ASSY, whose quantum efficiency in the range [300, 600] nm is about 30%. They are high quantum efficiency (HQE) phototubes, with 10 dinodes and a bialkali photocatode.

The PMTs are arranged in five rings, one on top, at 9 m from ground, and one on the bottom of the water tank, each made of 24 photomultipliers, plus 3 equally spaced rings of 12 PMTs each, along the vertical wall of the tank, looking inwards. The photomultipliers are installed on the internal wall, roof and floor of the water tank.
The inner surface of the Water Tank is covered by a reflective foil, DF2000MA, (Fig. 3.3), which has a reflectivity close to 100% between 400 and 600 nm wavelengths. It acts also as a wavelength-shifter to better overlap the Čherenkov light spectrum with the high quantum efficiency region of the PMTs.

In order to calibrate and equalize PMTs gain, the Muon Veto is provided with two independent calibration systems. Each PMT can be calibrated using an optical fiber

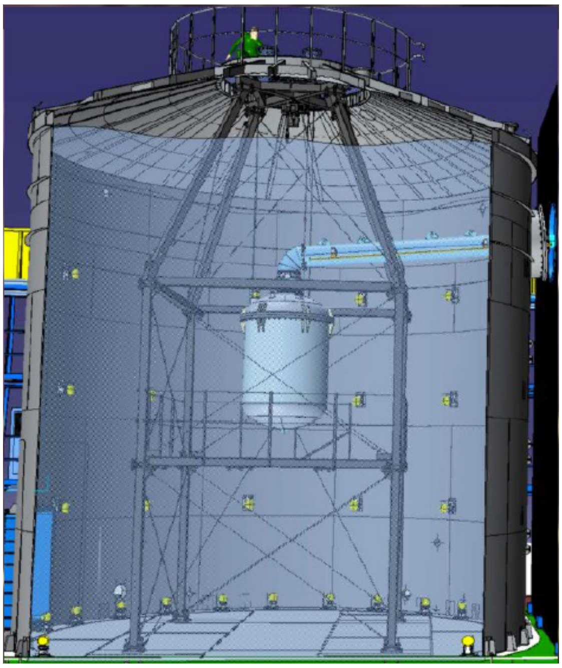

FIGURE 3.2: Design of the Muon Veto with the detector and its support structure at the center of the water tank.

placed in front of it, with light from a blue LED ($\lambda = 470$ nm). The LED, driven in voltage, is interfaced to a bundle of 8 optical fibers grouped together at one end. The other end is anchored to a vertical support, placed next to the PMT. There is a PTFE (politetrafluoroetilene) surface attached to the vertical support, to reflect the light, as shown in Fig. 3.4.

The second calibration system uses four Diffuser Balls (DB) located inside the water tank which illuminate all the PMTs. The position of the diffuser balls is shown in the drawing in Fig. 3.5.

The scheme of the calibration system is shown in Fig. 3.6.

3.1.2 The Muon Veto electronics

In this section the stream of information from the single PMT hit to the generation of the global trigger is explained.

The analog signals coming from the 84 Muon Veto PMTs are recorded by means of 11 commercial 8 channels digitizer CAEN mod. V1724 (14 bit, 0.5 V_{pp}, 100 MS/s). In Fig. 3.7 is shown an example of a waveform acquired from a Muon Veto PMT.

The digitizer can store sampled signals both from an external and internal trigger. The Muon Veto system is provided with a trigger unit, CAEN mod. V1495, which is designed (by means of custom firmware) to generate a global trigger to the Muon Veto following

Figure 3.3: Internal view of the Water Tank.

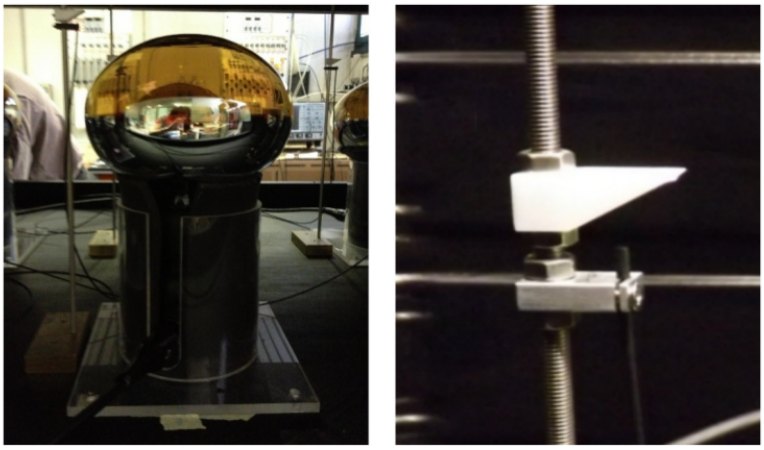

Figure 3.4: To the left the LED calibration system for photomultipliers. To the right the piece of PTFE in which the light is reflected before reaching the photocatode.

a predefined condition.

Two basics trigger modes are implemented in the V1495: the calibration trigger mode and the normal trigger mode.

In the calibration trigger mode an external trigger starts the LED pulsers, generating the light pulse for PMTs calibration and the digitalization of PMTs signals.

In normal trigger mode, the trigger is generated if a custom designed trigger condition is fulfilled. In particular, the trigger condition is set first at the level of single PMT signal amplitude (Thr) and number of consecutive samples over the threshold (TOT).

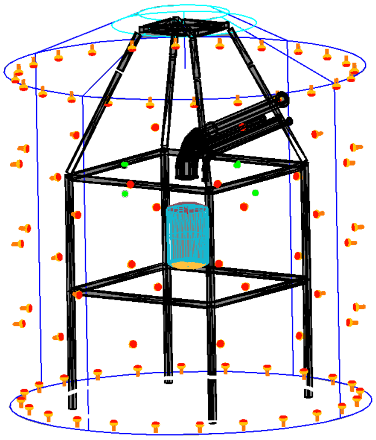

FIGURE 3.5: Position of the Diffuser Balls (green dots) inside the Water Tank.

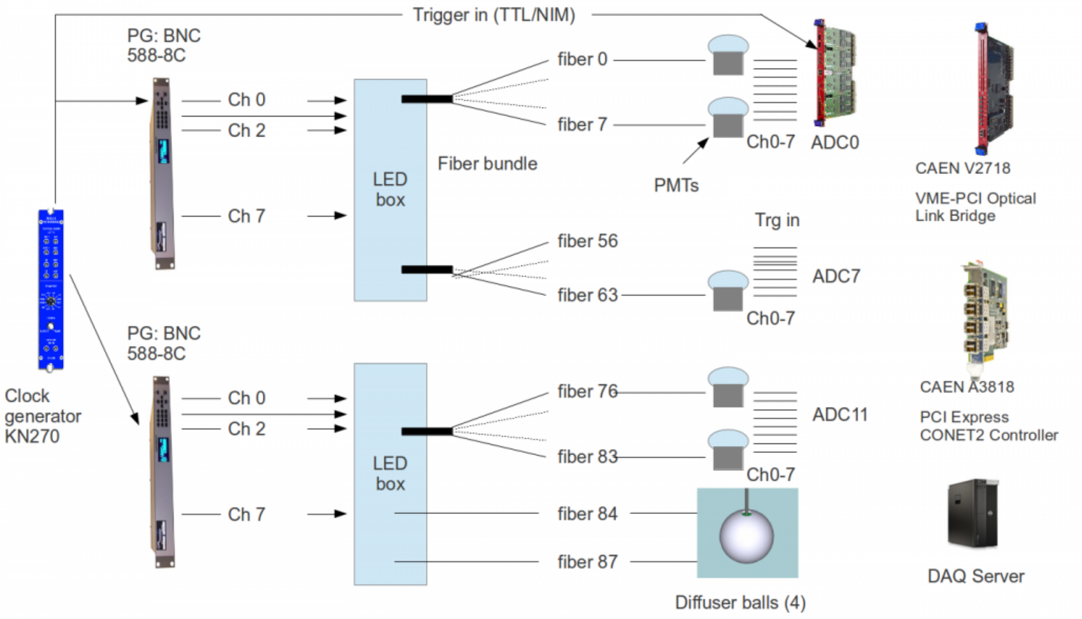

FIGURE 3.6: Working scheme of the calibration system.

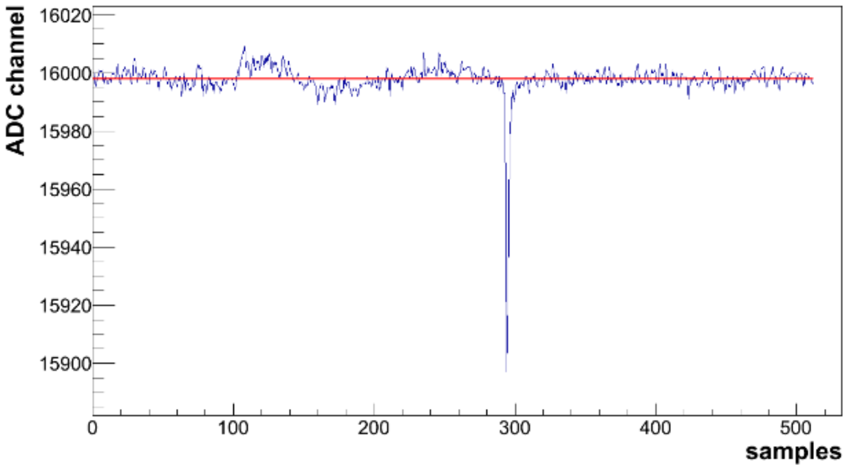

FIGURE 3.7: Example of a waveform acquired using a CAEN V1724 digitizer. The red line represents the baseline, which is set to 16000 ADC counts.

When a digitised channel (i.e. a PMT) overcomes this trigger condition a corresponding signal is sent to the V1495 trigger unit.
If the number of PMTs satisfying the condition in a time window $T = 300$ ns is greater than or equal to a programmable number N of PMTs, the trigger unit generates a global trigger and all 84 PMTs digitized signals are stored.
Finally, the Muon Veto system needs to be synchronized with the TPC (in order to behave as a Veto), so its electronics is completed by a Timing Unit, which is used to:

- assign an absolute time to events that have triggered the Muon Veto;
- produce a 50 MHz clock to synchronise all the Muon Veto system digitizers;
- produce a 0.1 Hz *SYNC* clock signal, distribuited also to the TPC, used as a common time reference.

The scheme of Muon Veto electronics and flow of information is shown in Fig. 3.8: the single channel (PMT) over threshold signal is sent to the trigger unit (blue lines); if the general trigger condition is fulfilled, a global trigger is generated and distributed to all 11 digitizers (red lines) starting the acquisition process of all 84 channels simultaneously. The 50 MHz clock signal, produced by the Timing Unit, is distributed to the first digitizer of the Muon Veto system and then propagated to the other 10 boards (violet lines) to syncronize the 11 fADCs. Finally the Timing Unit produces also the 0.1 Hz SYNC signal (green lines) that goes to both the TPC and the Muon Veto.

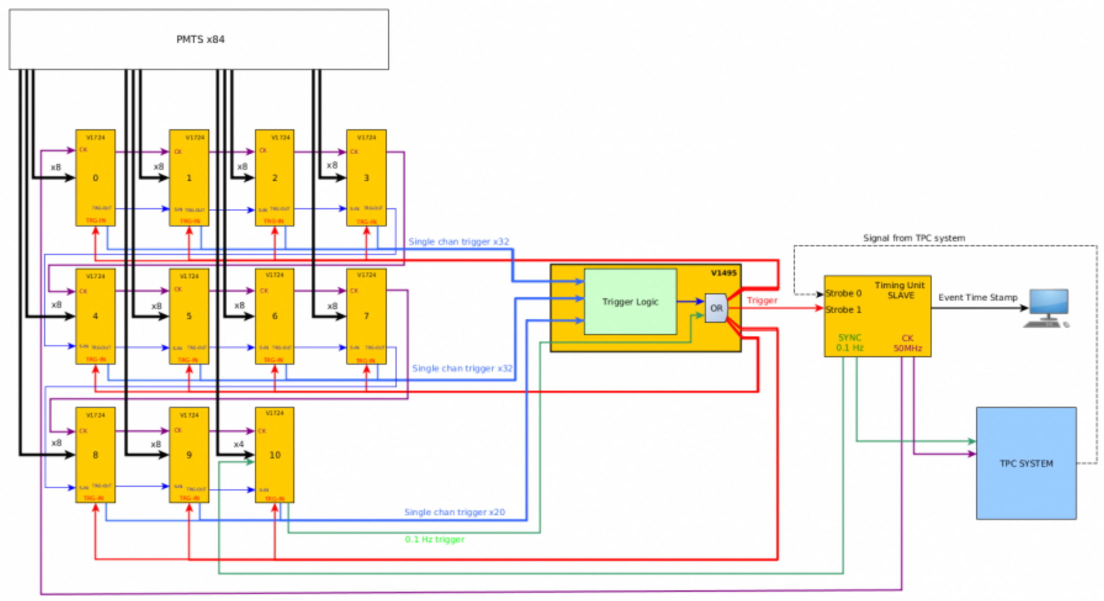

FIGURE 3.8: General scheme of the electronics.

3.1.3 PMT Calibration and Trigger setup

The Muon Veto calibration system is used to equalize and monitor the PMTs gain. Indeed the calibrations are performed on a weekly base. In particular, the PMTs high voltages (HV) are set in order to have a mean value of the charge collected at PMT anode equal to 1 pC as response to the extraction of a single photoelectron at the photocathode. Fig. 3.9(a) shows the charge of the distribution obtained for 6 equalized PMTs. The mean value of the single photoelectron charge are equalized to 1 pC within few %. From the gain equalization procedure we derive also the trigger threshold for the single PMT. Together with the charge spectra we build the amplitude spectra corresponding to the single photoelectron (Fig. 3.9(b)) and extract for each PMT the mean signal amplitude for the single photoelectron and use it as single channel trigger threshold. The measured average threshold obtained are of the order of 3 mV, i.e. about 90 ADC counts, as also shown if Fig. 3.9(b).
On the basis of this equalisation we can then set various trigger condition both on the single channel, like the *threshold* and the *TOT* or on the trigger unit.

In this preliminary data acquisition period, in order to have a stable running condition, the Muon Veto trigger was set to:

- At the single channel (i.e. PMT) level , we require an amplitude signal of 1 pe and $TOT = 1$.
- The global trigger condition is: 8 PMTs in coincidence in a 300 ns wide time window.

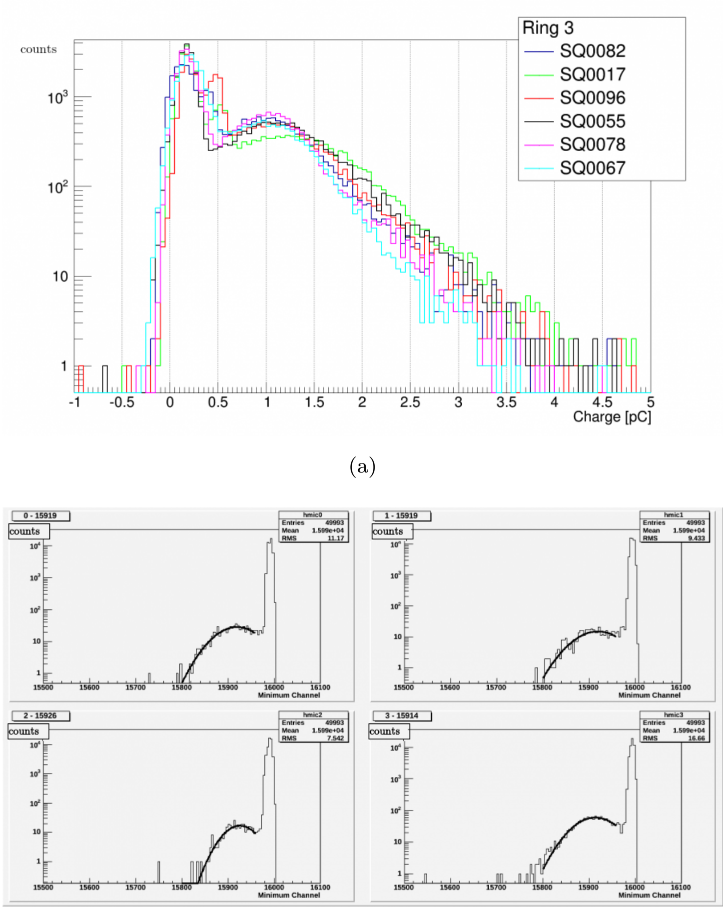

(a)

(b)

FIGURE 3.9: (a) Charge spectra of 6 PMTs in water, (b) Following an LED or Diffuser Balls calibration, channel by channel is picked the maximum amplitude in the time window in which we expect the LED/DF signal to appear. The distribution of maximum amplitudes for each channel is built and the average value in the signal region is extracted. In this example the extraction of the values of the thresholds for 4 different channels.

In the next paragraph we report the data processing and data analysis work.

3.1.4 Data Analysis

The data analysis for XENON1T and for the Muon Veto is done using **PAX** processed datasets.

PAX stands for **P**rocessor for **A**nalyzing **X**ENON and is a powerful tool used for digital signal processing and other data processing on the XENON100 and XENON1T raw data. All datasets taken get processed automatically with PAX, which produces a *root* file. To analyse these *root* files another package is available: **HAX**, **H**andy **A**nalysis tools for **X**ENON: after a dataset is elaborated by PAX, and the *root* file is created, HAX works in a way that it accesses the desired root file and it creates a so called *MiniTree*,

Variable	Description
NumPMTsHit	Number of Hit seen in the event
PMTs	ID of the PMT where the Hit was detected
Hit_area	Area of signal [pe]
Hit_height	Maximum height of signal [PE/samples]
Hit_left	Left boundary of signal [samples after eventstart]
Hit_right	Right boundary of signal [samples after eventstart]
Hit_width	Peak width [samples]
event.start_time	Start time of the event (Unixtime)
event.stop_time	Stop time of the event (Unixtime)

TABLE 3.1: Variable available for the analysis of a Muon Veto events

which is a selection of variables from the complete *root* file.

The variables used for the analysis of a Muon Veto events are listed in Table 3.1. In Fig. 3.10 an example of the variable *Hit_area* and *Hit_height*: a *Hit* is defined as every signal over the processor (**PAX**) threshold, set to 0.1 pe, in a PMT. An *event* happens when the collection of *Hits* in the PMTs channel satisfies the trigger condition. Each PMT may present many *Hits* inside the same event. So the area of an *Hit* is the number of photoelectrons in that signal, while the area of an event is instead the sum of the areas of the *Hits* contributing to that event.

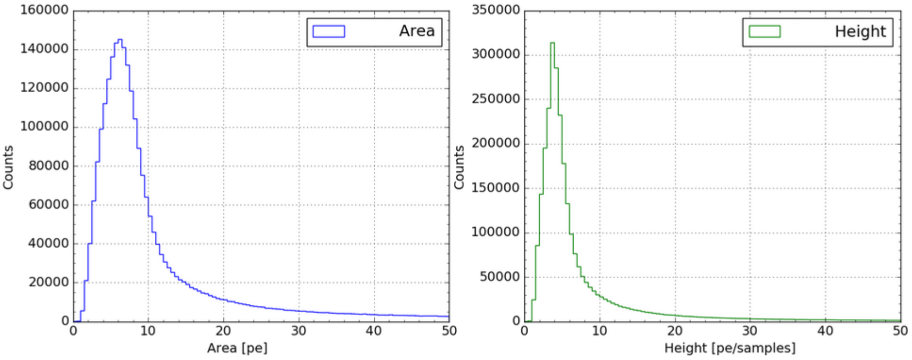

FIGURE 3.10: Distribution of the area and height of events, unit of photoelectrons [PE].

In the processed data the relevant information are related to the area of the signals expressed in unit of photoelectrons. If we want to express the Muon Veto hardware trigger condition, i.e. PMT signal amplitude greater than single photoelectron (s.p.e) mean amplitude, in terms of area of the signal, we get:

$$Q_{Thr} = \langle A_{Thr} \rangle \cdot \frac{V_{pp}}{2^{14}} \cdot \frac{\Delta t}{R} = 5.5 \cdot 10^{-13} C \qquad (3.1)$$

where Q_{Thr} is the signal area, $\langle A_{Thr} \rangle$ is the mean amplitude of single photoelectron, $R = 50\,\Omega$ is the total impedence of the system, $V_{pp} = 0.5$ V is the dynamic range of the ADC whose number of discrete values available is $2^{14} = 16384$ and t is the time width

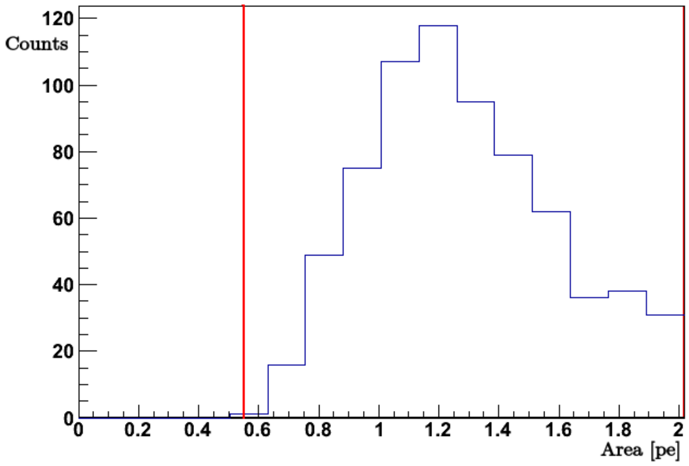

FIGURE 3.11: Distribution of area for events with 8 PMTs in coincidence.

of a sample $t = 10$ ns.

This implies that, due to PMTs gains equalisation ($Q_{s.p.e.} = 1$ pC) the corresponding threshold in the *Hit* in unit of p.e. is:

$$Q^{pe}_{Thr} = 0.55\,pe \tag{3.2}$$

This is visible for example in Fig. 3.11 where the area of the events acquired during Muon Veto data acquisition run is reported. It indeed presents a minimum value of 0.55 pe. We recall that the Muon Veto has been operated using the trigger conditions described in 3.1.3. The relevant infos of the Muon Veto used runs are visible in the run database, as can be seen in the screen shot shown in Fig. 3.12.

3.2 The Monte Carlo simulation

A detailed Monte Carlo simulation of the Muon Veto detector based on **GEANT4** (**GE**ometry and **T**racking) [64] version 4.9.5 was performed. GEANT4 permits to build virtually the detector through volumes. Starting from a mother volume, any other volumes is built inside it, with coordinates referring to it. Every volume contains information regarding its shape, position and composition.

The simulation uses a reconstruction of the experimental Hall B of LNGS. To reproduce the geometry of the Hall B, we built the following volumes:

- Gallery of air, 100 m long, with diameter of ∼18 m and total height of 16 m. (See Fig. 3.14 for the details).

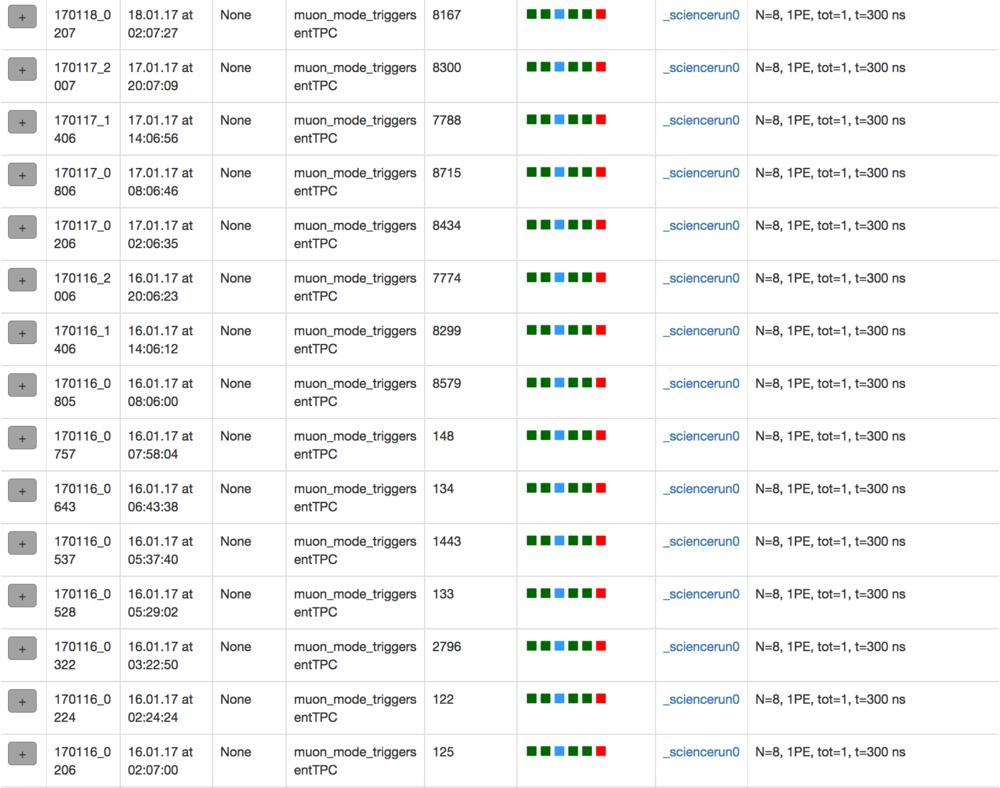

+	170118_0207	18.01.17 at 02:07:27	None	muon_mode_triggersentTPC	8167	🟩🟩🟦🟩🟩🟥	_sciencerun0	N=8, 1PE, tot=1, t=300 ns
+	170117_2007	17.01.17 at 20:07:09	None	muon_mode_triggersentTPC	8300	🟩🟩🟦🟩🟩🟥	_sciencerun0	N=8, 1PE, tot=1, t=300 ns
+	170117_1406	17.01.17 at 14:06:56	None	muon_mode_triggersentTPC	7788	🟩🟩🟦🟩🟩🟥	_sciencerun0	N=8, 1PE, tot=1, t=300 ns
+	170117_0806	17.01.17 at 08:06:46	None	muon_mode_triggersentTPC	8715	🟩🟩🟦🟩🟩🟥	_sciencerun0	N=8, 1PE, tot=1, t=300 ns
+	170117_0206	17.01.17 at 02:06:35	None	muon_mode_triggersentTPC	8434	🟩🟩🟦🟩🟩🟥	_sciencerun0	N=8, 1PE, tot=1, t=300 ns
+	170116_2006	16.01.17 at 20:06:23	None	muon_mode_triggersentTPC	7774	🟩🟩🟦🟩🟩🟥	_sciencerun0	N=8, 1PE, tot=1, t=300 ns
+	170116_1406	16.01.17 at 14:06:12	None	muon_mode_triggersentTPC	8299	🟩🟩🟦🟩🟩🟥	_sciencerun0	N=8, 1PE, tot=1, t=300 ns
+	170116_0805	16.01.17 at 08:06:00	None	muon_mode_triggersentTPC	8579	🟩🟩🟦🟩🟩🟥	_sciencerun0	N=8, 1PE, tot=1, t=300 ns
+	170116_0757	16.01.17 at 07:58:04	None	muon_mode_triggersentTPC	148	🟩🟩🟦🟩🟩🟥	_sciencerun0	N=8, 1PE, tot=1, t=300 ns
+	170116_0643	16.01.17 at 06:43:38	None	muon_mode_triggersentTPC	134	🟩🟩🟦🟩🟩🟥	_sciencerun0	N=8, 1PE, tot=1, t=300 ns
+	170116_0537	16.01.17 at 05:37:40	None	muon_mode_triggersentTPC	1443	🟩🟩🟦🟩🟩🟥	_sciencerun0	N=8, 1PE, tot=1, t=300 ns
+	170116_0528	16.01.17 at 05:29:02	None	muon_mode_triggersentTPC	133	🟩🟩🟦🟩🟩🟥	_sciencerun0	N=8, 1PE, tot=1, t=300 ns
+	170116_0322	16.01.17 at 03:22:50	None	muon_mode_triggersentTPC	2796	🟩🟩🟦🟩🟩🟥	_sciencerun0	N=8, 1PE, tot=1, t=300 ns
+	170116_0224	16.01.17 at 02:24:24	None	muon_mode_triggersentTPC	122	🟩🟩🟦🟩🟩🟥	_sciencerun0	N=8, 1PE, tot=1, t=300 ns
+	170116_0206	16.01.17 at 02:07:00	None	muon_mode_triggersentTPC	125	🟩🟩🟦🟩🟩🟥	_sciencerun0	N=8, 1PE, tot=1, t=300 ns

FIGURE 3.12: Screen shot of the MUon Veto run database. We used a datasample of 70957 events acquired during the first XENON1T science run, between 16^{th} and 18^{th} January 2017.

- Concrete, thickness of 0.50 m, all around the LNGS gallery;
- Rock, thickness 5.00 m, in order to allow the full development of the muon showers.

The Muon Veto Water Tank (containing the XENON1T TPC in its center) is placed inside the gallery mother volume, as shown in Fig. 3.14, in its proper position.

3.2.1 Generation of muons

The flux of muons in the gallery is modulated by the mountain. The profile of the mountain modifies the energies and direction of muons that can reach the detector.
The muon characteristics are taken from a separate Monte Carlo simulation [65] already validated with measurements in situ. In Fig. 3.13 the proper energy and the angular distibutions of muons in the Hall is shown. With these information, it was thus possible to prepare a file containing 10^6 muons. For each of them the charge (muons - antimuons), the energy and the direction are available.
The Muon Veto simulation reads this file and sets the initial conditions of each muon. The position of the muon is then generated uniformly in a cilinder with a radius of 15 m. The axis of the cilinder intersects the origin of the reference system (the top-center

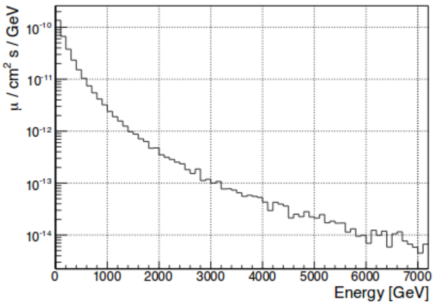

(a) Energy Distribution

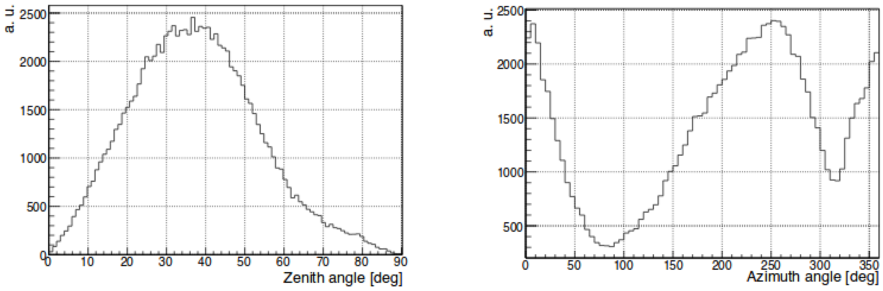

(b) Angular Distribution (Zenith and Azimuth)

FIGURE 3.13: Muon energy distribution at LNGS underground laboratory and angular distribution (Zenith and Azimuth)

of the TPC) and its direction is the same of the muon.
When it enters the experimental hall, the muon can travel through the water tank, and occasionally also through the TPC. We call them **crossing muons**. On the other hand, it may also happen that the muon track is outside the water tank, but the particles produced in the electromagnetic and hadronic shower during its path in rock and concrete can hit the water tank and release energy inside the Muon Veto. We call these events as **showering muons**.

3.2.2 The Monte Carlo output

In Table 3.2, the variables in the Monte Carlo output are listed. The variable *npmthits* contains the total number of photons detected by the photocathode of a PMT in an event; for each hit the time and the PMT ID are stored in the variables *pmthitTime* and *pmthitID*.
Every time a particle crosses a volume, variables of the group **Save** are filled. The *Save_flag* is filled when a particle goes through a volume, namely :

- *Save_flag* == 11 is a particle going from the concrete to the gallery.

Branch Name	Type	Description	notes
eventid	int	event ID	-
pmthits	vector$< int >$	collection of hits per PMT	vector size = number of PMTs
pmthitID	vector$< int >$	collection of the hit PMT ID	vector size = number of hit PMTs
pmthitTime	vector$< int >$	Times of the hit	vector size = number of hit PMTs
xp_pri	float	X position of the primary particle	-
yp_pri	float	Y position of the primary particle	-
zp_pri	float	Z position of the primary particle	-
nsteps	int	number of energy depositing steps	-
xp	vector$< float >$	X position of the step	vector size = nsteps
yp	vector$< float >$	Y position of the step	vector size = nsteps
zp	vector$< float >$	Z position of the step	vector size = nsteps
NSave	int	number of saves	-
Save_flag	vector$< int >$	flag of the save	vector size = NSave
Save_type	vector$< int >$	type of the save	vector size = NSave
Save_x	vector$< float >$	X position of the save	vector size = NSave
Save_y	vector$< float >$	Y position of the save	vector size = NSave
Save_z	vector$< float >$	Z position of the save	vector size = NSave

TABLE 3.2: List of variables contained in the MC output tree

- $Save\_flag$ == 12 is a particle at the border between the gallery and the Water Tank
- $Save\_flag$ == 13 is a particle at the border between the Water Tank and the TPC.

Moreover, GEANT4 provides a class, *G4ParticleDefinition*, to describe particles: by means of a numbering scheme every particle is encoded with a number, according to the PDG classification [66]. So the *Save_type* is filled with a different number according to the particle nature. The muon has a *Save_type* == 13.
Finally the variables $Save\_x$, $Save\_y$ and $Save\_x$ are the coordinates of the saved particles.
In order to select muons in the Water Tank, we require the $Save\_flag$ to be 12 (particle on the WT) and the *Save_type* to be 13 (particle is a muon).
In Fig. 3.14 a scheme of the volumes implemented in the simulation and the track of a muon crossing both the Water Tank and the TPC.

The Monte Carlo simulation output has a set of variable for the analysis different from the output of the real data processing.
In order to analyse both the Monte Carlo data and Muon Veto real data in the same way, I developed a code to convert the Monte Carlo output files into the format of the Muon VetoTreeMaker defined for the real data.
The Monte Carlo simulation provides as output the number of photons's hit on each

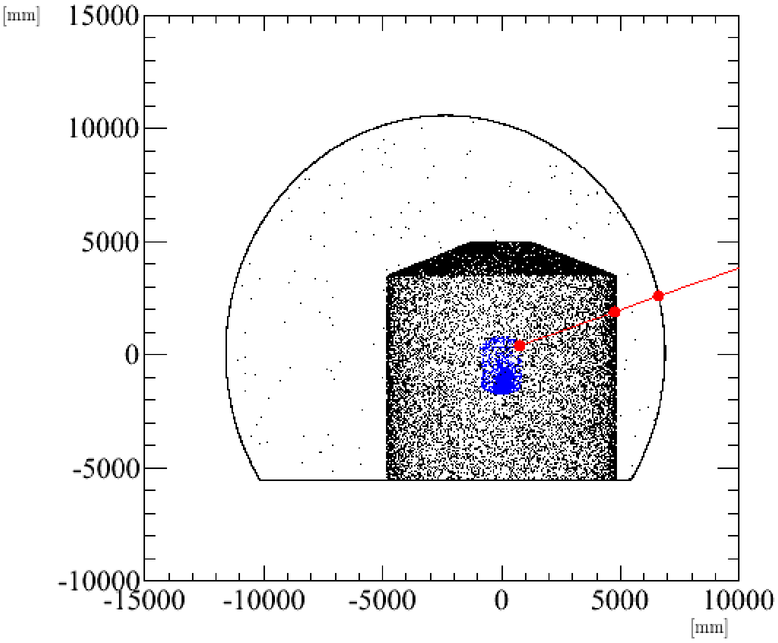

FIGURE 3.14: Example trajectory of a muon (red) and scheme of the volumes implemented in the MC: in blue the TPC, in black the Water Tank.

Parameter	Value	Description
Total QE	0.255	Total QE = QE * CE
Gain	6.2	-
ScaleMc	2	parameter to find the best matching
Processor Th	0.1	Threshold of the software processor

TABLE 3.3: List of the parameters used in the Monte Carlo data processing.

PMT. This number must be corrected by the *Quantum Efficiency*, the *Collection Efficiency*[1] to give the number of photoelectrons produced in each PMTs, which correspond to the variable *Hit_area*.

Starting from this Monte Carlo information I built a clone of the **PAX** processor acting on the Monte Carlo data.

PAX reads and process the signals from all the PMTs everytime the trigger condition is satisfied. The hardware trigger requires two conditions at different levels; The first one is about the single channel: the amplitude of the pulse must be over a certain threshold (*Thr*) for *TOT* number of consecutive samples. The second one is a predefined number of PMTs in coincidence within in a time window of 300 ns.

Once the trigger condition is fulfilled, pulses above the software *processor threshold*, set

---

[1] The Quantum Efficiency is the ratio of output electrons to incident photon. It is corrected by the *Collection Efficiency* which is the ratio of the number of electrons landing on the effective area of the first dynode of the PMT to the number of emitted photoelectrons.

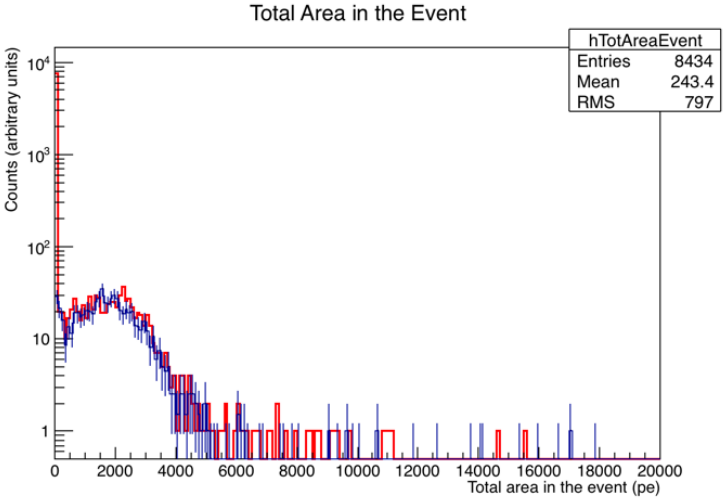

FIGURE 3.15: Distribution of area of the event for Monte Carlo data (Blue) and Muon Veto data (red). With the correction of a factor two we see the compatibility between Monte Carlo and real data.

to 0.1 pe are stored in the output *root* file. In order to have the same output I implemented this feature of the experimental data processor in the Monte Carlo output files. Lastly, to be similar to the real data we down sampled the Monte Carlo Data from the infinite precision of the GEANT4 output to the 10 ns bin width of the digitizer: the arrival times of the photons on the PMTs, have been projected in 10 ns bins. In this way the Monte Carlo output a *root* file has the same format of the Muon Veto processed data, with all the variables listed in Table 3.1.

As first test of our Monte Carlo simulation of the detector we compared the distribution of the total area of the event (the sum of all the *Hit_area*) from Monte Carlo and experimental data. The comparison shows that the amount of light seen in real data for a muon crossing the Water Tank is a factor two larger than what expected from the simulation. The discrepancy can be due to the fact that we didn't take in consideration the reflectivity of the cryostat in the simulation or that the absorption length in water is higher than what implemented in the Monte Carlo simulation.
Fig. 3.15 shows the distribution of events obtained from the Monte Carlo simulations and corrected by a factor 2 together with the distributions of the area of the events of the experimental data. With this correction, Monte Carlo results and experimental data are in good agreement, so we can safely use our Monte Carlo simulation to compute the Muon Veto tagging efficiency for crossing and showering muons.

3.3 Monte Carlo and experimental data

Before studying the Muon Veto tagging efficiency we compared the Monte Carlo and experimental data in terms of rate, differential multiplicity and area of the events.

The trigger rate of the Muon Veto can be calculated as follow:

$$R = \frac{n_{mu}}{time} \tag{3.3}$$

where n_{mu} is the number of events satisfying the trigger condition and *time* is the run duration. The simulation used in this work corresponds to about 1200 hours of Muon Veto data acquisition. The experimental data covers a time period of about 54 hours. For the Monte Carlo simulation, we extracted the equivalent time as: $T = \frac{N}{A\phi}$, where N is the number of muons generated, ϕ is the muons flux, corresponding to $R = 0.331 \cdot 10^{-7}/\mathrm{cm}^2/\mathrm{s}$ and A is the effective area of the disk where muons have been generated, $7.07 \cdot 10^6$ cm^2.

In section 3.1.3 it is explained how the trigger threshold is set, we recall its correct definition: the *trigger threshold* is the average height of pulses corresponding to the emission of a single photoelectron at photocathode.
In this analysis we define the *software threshold* (ThS), the request for each pulse to have an area equal or bigger than a particular threshold value.

The multiplicity is the number of PMTs in coincidence in a time window of 300 ns, each one with an area greater than a chosen ThS.
In Fig. 3.16 we show the rate of the Muon Veto experimental data as a function of the trigger threshold and the number of PMTs in coincidence. Fig. 3.16 represents the *Integral Multiplicity*, namely the number of events with a multiplicity value equal or larger than a minimum number of PMTs in coincidence (x-axis).
The rate with a software threshold of 1 pe is an order of magnitude greater than what obtained using other thresholds. This is probably due to the effect of natural radioactivity (γ from the rock in Hall B that produce electrons by Compton scatter in water), which triggers PMTs when a low threshold is set.
A zoom of Fig. 3.16 and the Monte Carlo results are shown in Fig. 3.17(a) and 3.17(b).
In the Monte Carlo, the contribution of the ambient radioactivity is not simulated. There are two possibilities, in terms of trigger conditions, to avoid the acquisition of events from natural radioactivity: If we want to maintain the software trigger threshold to 1 pe, we might request a minimum multiplicity greater than 20, otherwise we must set an higher trigger threshold.
With a trigger threshold of 1 pe and a multiplicity bigger than 20, we obtain an event

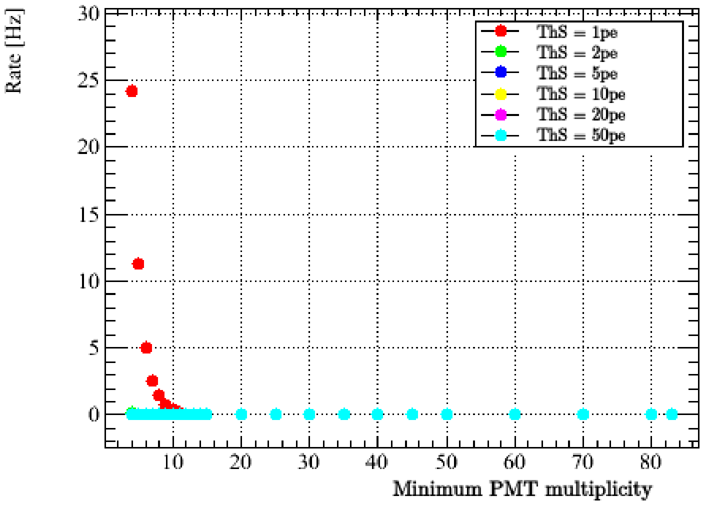

FIGURE 3.16: Trigger rate as a function of multiplicity and threshold

rate of R =∼ 0.03 Hz, which is close to the rate of muon expected in the Water Tank, extracted from the Monte Carlo simulation (∼ 0.037 Hz). From the comparison between the Monte Carlo and the experimental data, we see that the trend of the rate is similar: both show a decrease as the multiplicity and software threshold increase.

Events in the plateau region are expected to be muons, their rate range is from $R = 0.03$ Hz for a software threshold between 2 pe and 5 pe and a multiplicity lower than 35 PMTs, to R = 0.025 Hz for a multiplicity between 35 and 60 PMTs.

In Fig. 3.18 is shown a comparison between the rate of Muon Veto data and Monte Carlo data for selected values of the software threshold. It is evident the absence of natural radioactivity for Monte Carlo data (Fig. 3.18(a)) and the fact that, in the Muon Veto data, this effect decreases as soon as the software threshold increases, giving a better agreement with Monte Carlo data. (Fig. 3.18(b) and 3.18(c)). The agreement in the rate is very good for multiplicities lower than 30 PMTs, from 30 to 84 PMTs the experimental data present a slightly higher rate. In Fig. 3.19 we show the differential multiplicity for various software thresolds. The runs used for the analysis are taken with a trigger condition set to 8 PMTs and a trigger threshold of 1 pe. In Fig. 3.20 we show the multiplicities obtained with software thresholds of 1 pe and 0.1 pe. With a software threshold of 1 pe in amplitude, we see some events with a multiplicity lower than 8. They fulfilled the trigger condition, in our case the coincidence of at least 8 PMTs whose heights are larger than the trigger threshold,, i.e. the average height of the signals with 1 pe area. Because of the fluctuations in the ratio between the signal area and height, in some of the PMTs, the hit might have an area lower than the software condition (set to 1 pe) and not contribute to the calculation of the multiplicity.

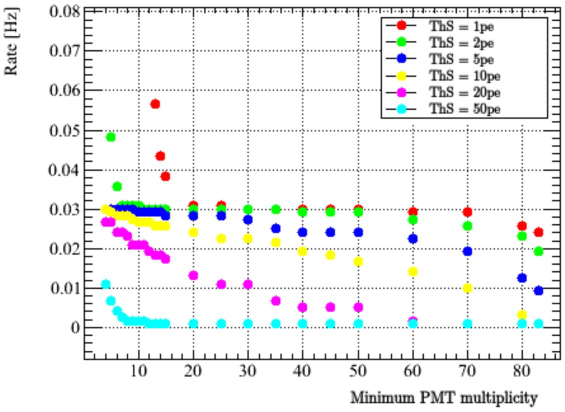

(a) Muon Veto data

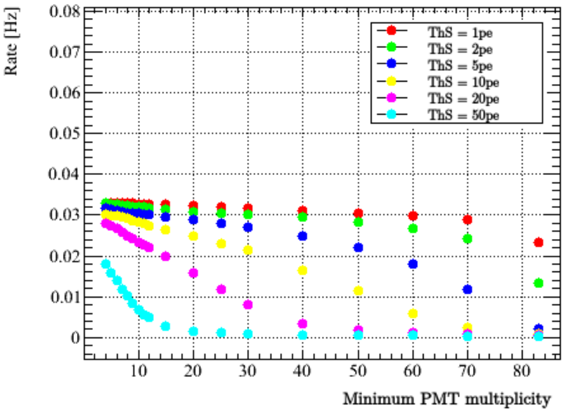

(b) Monte Carlo data

FIGURE 3.17: Rate comparison for Muon Veto data and Monte Carlo data.

With a software threshold of 0.1 pe, the software multiplicity reflects the trigger multiplicity.

In Fig. 3.21 we shows the correlation between the area of an event and its multiplicity. It is almost linear, indeed the more PMTs participate to the event the more photoelectrons are collected.

Many events have the maximum value of multiplicity, N = 84. We might interpret these events as the muons that fully crossed the Water Tank producing a huge amount of Čherenkov light. We see the effect of natural radioactivity in the Muon Veto data, with a low threshold (Fig. 3.21(a)) there are a many events with a value of multiplicity up to 20 and an area of less than 10^2 pe.

We see that these events are not present in the Monte Carlo simulation (Fig. 3.21(b)) and as software threshold increases, they disappear (Fig. 3.21(c) and 3.21(e)).

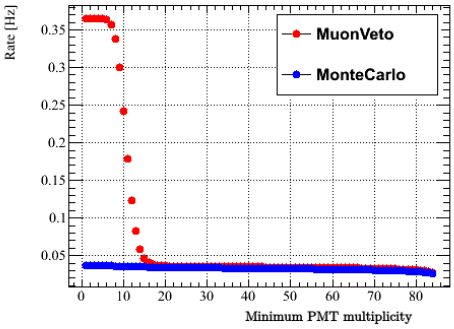

(a) ThS = 1 pe

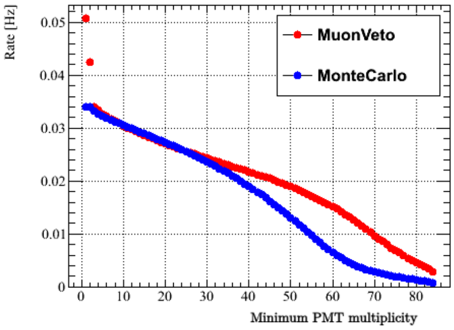

(b) ThS = 10 pe

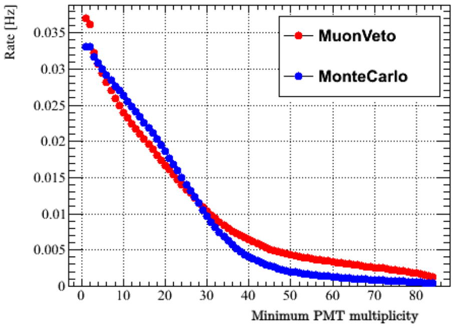

(c) ThS = 20 pe

FIGURE 3.18: Differential multiplicity for Muon Veto data and Monte Carlo data for a software threshold of 1 pe (a), 10 pe (b) and 20 pe (c).

The Monte Carlo simulation allows to select muons by their trajectory and analyze their different behaviors. We divided muons into three categories, mutually exclusive:

- Muons in the water tank, but not in the TPC.
- Muons that cross the water tank and the TPC.
- Muons outside the Water Tank, but with some particles in it. We don't see the muon directly, but we see the effect of the shower produced by it.

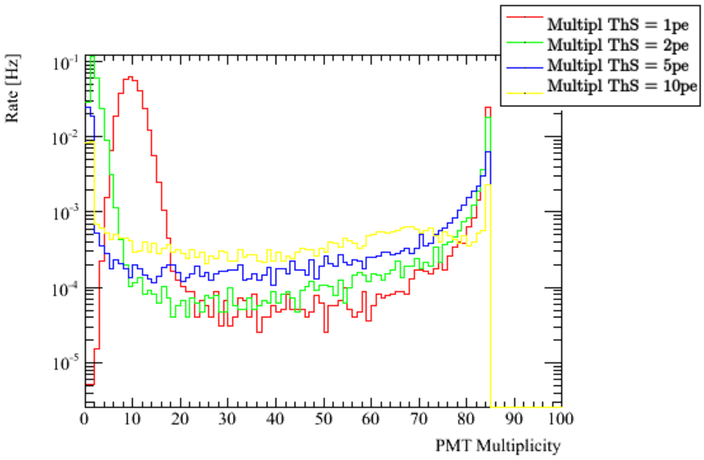

(a) Muon Veto data

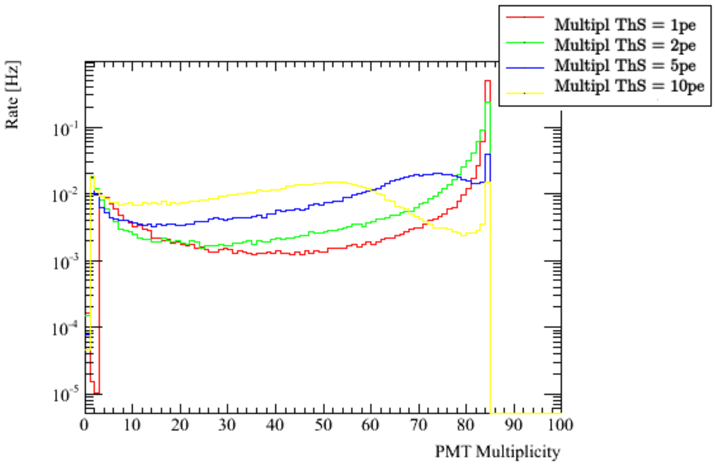

(b) Monte Carlo data

FIGURE 3.19: Differential multiplicity for Muon Veto data and Monte Carlo data.

In Fig. 3.22 we show the total area of events of Muon Veto data and the three categories in which Monte Carlo events have been divided. The software threshold is set to 1 pe. We see that muons crossing the TPC are few compared to the other categories. Their rate is R = $\sim 3.4 \cdot 10^{-4}$ Hz, two orders of magnitude lower than the rate of events crossing the Water Tank, which have a rate of R = $\sim 3.3 \cdot 10^{-2}$ Hz . Lastly, events with a muon outside the Water Tank, but with secondary particles on it, have a rate of R = $\sim 3.5 \cdot 10^{-3}$ Hz.

The black crosses are Muon Veto data with theis statistical errors; the agreement between data and Monte Carlo (blue line) is very good. Moreover at very low values of area, we see the effect of natural radioactivity. This explains the high number of Muon Veto data in the first few bins.

After a minimum value at about 400 pe, the Muon Veto event's area presents a bump around $\sim$ 2000 pe, this is the average value of photoelectrons produced by muons.

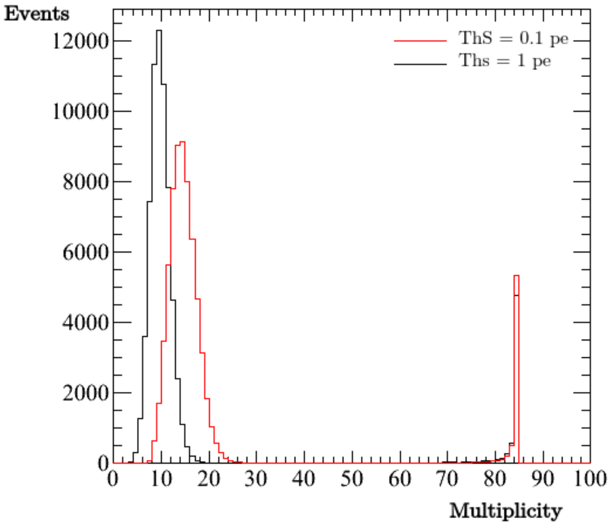

FIGURE 3.20: Differential multiplicity for a software threshold of 1 pe and 0.1 pe.

In the same figure the contribution of muons outside of the Water Tank is shown with the green line. The muon doesn't cross the Water Tank but some of the particles generated in electromagnetic or hadronic showers may enter the Water Tank. The number of these events decreases as a function of the signal area: the secondaries particles indeed are not as penetrating as the muon and we don't expect them to have an area bigger than 2000 pe. The purple line represents muons crossing also the TPC, which are less abundant than the other categories but they have a long path in water and so a large amount of emitted light. The events with more than 6000 detected *pe* are due to muons that have generated a cascade inside the Water Tank.

We report also in Fig. 3.23 the differential multiplicity for the Muon Veto data and the Monte Carlo simulation for different software thresholds.

The three categories of muons show different behaviours: the secondaries from muons out of the Water Tank are not very energetic, but with a software threshold of 1 pe and with a low multiplicity (Fig. 3.23(a)) they are the main contribution. The rate of these events decreases as the trigger threshold and the multiplicity increase. For a trigger threshold of 20 pe, their contribution is evident only at low multiplicity and close to the maximum number of PMTs (84).
Muons in the TPC, which are enough energetic to pass through the water layer, present the opposite rate. Because of their large path in water at low threshold, they trigger almost all PMTs, in fact we see these events with the maximum multiplicity. With the request of an higher threshold (20 pe), we cut events with low area, and their multiplicity

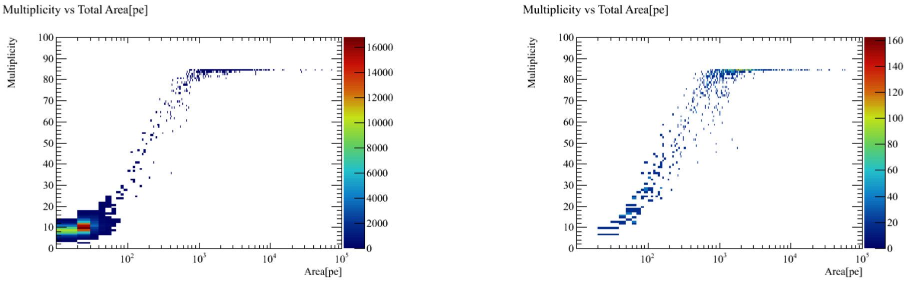

(a) Muon Veto data: ThS = 1pe (b) Monte Carlo data: ThS = 1pe

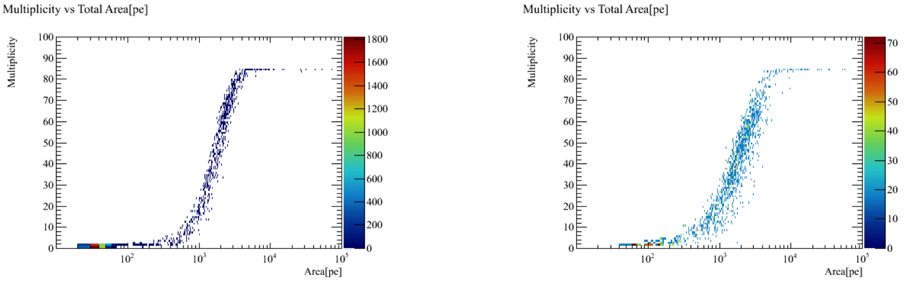

(c) Muon Veto data: ThS = 10 pe (d) Monte Carlo data: ThS = 10 pe

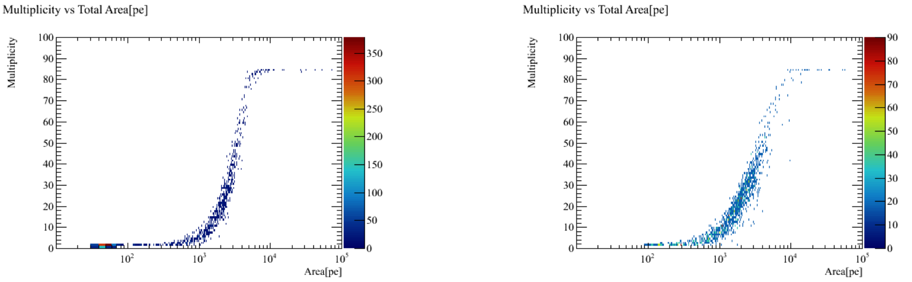

(e) Muon Veto data: ThS = 20 pe (f) Monte Carlo data: ThS = 20 pe

Figure 3.21: Area versus Multiplicity for Muon Veto data and Monte Carlo data.

decreases, presenting a bump at about 15 PMTs.

The muons in the Water Tank present, for a low threshold, a flat value of the rate as a function of the multiplicity. Muons crossing the Water Tank are coming with different angles and have different incident impact points. Their trajectory inside the Water Tank can be either very long or very short. A long trajectory allows the triggering of all PMTs whereas muons crossing the Water Tank only close to the ”corner” and thus with a short trajectory, trigger a few number of PMTs.

The Monte Carlo simulation clearly shows that the major contribution to the muon events is represented by muons in the Water Tank, their rate is very close to the total rate of muons. There is only one conditions in which the rate of these events differs substantially from the total rate: low multiplicity and low threshold, in this trigger condition there are many events from secondaries generated by muons outside of the Water Tank.

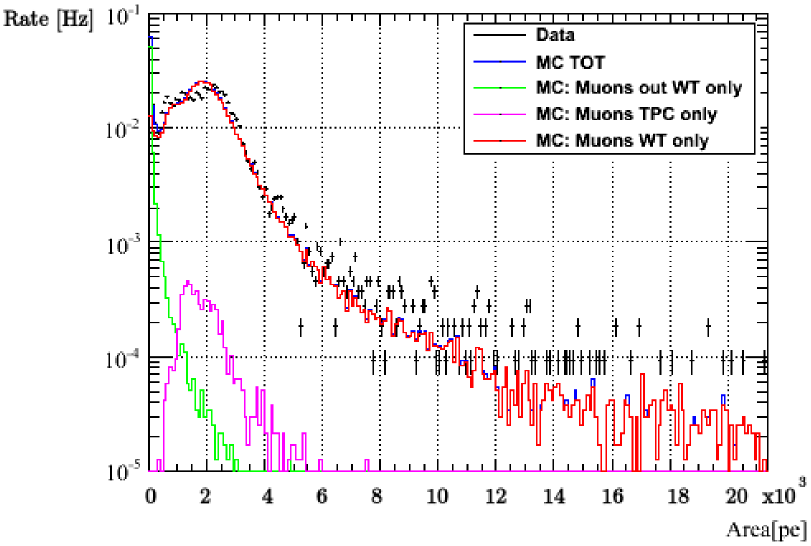

FIGURE 3.22: Total area of events of the Muon Veto data and of the three categories in which Monte Carlo events have been divided. The black points are experimental data with their statistical error, the blue line is the total output of the Monte Carlo. It is divided into muons in the Water Tank but not in the TPC (red line), muons out of the Water Tank (green line) and muons in the TPC (purple line).

3.4 Muon Veto Tagging Efficiency

After the first months of commissioning and testing, XENON1T is now in data acquisition for its first science run, called *Science Run 0*. In order to perform any background estimation, it is fundamental to know the tagging efficiency of the Muon Veto detector for both muon and shower events. The Muon Veto constitute an effective shield against gammas and neutrons produced by rock radioactivity. The only residual enviromentals background after the water shield is given by muon-induced neutrons, which are produced via direct muon spallation of nuclei or through electromagnetic and hadronic cascades generated by muons [59].

We consider dangerous events those with at least one neutron at the surface of the Water Tank, with a neutron energy of at least 10 MeV. In [59] it was estimated the residual background due to neutrons crossing the whole water shield, producing a single scatter nuclear recoil, in 1 tonne fiducial volume, in the $[5, 50]$ keV energy range. Before considering the impact of the Muon Veto, the background is summarised in Table 3.4.

	Muon events	Shower events
Background rate [ev/y] in 1 tonne	$9 \cdot 10^{-3}$	$2.1 \cdot 10^{-2}$

TABLE 3.4: Background rate in 1 tonne fiducial volume for muon and showering events without considering the Muon Veto tagging.

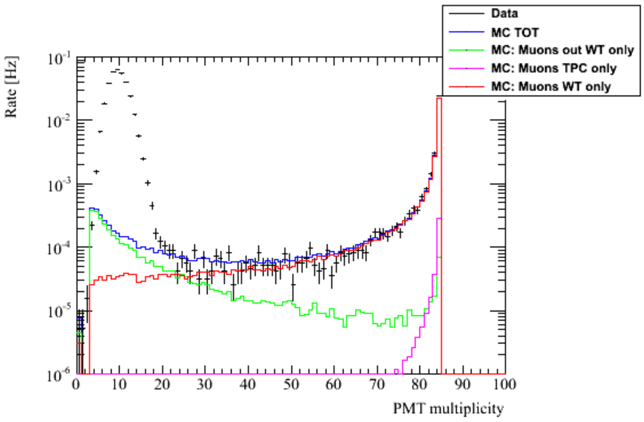

(a) ThS = 1pe

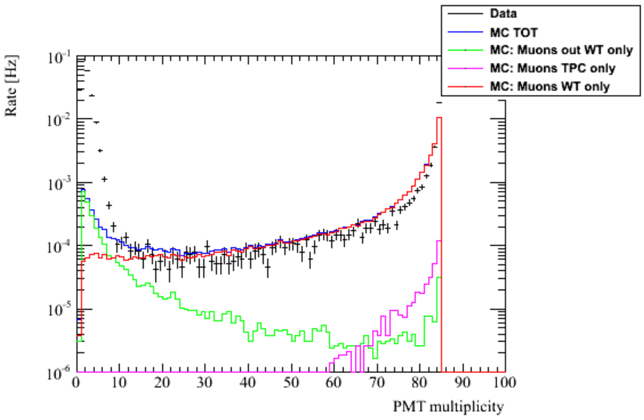

(b) Muon Veto data: ThS = 2 pe

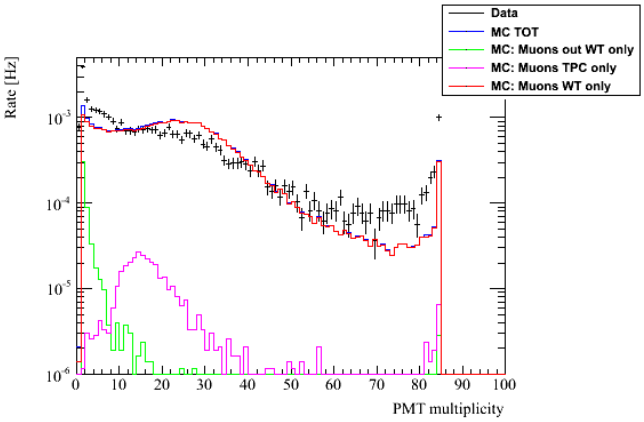

(c) Monte Carlo data: ThS = 20 pe

FIGURE 3.23: Differential multiplicity for Muon Veto data and Monte Carlo data. The black crosses are experimental data with their statistical error, the blue line is the total output of the Monte Carlo. It is divided into muons in the Water Tank but not in the TPC (red line), muons out of the Water Tank (green line) and muons in the TPC (purple line).

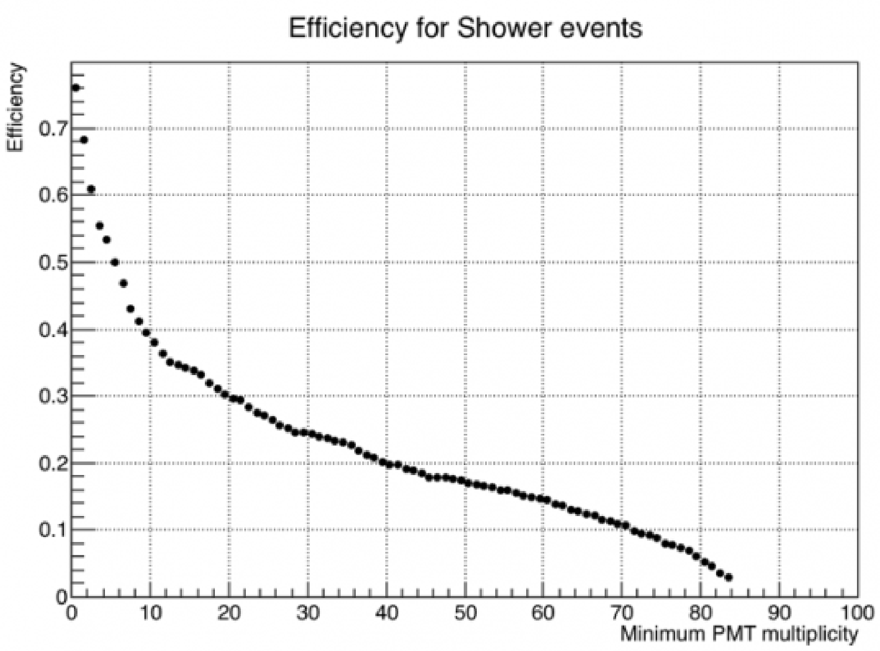

FIGURE 3.24: Tagging efficiency for shower events as a function of the PMT multiplicity. The threshold in each PMT is fixed to 1 pe.

After the validation of the Monte Carlo simulation against the available Muon Veto data, we can reliably use the Monte Carlo to estimate the tagging efficiency. We applied then to the dangerous events the trigger requirements of the Muon Veto during the *Science Run 0*.

The Muon Veto tagging efficiency is $\eta_\mu = 99.5\%$ for muon events and $\eta_{shower} = 43\%$ for the shower events.
The efficiency for the shower events, as a function of the PMT multiplicity is shown in Fig. 3.24. With the detection efficiency estimated above, we calculate the residual background from muon induced neutrons and report the values in Table 3.5

Background rate [ev/y] in 1 tonne	Muon events	Shower events	Total
Before MV cut	$9 \cdot 10^{-3}$	$2.1 \cdot 10^{-2}$	$3.0 \cdot 10^{-2}$
Tagging Efficiency	99.5%	43%	
Residual Background Rate	$5 \cdot 10^{-5}$	$1.2 \cdot 10^{-2}$	$1.2 \cdot 10^{-2}$

TABLE 3.5: Residual background rate in 1 tonne fiducial volume.

In the 40 days exposure of *Science Run 0*, the resulting background is $1.3 \cdot 10^{-3}$ events in 1 t fiducial volume, practically negligible.

3.5 Conclusion

The comparison between the Monte Carlo simulation of the Muon Veto detector and the experimental data show an very good agreement. This is evident for example either from Fig. 3.22 where we show the total light detected in the event, and in Fig. 3.19 where we plot the differential PMT multiplicity. The agreement between the simulation and the experimental data allows us to safely use the simulation to study and compute the Muon Veto tagging efficiency. With the trigger requirements used by the Muon Veto during the XENON1T *Science Run 0* we obtain a tagging efficiency of $\eta_{\mu} = 99.5\%$ for crossing muon events and $\eta_{shower} = 43\%$ for showering muons events.
Given these efficiencies, it is possible to calculate the expected background in the *ScienceRun0*, which corresponds to $1.3 \cdot 10^{-3}$ events in 1 tonne fiducial volume.

Chapter 4

SiPM Silicon PhotoMultiplier

In this chapter the physical and electronic working principles of a silicon photomultiplier (SiPM)are described. The SiPM addresses the challenge of detecting, timing and quantifying low-light signals down to the single-photon level. It offers a highly attractive alternative to PMTs offering all the benefits of a solid-state device: low voltage operation, insensitivity to magnetic fields, mechanical robustness and excellent uniformity of response.
In the framework of the XENON collaboration, we started a study of the possible use of a SiPM as an alternative to the current technique for the light collection, which consists of two arrays of PMTs based at the top and bottom of the TPC, characterised by a low radioactivity and by a high quantum efficiency.
In the first part of this chapter we briefly describe the development of the SiPM, in the second one, the performance parameters and noise components are reported. In the next chapter we will study the **LCE** (**L**ight **C**ollection **E**fficiency) for different future possible configuration for a TPC instrumented with SiPMs.

4.1 The physics of a silicon photodiode

4.1.1 Silicon

Silicon (Si) has been used as a particle detector both for ionizing particles (excellent spatial resolution) and for photon-counting (at single-photon level) devices. It is an indirect semiconductor and the electrical properties are related to its energy band structure.
Indeed the valence band is filled and the conduction band is only partly filled, depending on the room temperature.
If impurities are added to a semiconductor (*doping*), the material characteristics change.

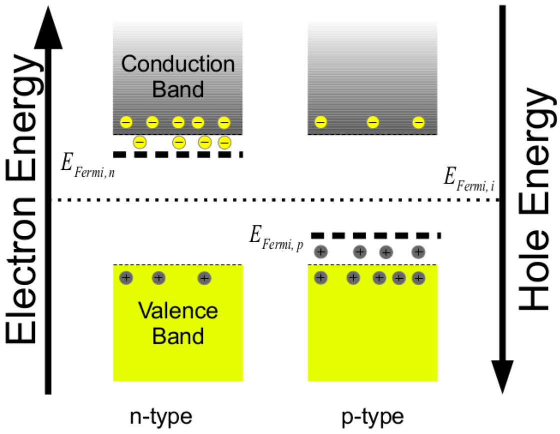

FIGURE 4.1: The band structure of p and n-type silicon. At absolute zero temperature the valence band is completely occupied and the maximum energy of the highest occupied state is called E_v. The conduction band is instead completely empty. The energy of the lowest unoccupied state is called E_c. The bandgap is the forbidden area in between. There are no allowed energy states available and the width of the bandgap is $E_g = E_c - E_v$. In n-type silicon electrons form the majority charge carriers while holes are minority charge carriers, whilst in p-type material this is vice versa.

There are two ways of doping; considering that silicon forms four covalent bonds, one can add donors, atoms of valence five like phosphorus, **P**, or arsenic, **As**, which leave free excess electrons in the conduction band, or acceptors, of valence three, like boron, **B**, or aluminium, **Al**, which leave positive holes in the valence band.

Donors (n-type silicon) and acceptors (p-type silicon) introduce states in the forbidden region (bandgap) and an increase in doping concentration affords an increase in conductivity (see Fig. 4.1). The Fermi level, namely the energy at which the probability of occupation by an electron is exactly one half, shifts towards the conduction band for n-type silicon and towards the valence band for p-type silicon. The extra electrons for n-type material reside in a discrete energy level inside the gap and can be excited into the conduction band. For p-type material the extra states are created in the forbidden region near the valence band, which means that electrons from the valence band are excited to this extra level. In this case an electron-hole pair is created and the holes become majority charge carriers for this kind of material.

4.1.2 The p-n junction

A boundary between two types of semiconductor material, p-type and n-type, inside a single crystal of semiconductor is called *p-n junction*. The **p** (positive) side contains an excess of electron holes, while the **n** (negative) side contains an excess of electrons. A p-doped and an n-doped semiconductor is relatively conductive, but the junction between them can become depleted of charge carriers, and hence non-conductive. This property

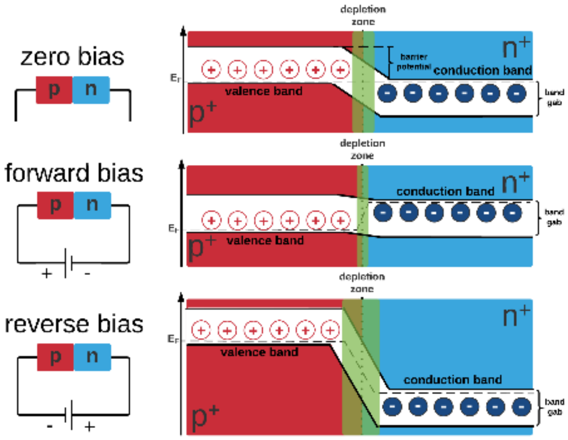

FIGURE 4.2: Band-gap diagram for zero bias (top), forward bias (middle) and reverse bias(bottom) of a silicon p-n junction. The depletion zone decreases for forward bias making the junction conductive and increases for reverse bias making the junction non conductive.

depends on the relative voltages of the two semiconductor regions. The application of a voltage across a p-n junction is called *bias*. The simplest electronic component containing a p-n junction is a diode, allowing current to flow only in one direction, depending on the bias:

- **Zero bias:** for a p-n junction at zero bias (see Fig. 4.2), the Fermi levels E_F, match on the two sides of the junctions. Electrons and holes reach an equilibrium at the junction and form a depletion region. The upward direction in Fig. 4.2 represents increasing electron energy. That implies that you would have to supply energy to get an electron to go up or to get a hole to go down in the diagram.
- **Forward bias:** To forward-bias the p-n junction, the p side is made more positive, so that it is 'downhill' for electron motion across the junction. The depletion region becomes smaller and an electron can move across the junction and fill a vacancy or 'hole' near the junction. It can then move from vacancy to vacancy leftward (see Fig. 4.2) toward the positive terminal, which could be described as the hole moving right. The conduction direction for electrons in Fig. 4.2 is right to left.
- **Reverse bias:** To reverse-bias the p-n junction, the p side is made more negative, making it 'uphill' for electrons moving across the junction. The depletion zone becomes bigger, making the p-n junction non-conductive (see figure4.2).

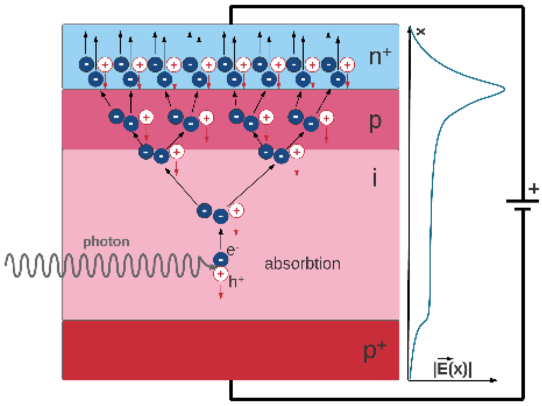

FIGURE 4.3: Different doped layers of a reverse biased APD showing the corresponding electric field strength. The photon absorption, impact ionisation and avalanche formation are visualized. The electron trajectories are represented by black arrows and the hole trajectories by red arrows.

4.1.3 Avalanche photodiode (APD)

An avalanche photodiode is a diode with four different layer of semiconductor doped asimmetrically:

- p^+ **zone**: zone intensely doped with number of acceptors N_a.
- **intrinsic zone**: non doped zone.
- **p zone**: zone mildly doped with N_a acceptors.
- n^+ **zone**: zone intensely doped with N_d donors

An electron-hole pair is generated for example by the absorption of a photon with sufficient energy in the intrinsic region i (see Fig. 4.3) or by thermal effect. Under the influence of an external field, the electron drifts to the n^+ side and the hole drifts to the p^+ side, resulting in the flow of a current.

The charge carriers can gain sufficient energy in the high field at the $p - n^+$ junction to generate other electron-hole pair, losing some of their kinetic energy in the process. This process is known as *impact ionization*. The charge carriers can accelerate again, as the secondary electron or hole, and create more electron-hole pairs. After a few transit times, a competition develops between the rate at which electron-hole pairs are being generated by impact ionization and the rate at which they exit the high-field region and are collected. If the magnitude of the reverse-bias voltage is below a value known as the *breakdown voltage*, the collection dominates, causing the population of electrons and holes to decline.

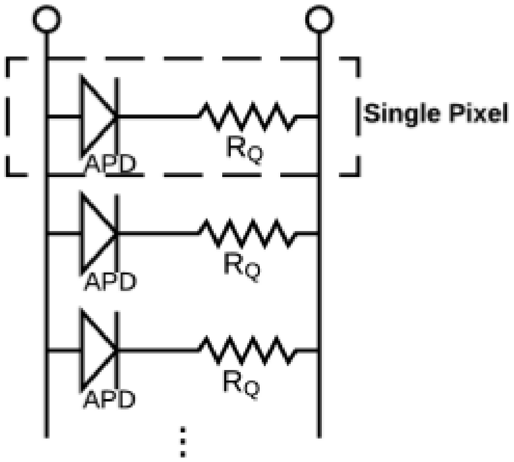

FIGURE 4.4: Equivalent circuit of a SiPM. A single pixel is a series combination of an avalanche photodiode (APD) and a quenching resistor (R_q). All the pixels are connected in parallel.

4.1.4 Operation of APDs and SiPMs

Silicon photomultipliers (SiPMs) consists of several pixels connected in parallel; one pixel is a combination of an APD and a quenching resistor R_q connected in series, as illustrated in Fig. 4.4. It is operated with an external reverse-biased voltage (V_{bias}), that is up to a few volts larger than the breakdown voltage (V_{br}) of the APD. In this mode the electrons and holes multiply by impact ionisation faster than they can be extracted. The overvoltage, $\Delta V = V_{bias} - V_{br}$, is one of the most important adjustable parameters affecting the performance of the device. The following two subsections describe in detail, the operation of an APD and a SiPM for $V_{bias} > V_{br}$.

Avalanche photodiode in Geiger mode When the applied bias voltage V_{bias} to an APD exceeds its breakdown voltage V_{br}, the APD is said to be in Geiger mode [67]. It is also called Single Photon Avalanche Diode (SPAD), it is able to detect also signal at low intensity (up to the single photon) and to provide the arrival time of the photon with excellent time resolution. Geiger-mode APDs are modelled by the circuit shown in Fig. 4.5, where the main components are the capacitance C_J of the depletion region of the APD, a switch S, a voltage and a series resistance R_s that is equal to the combined resistance of the undepleted regions in the APD. The value of R_s depends on the voltage over the diode since the latter controls the total length of the undepleted regions. R_s is of the order of several hundred ohms at zero bias and decreases to tens of ohms for bias around V_{br}.

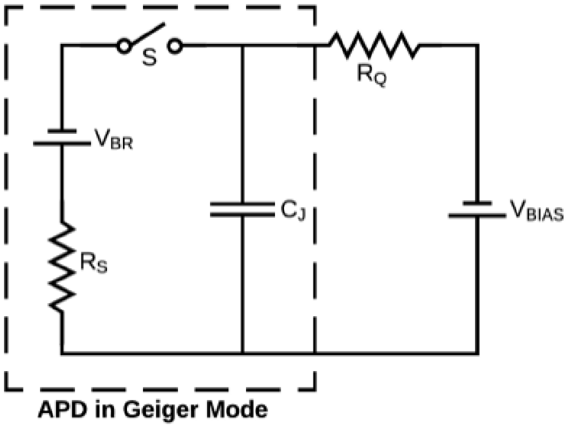

FIGURE 4.5: Equivalent circuit of an APD in Geiger mode in series with a resistor R_q.

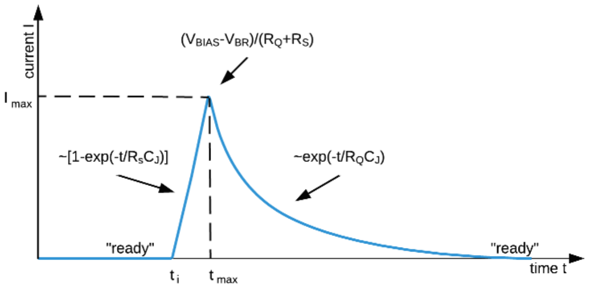

FIGURE 4.6: Current flowing through the terminals of the APD as a function of time. The pulse is asymmetric around $t = t_{max}$ because of $R_q \gg R_s$.

In the absence of light, the switch S is open and C_J is charged to V_{br}. The voltage on the APD is $\Delta V = V_{bias} - V_{br}$ above V_{br}, and the APD is ready to detect a photon. If the APD absorbs a photon and the resulting charge carrier triggers an avalanche. The switch S closes and C_J begins to discharge through R_s, which tends to lower the voltage across the APD. However, since the APD is biased by a constant voltage source V_{bias} , a current begins to flow through the terminals of the APD reaching a steady state value of $\Delta V/R_S$. This current will persist unless V_{bias} is reduced to V_{br} , restoring the APD to the light-sensitive state. The role of R_q is to extinguish or quench the avalanche bringing the APD back to Geiger mode, hence the name quenching resistor. The time dependency of the described current flow through the APD is shown in Fig. 4.6.

The avalanche begins at $t = t_i$. The leading edge of the current pulse increases with the time constant $R_s \times C_j$ and reaches a maximum value of

$$I_{max} = \frac{V_{bias} - V_{br}}{R_q + R_s} \approx \frac{\Delta V}{R_q} \tag{4.1}$$

at t_{max} . At this time the avalanche stops or is quenched because of R_q . After t_{max}, C_j recharges to the nominal voltage of V_{bias} while the current decreases with a time

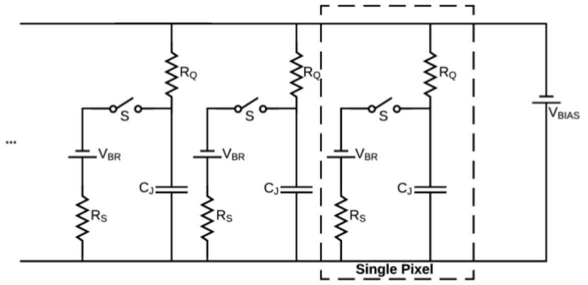

FIGURE 4.7: Equivalent circuit of a SiPM. Every pixel correspond to an APD with a quenching resistor R_q in series. All the pixels are connected in parallel and operated in Geiger mode.

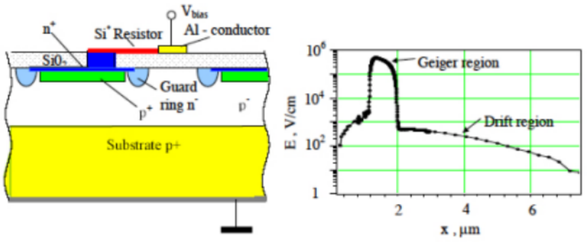

FIGURE 4.8: Transverse section of a SiPM and its trend of electrical field.

constant $R_s \times C_j$. Because $Rq \gg R_s$, the leading edge of the pulse is steeper than the declining edge, making the pulse asymmetric around $t = t_{max}$.

SiPM A SiPM is an array of light-sensitive elements, *pixels*, that are all connected in parallel and externally biased by a single voltage source, V_{bias}. Each pixel is a series combination of an APD and a quenching resistor R_q. By design, all pixels are identical and all operated in Geiger mode. Since the pixels are connected in parallel and work on a common load; It is not possible to have any information about which pixel has detected for example a photon.Fig. 4.7 shows the equivalent circuit of a SiPM; the dashed rectangle delineates a single pixel. In the absence of light, all the switches are OFF, and the voltage is V_{bias} on each APD and is zero on each R_q. If a single APD absorbs a photon and the process triggers an avalanche, the switch goes to the ON position, and the current pulse begins to flow through the terminals of the SiPM. The resistor R_q of that pixel quenches the avalanche, and the pixel is restored back to the 'ready' state. If two (or more) photons simultaneously trigger avalanches in two (or more) distinct pixels, the current pulse flowing through the terminals of the SiPM is a superposition of the current pulses. Instead, if a single pixel absorbs simultaneously two or more photons, the resulting current pulse is identical to the one produced by a single photon.

In figura 4.8 is showed an illustrative scheme of the a SiPM structure.

The *drift* region, at low electric field, few mm thick, is on the low-resistive substrate p. The condition for the discharge are verified in the Depletion Layer, between the p^+ and n^+ layers, where it is located a high electric field ($\approx 3 - 5 \cdot 10^5$ V/cm).
The uniformity of the electric field is garanted by a guard-ring around every pixel and the electrical decouplig is obtained by resistive stripes of polysilicon; all the cell are connected by Aluminium stripes in order to read the total signal of the detector. The upper part is coated by a antireflecting cladding to minimize the photon reflection on the surface. Lastly, a $Si0_2$ or SiC layer cover the device in order to protect it. The last prototypes of SiPM have also an optical trench, made of a nitrade layer to reduce the . cross-talk (section 4.6.2).

4.2 Gain of a SiPM

The *Gain* of a SiPM is defined as the amount of charge created for each detected photon. Values of gains are around $\sim 10^5 - 10^7$. Considering one single pixel, the gain is defined as the ratio of the total charge crossing the junction when a photon is revealed and the electron charge $q = 1.6 \cdot 10^{-19}$ C :

$$G_{pixel} = \frac{Q_{pixel}}{q} = C_{pixel} \frac{V_{bias} - V_{br}}{q} \tag{4.2}$$

So it is evident that the gain depends on the breakdown voltage and on the costructive characteristic of the device.In order to have an accurate knowledge of the signal in output, the uniformity of the pixels gain is necessary.
The external parameter modifiable to have a bigger uniformity are V_{bias} and the pixel dimensions. Considering a signal of time duration t, we calculate the value of the total output charge of the SiPM as:

$$Q_{tot} = \int_0^t \frac{V_{out}}{R_{load}} dt \tag{4.3}$$

where V_{out} is the voltage on R_{load}. If the charge is uniform, from the total charge emitted from a single pixel, we can extract the number of pixels on.

4.3 The Photon Detection Efficiency (PDE)

The Photon Detection Efficiency (PDE) is the probability than an incoming photon with certain wavelength is detected. PDE is the product of different factors:

$$PDE = Q.E. \cdot \eta_{trigger}(\lambda, V_{bias}, T)\eta_{geom} \tag{4.4}$$

where η_{geom} is the geometrical efficiency, namely the ratio of active surface to total detector area. Tipically this values is around $\sim 0.3 - 0.6$. $\eta_{trigger}$ is the efficiency to trigger a microcell when an electron hole pair has been created, it depends on the V_{bias} and on the wavelength of the photon. QE is the quantum efficiency to create a primary electron hole pair, it is defined as the average number of electron-hole couples created by the incident photon conversion in the depletion layer.

With the last prototypes of SiPM, the typical values of detection efficiency are from 10% to 20%.

4.4 Timing Resolution

The time response of a SiPM depends on four differen process that happens in the single pixel when a photon is detected.

- Holes and electrons move in the drift region with a similar velocity (due to the high electric field), the time for their collection, called *collection time* is of the order of 50 ps.
- The *breakdown time* is the time that occurs for the avalanche to bring all the juction in breakdown.
- *Time of avalanche propagation*, depends on the region of the photon interaction. The total propagation time is in the order of hundreds of picoseconds.
- The *Drif Time* of the carriers generated outside the active area, is the time they need to reach the drift area. Outside the depleted region the electric field is much more lower and consequently the drift time is slower and can lead to a time delay.

4.5 Dynamic Range

The dynamic range of a SiPM, namely the optical signal level range over which the detector provides a useful output, extends from the lowest signal level detectable to the highest signal obtained when every microcell reveals simultaneously incident photons. In this condition the output signal is saturated and it is not possible to reveal any other photon until one or more pixels return in Geiger mode, after the necessary hold-off time. At this point, the output signal completely saturates, since no more microcells are available to detect incoming photons until some of the microcells have recovered back to their sensitive (charged) state.

The dynamic range of an SiPM is therefore a function of the total number of microcells and the PDE of the device, which is in turn a function of the bias voltage V_{bias} and wavelength of the incident photons.

The number of microcells fired as a function of the number of incident photons can be approximated by the expression:

$$N_{fired}(M, V, \lambda) = M \left(1 - e^{\frac{-PDE(\lambda, V_{bias}) N_{ph}}{G}}\right). \tag{4.5}$$

where N_{fired} is the number of microcell fired, N_{ph} is the number of incident photons and M is the number of SiPM microcells.

The expression also assumes that the incoming photons are uniformly distributed across the surface of the SiPM.

At low optical signal levels the SiPM photocurrent is proportional to the incident optical power, giving a linear detector response. As the optical power increases the SiPM photocurrent begins to deviate from linearity due to the limited number of microcells, and finally saturates. [68].

4.6 Noise components of a SiPM

Noise in SiPMs is represented by output current pulses produced in absence of incident light. A SiPM generates three different noise components: dark noise also called dark counts (DC), optical cross-talk (CT) and after-pulses (AP).

4.6.1 Dark count rate

The main source of noise in an SiPM is the dark count rate (DCR), which is primarily due to thermally generated electrons that create an avalanche in the high field region. The signals resulting from the breakdown of the cell, due to either photoelectrons or thermally generated electrons, are identical. Therefore, these electrons form a source of noise at the single photon level. If a threshold can be set above the single photon level, false triggers from the noise can be avoided, but the dark counts will always form a contribution to the measured signal. [68]. The physical process for the dark rate is due to the Silicon structure and it is exlained by the Shockley-Read-Hall (SRH) theory: the electron in transition between bands passes through a new energy state (localized state) created within the band gap by an impurity in the lattice; such energy states are called deep-level traps. The presence of recombination center is particularly due to imperfection in the lattice, which in turn are caused by impurities of the semiconductor or after an exposition to high energy radiation. The temperature plays an important role in the dark rate, in fact it decreases with the temperature from the order of MHz/mm^2 at room temperature to less than 1kHz/mm^2 at 100K [69].

4.6.2 Crosstalk

When undergoing an avalanche, carriers near the junction emit photons as they are accelerated by the high electric field. These photons tend to be in the near infrared region and can travel substantial distances through the device.
Typically $2 \cdot 10^5$ photons are emitted per electron crossing the junction. These photons can travel to neighboring microcells and may initiate a subsequent Geiger avalanche there. The crosstalk probability is the probability that an avalanching microcell will initiate an avalanche in a second microcell. The process happens instantaneously and, as a consequence, single photons may generate signals equivalent to a 2, 3 or higher photoelectron event. The optical crosstalk probability is a function of SiPM over-voltage and the distance between neighboring microcells, and can be estimated by the ratio of the count rate at the second photoelectron level to the count rate at the single photoelectron level.

An other type of cross talk is the electrical cross talk, which happens when the carriers generated during the avalanche propagate across the p^+ region, which is common to al the cells. At this point they can be absorbed from neighbouring pixels and trigger new avalanches.

The cross talk can be diminuished or increasing the distance between the active zones of two pixels or insulating the microcell with an optical trench made with an oxide.

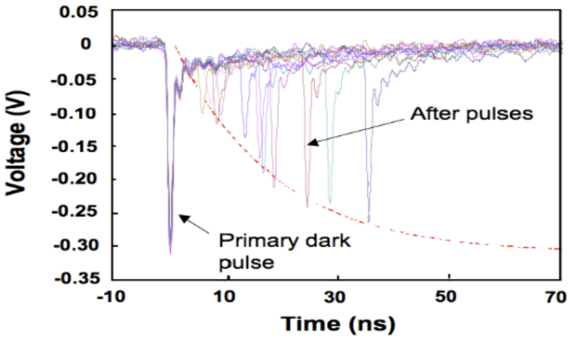

FIGURE 4.9: Primar pulse and afterpulsing.

4.6.3 AfterPulsing

After-pulsing is due to charge carriers, trapped in silicon defects during the avalanche multiplication, that are released later or during the recharge phase of the SiPM pixel. The net effect is that a new current pulse is observed on the tail of the original pulse, see Fig. 4.9.

After-pulse probability increases more than linearly with the overvoltage. The amount of charge released in an after-pulse depends on the time delay Δt between the primary and secondary avalanches.The after-pulse contributes to the noise only if the photon is relaxed after the hold-off time, because during it, the electric field is not high enough to produce an avalanche. Consequently an efficient way to limit the afterpulsing is to increase the hold-off time with very high quenching resistors.

Chapter 5

LCE study for SiPM future application in XENONnT

XENON1T has a design sensitivity for spin independent WIMP nucleon cross section of $1.6 \cdot 10^{-47}$ cm^2, a factor 100 below the XENON100 best limit. To achieve another order of magnitude in sensitivity, the XENON collaboration plans to build and install inside the same XENON1T cryostat a new detector with about three times the active LXe mass and with even lower background. The new experiment, named **XENONnT**, will use the same shield, cryogenic plants and DAQ system of XENON1T.

With a LXe target mass of ~ 6 tons, compared to the current 2 tons, the sensitivity to spin-independent WIMP-nucleon elastic scattering cross sections can reach the value of $\sigma_{SI} = 1.6 \cdot 10^{-48}$ cm^2 in a 20 t $\cdot$ y exposure [70].

XENONnT won't only increase the WIMP sensitivity by an order of magniture, but it will also probe with higher statistics a potential signal seen by XENON1T.

Furthermore it will open the possibility to probe other physics channels, such as the detection of solar ^{8}B neutrinos via coherent neutrino scattering or the search for the neutrinoless double beta decay in ^{136}Xe.

For the achievement of this upgrade, an intense *R&D* is carried out. Different solutions are explored, such as different geometries for the TPC and different mechanisms for the light collection.

The parameter that measures the light collection is the **LCE** (**L**ight **C**ollection **E**fficiency). It is defined as the fraction of emitted photons reaching the PMTs. It depends on the position of the interaction in the active volume and on the optical properties of LXe and of the materials around it.

The study of the LCE has been performed with the **GEANT4** tookit.

In this work we study the possibility of using SiPMs for the light collection and we provide an estimation of the reachable LCE.
We first study a configuration with SiPMs only in the bottom and top of the TPC and secondly a TPC with also a lateral coverage of SiPMs. The improved LCE is then translated in the capability to detect low energy nuclear recoil, lowering thus the energy threshold of the detector. The sensitivity, expressed as number of WIMP interaction above threshold is then estimated.

5.1 Optical photons and their interactions

The search of dark matter in the XENON experiments relies on the detection of the interaction of a WIMP with a xenon nucleus. Its detection depends on the collection of the light produced in the interaction. The photon, emitted in the process that follows such a collision, has a wavelenght of $\lambda \sim 178$ nm, in the ultra-violet range.

In GEANT4, optical photons (including also UV photons) are treated as a class of particle distinct from their higher energy gamma cousins. This implementation allows the wave-like properties of electromagnetic radiation to be incorporated into the optical photon process.
The GEANT4 catalogue of processes at optical wavelengths includes refraction and reflection at medium boundaries, bulk absorption and Rayleigh scattering. Each of these phenomena is described with a specific parameterization in the code.

We briefly recall each process and how it is coded in GEANT4:

Reflection The most frequent process inside the TPC for optical photons is the reflection. In GEANT4, reflection at an interface between two adiacent media is treated differently according to the materials. For the simple case of a perfectly smooth interface between two dielectric materials, all the user needs to provide are the refractive indices of the two materials stored in their respective *G4MaterialPropertiesTable*. In all other cases, the optical boundary process relies on the concept of *surfaces*. The information is split into two classes. One class, in the material category, keeps information about the physical properties of the surface itself, and a second class, in the geometry category, holds pointers to the relevant physical and logical volumes involved and has an association to the physical class. The former is called a **border surface** while the latter is referred to as the **skin surface**. This second type of surface is useful in situations where a volume is coded with a reflector and is placed into many different mother volumes [64].

Rayleigh Scattering The Rayleigh scattering is the elastic scattering of light by particles much smaller than the wavelength of the radiation. Rayleigh scattering results from the electric polarizability of the particles. The oscillating electric field of a light wave acts on the charges within a particle, causing them to move at the same frequency. The particle therefore becomes a small radiating dipole. We see the radiation as scattered light [64].

Absorption An other important process for optical photon is the absorption. It determines the lower limit in the window of transparency of the radiator. The implementation in the code of bulk absorption, *G4OpAbsorption*, is trivial. The process merely kills the particle. The procedure requires the user to fill the relevant *G4MaterialPropertiesTable* with empirical data for the absorption length, which is the average distance traveled by a photon before being absorbed by the medium. In LXe the value of the absorption length is set to $\lambda_{absorption} = 50$ m [64].

Among the initial tests to understand the behaviour of optical photons, we looked at the distribution of arrival times on the PMTs of photons generated in different positions of the XENON1T TPC.
We defined a small cylinder with radius 0.1 mm and half height of 0.1 mm. We placed this cylinder in six relevant positions in the TPC.
Photons were generated isotropically from the cylinder. The center of each starting point is indicated in the table 5.1. The origin of the Z-axis is at the the top of the active volume.

	Bottom edge	Bottom center	Top edge	Top center	Middle edge	Middle center
(r, z) [mm]	478, -968	0, -968	478, -3	0, -3	478, -480	0, -480

Table 5.1: Position of the center of the cylinder used for the generation of photons.

In Fig. 5.1 we show the distribution of the arrival time of photons on the bottom PMT array (red line) and top PMT array (blue line).

The main differences on arrival times for the optical photons are due to the position along the vertical axis of the TPC. Photons generated at the bottom of the TPC have a short path in LXe before reaching the bottom PMT array and consequentely their arrival times are short. Only a small fraction of them reaches the top PMT array (Fig. 5.1(a)). The opposite happens if photons are generated in the top part of the TPC: most of them are detected in a short time by the upper PMTs array, but a consistent part of photons reaches the lower array thanks to the total internal reflection between the LXe and the GXe. (Fig. 5.1(c))
We see the effect of reflection also in the time arrival distribution of photons generated in the middle part of the TPC. The majority of photons is collected by the bottom

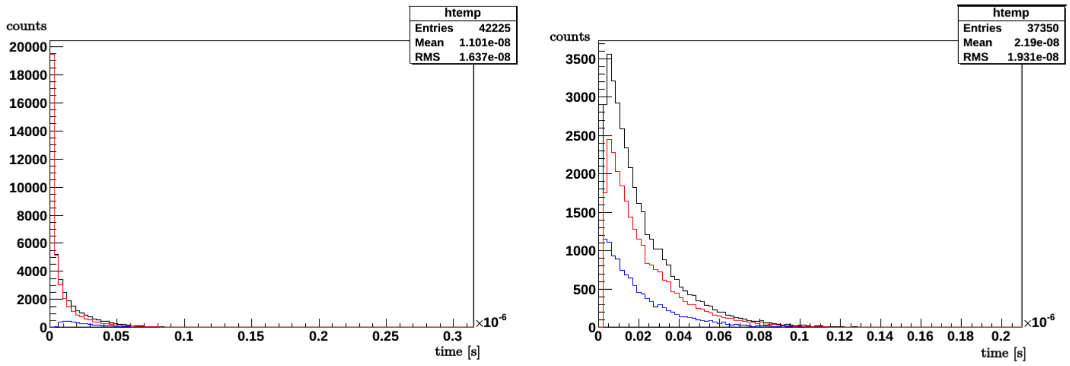

(a) Bottom left

(b) center left

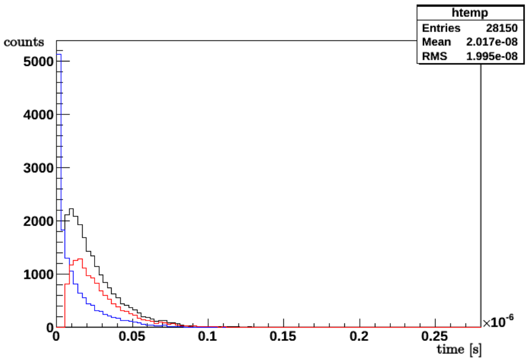

(c) top left

FIGURE 5.1: Distribution of the arrival time of photons on the bottom PMT array (red line) and top PMT array (blue line). In Black the total arrival time of photons. Photons are generated from a cilynder placed in the bottom left side of the TPC in 5.1(a), in the certer left side in 5.1(b) and in top left side in 5.1(c).

PMT array, after their reflection at the LXe/GXe surface. We see indeed that the tail of the distribution for the total arrival time is larger than in the two previous cases (Fig. 5.1(b)).

5.2 The XENONnT geometries

XENONnT is conceived as a fast upgrade of XENON1T: the infrastructure has been designed for a rapid deployment of an upgraded detector.

The muon veto for XENONnT will be the same one currently used, furthermore the support structure and levelling systems of XENON1T were designed to accomodate also an enlarged detector and the cryogenic system is able to handle an additional heat load. The GXe purification system is modular and scalable, and the Kr distillation column can fulfill XENONnT ^{85}Kr requirement. Currently the LXe storage capacity is of 7.6 tons, which is enough for the $\sim 6-7$ tons hypothesized for XENONnT.

The current dimension of the outer cryostat of XENON1T leaves the possibility of an

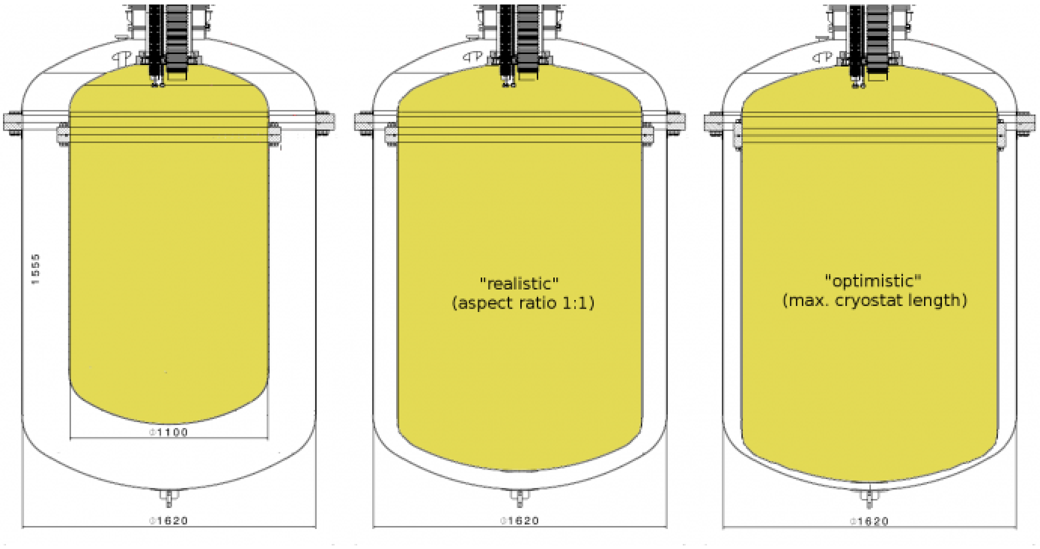

FIGURE 5.2: Sketch of the proposed inner vessels inside the outer cryostat.

easy upgrade of the experiment in terms of dimensions of inner cryostats and TPCs. A larger TPC implies a larger fiducial volume of LXe and the capability to increase the reduction of external backgrounds.

At the beginning of the work for this thesis, there were still various possible options for the geometry of the XENONnT TPC, named *Realistic*, *Optimistic*, *LZ* and *Draft-Design*.

The Realistic and Optimistic geometry The Realistic and Optimistic scenario were the first two hypotised geometries for the XENONnT TPC. Both of them are based on the dimensions of the XENON1T outer cryostat, and they are projected to fit into it without any modification. The final XENON1T cryostat design constrains the inner diameter of the outer cryostat to 1620 mm and limits the maximum possible increase of the TPC length to 357 mm (the space available below the XENON1T inner cryostat). The actual TPC in XENON1T has a radius $r = 479.25$ mm and and height of $h = 970$ mm.

The dimensions of the TPCs in these two preliminary geometries are shown in Table 5.2 and a sketch of them is presented in Fig. 5.2.

TABLE 5.2: Table of the dimension of the possible upgrade of XENON1T TPC in the Realistic and Optimistic geometry.

Scenario	Realistic	Optimistic
r (mm)	616.0	668.0
h (mm)	1232.0	1281.0

A larger TPC involves also a different number and pattern of the PMTs in order to cover the surface as much as possible. The number of the R11410 PMTs increases from

the current 248 to 394 (195 in the bottom plate plus 199 in the top one) in the Realistic option, and to 452 in the 0ptimistic one (222 in the bottom and 230 in the top).
We report in Table 5.3 the structural details of the two geometries.

Table 5.3: Reference dimensions and (G4) implemented dimensions of XENONnT detector parts.

	Realistic	Optimistic
ID outer cryostat	1620 mm	1620 mm
Outer cryostat cylinder height	1687 mm	1687 mm
Inner cryostat ID	1350 mm	1474 mm
Inner cryostat cylinder height	1687 mm	1687 mm
Bell diameter	1300 mm	1384 mm
Bell height	248 mm	248 mm
TPC diameter	1232 mm	1336 mm
TPC height	1232 mm	1282 mm
Liquid Xe diameter	1350 mm	1350 mm
Liquid Xe height	1232 mm	1282 mm
TPC active radius	616 mm	668 mm
Gate Z position	553 mm	568 mm
Cathode Z position	-678 mm	-714 mm
Z position top surface bottom PMTs	-737 mm	-772 mm
Z position top LXe surface above bell	854 mm	≃mm
Z position bottom LXe surface below TPC	-934 mm	≃ mm
Total number of PMTs	394 (195 bottom, 199 top)	452 (222 bottom, 230 top)

A direct competitor of the XENONnT experiment has been proposed in the US with the name of LZ (as the proponents come mainly from the previous LUX and ZEPLIN experiments), foreseen to be realized by 2020 in the Homestake underground laboratory.

The LZ geometry In order to compare the performances of XENONnT direcly with LZ, and to check the results claimed in their Conceptual Design Report [71], we implemented also a geometry similar to the LZ one. This geometry has a TPC that resembles the dimension of the TPC of LZ, it has a radius of r = 728 mm and a height of h = 1456 mm.
Due to the bigger dimension, this TPC doesn't fit the actual outer cryostat making this possibility not quick and easy to install. The number of hypotised PMT is 476 (223 in the top plate and 253 in the bottom one).
In the Fig. 5.3 we show a scheme of the three options.

The Draft-Design geometry Recently the collaboration fixed the final geometry for the XENONnT proposal, named here "Draft-Design". This geometry maximizes the dimensions of the TPC, with the constrain to fit the actual external cryostat. It is slightly larger that the Optimistic one, and with a longer drift length in the TPC. The

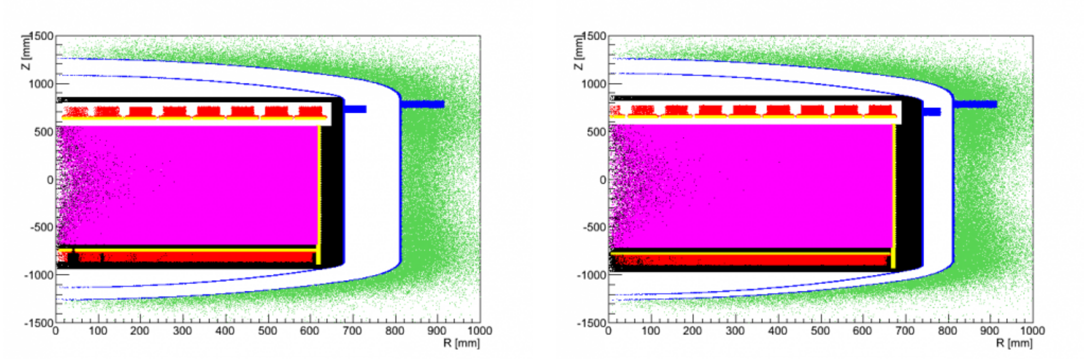

(a) Realistic scenario

(b) Optimistic scenario

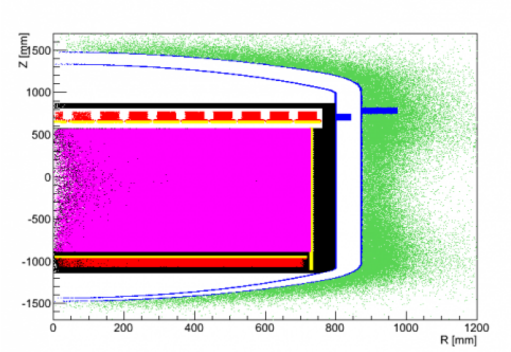

(c) alaLZ scenario

FIGURE 5.3: In blue the Cryostat; in red the PMTs; in yellow the PTFE; in purple the active LXe volume; in black the LXe below the cathode, and outside the TPC; in green the position of the neutron capture in a potential Gd-loaded LS buffer outside the outer cryostat.

number of top PMTs is 223, while the number of bottom PMTs is 253, for a total of 476 PMTs.

The main geometrical characteristics of the Draft-Design geometry are reported in Table 5.4.

	Draft-Design
TPC diameter (mm)	1368
TPC height (mm)	1446
Active LXe (t)	∼6
Total LXe (t)	∼8
Cryostat (kg)	1600
PTFE (kg)	170
Total number of PMTs	476 (top 223, bottom 253)

TABLE 5.4: Geometric characteristics of the Draft-Design geometry.

5.3 The XENONnT Monte Carlo simulation

This work is performed on the XENONnT Monte Carlo simulation based on the GEANT4 toolkit.

In GEANT4 the tracking of the various particles is divided into steps, whose length is automatically chosen according to the type and energy of the particle, and to the characteristics of the medium. For each step of all the particles inside the LXe target, we record the position, time, deposited energy, particle type and the process responsible for the energy loss.

In order to cross check the initial results, we started this work with the calucation of the Light Collection Efficiency (LCE) for XENON1T and compared it with the results published in [61].

Secondly we extended the analysis to XENONnT: we improved various parts of the simulation code implementing in particular the various reflective components in the TPC, in order to increase the LCE. Lastly we changed the light collection sensors in XENONnT, from the current option of PMTs to a potential improvement using SiPMs with various coverage inside the TPC.

5.3.1 LCE in XENON1T

The first exercise to learn confidence with the code was the reproduction of the LCE map, namely the LCE as a function of the position in the TPC, for the XENON1T experiment. The parameters used in the simulation have been studied through several measurements of the optical properties of LXe throughout the years [61].

For the refractive index it was used the average value of 1.63 and the Rayleigh scattering length, which affects the mean free path of photons, was set to 30 cm. Another parameter of interest is the absorption length which mostly depends on the amount of impurities present in the LXe (O_2 and H_2O) and is therefore dependent on the performance of the purification system. We consider a conservative value of 50 m.

The quartz of the PMT window is a material whose optical properties must be properly defined, as it governs the amount of light transmitted to the photocathode. We chose a refractive index of 1.59 for a wavelength of 178 nm.

The photocathode is modeled as a fully-opaque thin layer, placed on the inner side of the PMT window where photons are absorbed. Apart from the cut-outs needed to host the PMTs, the inner surface of the TPC is entirely made of PTFE in order to reflect as much VUV light as possible. We assumed a 99% PTFE reflectivity in this study.

The layer of GXe located between the LXe and the top PMT array is characterized by

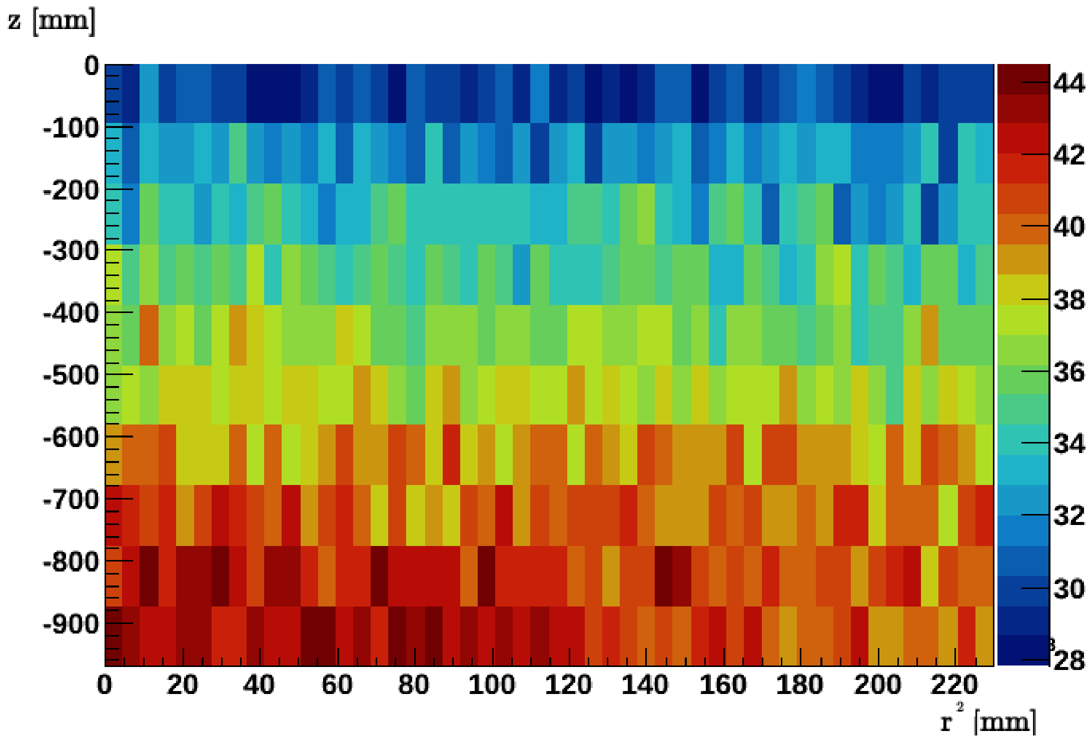

FIGURE 5.4: Map of the LCE for XENON1T.

a refractive index equal to 1.

Lastly, there are five electrodes used to define the electric field within the TPC. Four of them are hexagonally etched meshes: the top and bottom screening meshes and gate meshes have an optical transparency of 94%, while that of the anode is 93%. The cathode is made of thin wires and presents an optical transparency of 96%.

In this study, photons are generated uniformly and isotropically in the full volume of the TPC, and the LCE is calculated for each individual R^2, Z pixel, using the axial symmetry of the TPC.

A map of the variation of LCE inside the TPC is shown in Fig. 5.4.

Given the internal reflection occurring at the liquid/gas interface, the LCE is higher close to the bottom PMT array, in particular in the center of the TPC, and decreases when moving closer to the anode due to the increase in path length, leading to absorption of photons.

The average LCE value obtained is: 36.73% in good agreement with the results of [61].

5.3.2 LCE in XENONnT

The starting point of this work was a rough (not optimized for the optical simulations) Monte Carlo simulation of the XENONnT detector with a LCE values of ∼ 8%. From a quick comparison with the value of LCE in XENON1T, which is ∼ 37%, it is obvious

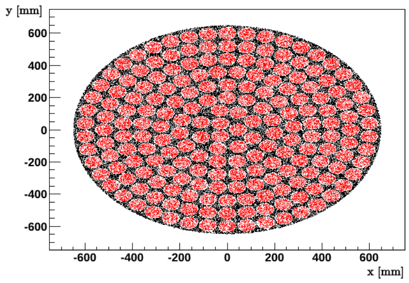

(a) A x-y view of the bottom of the TPC, in red the PMTs windows and in black the Bottom Reflector Plate.

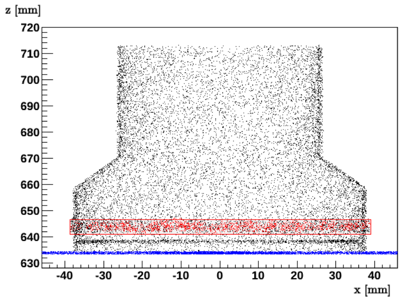

(b) Side view: A z-r view of a PMT and a reflector plate. The outer ring in visible in red at z = 638mm, in blue the reflector plate. The thickness of the bottom (and top) side reflector is 1mm. The PMT has a ring to keep it in position, the outer radius of which, r = 38.75 mm, is bigger than the radius of the pmt windows, r=32mm. The ring is few mm under the PMTs windows therefore the PTFE reflector is made thin enough not to overlap with the ring.

that many photons are lost during their propagation from the generation point to the PMT arrays.
In the *Physics List* of GEANT4, which is the class collecting all the particles and physics processes, it is possible to activate the *verbosity* of an event. In this way, the output file reports all the information about the propagation of the particles generated, and in our case, for each photon, which intecration it undergoes to.
I noticed that the main reasons for the poor LCE were, at first, the loss of photons in the lateral walls of the TPC, secondly the loss of photons in the space amongst PMTs and lastly the absorption of photons by the grids.

The loss of photons in the lateral walls of the TPC was solved with the introduction of an optical surface between the LXe and the TPC wall. When a photon reaches the edge of the TPC, if a reflecting surface is present, it is reflected and keeps travelling in the LXe and it is not lost outside the detector.
In this way, the possibility of the photon detection by a PMT increases, and the LCE as well.
Similarly, reflectors plates to cover the surface between the PMTs windows were missing. I defined, on the top and bottom of the TPC, two reflecting surfaces, called respectively Bottom Reflector Plate and Top Reflector Plate. The lateral, bottom and top side reflecting surfaces are made of PTFE.
These reflectors cover the surface between the PMTs windows. An image of the bottom of the TPC with the reflector among the PMTs, together with a lateral view of a PMT and the reflector can be seen in Fig. 5.5(a) and Fig. 5.5(b).

The last correction to the XENONnT code, was the proper value of the transparency of

the five electrodes used to apply the electric field within the TPC.
The transparency enters in the definition of the absorption length, namely the distance λ inside a material where the probability that a particle has not been absorbed has dropped to $1/e$. The Absorption Length is defined as:

$$AbsorptionLength = \frac{GridThickness}{-log(Transparency)} \tag{5.1}$$

The values of transparecy given to the grids are reported in Tab. 5.5.

	TopScreeningMesh	BottomScreeningMesh	AnodeMesh	GateMesh	CathodeMesh
Transparency	0.945	0.945	0.929	0.945	0.96

Table 5.5: Values of trasparency given to the grids.

These optimitation of the GEANT4 simulation code for XENONnT were done for the four geometries described in section 5.2. In Table 5.6, I report the value of LCE for each of them and, as a mean of comparison, the LCE value in XENON1T.

geometry	Realistic	Optimistic	AlaLZ	Draft-Design	XENON1T
LCE	40.85%	40.57%	39.99%	39.01%	36.73%

Table 5.6: LCE values for XENONnT in the four geometries and as a comparison XENON1T LCE.

From Table 5.6 we see that the four versions of the XENONnT geometry presents very similar values of the LCE. The difference in LCE values between XENON1T and XENONnT lies in the different implemented structure of the PMTs. In XENON1T, the real detector and its reconstruction, the PMTs are surrounded by a small ring to keep them in position. The ring is opaque, thus every time a photon hits this ring it is absorbed.
In the XENONnT detector reconstruction, this ring is not present, so the reflecting surface is larger. Consequently the number of photons eligible for the collection is larger, leading to a sligthly higher LCE.

In Fig. 5.5, the LCE map for the geometry Draft-Design, which is the definitive geometry foreseen by the XENON collaboration.

5.4 Simulation of a next generation TPC

A promising replacement candidate for the PMT is the SiPM, since its technology is rapidly developing and may become suitable for the read-out of large detectors, offering

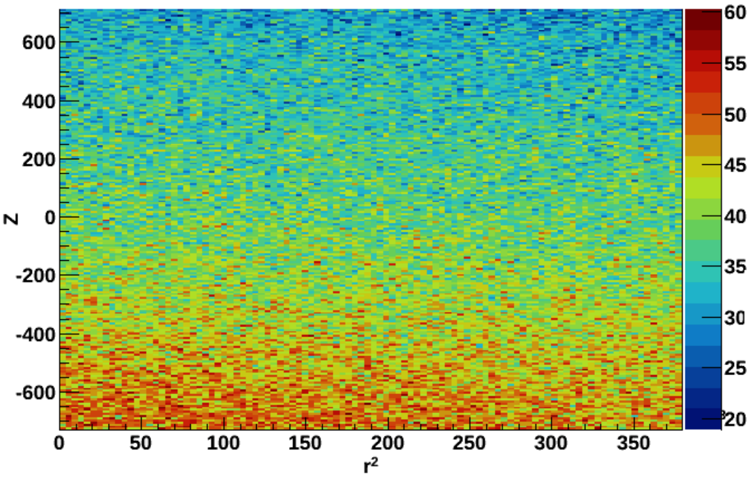

FIGURE 5.5: LCE map for the Draft-Design geometry.

very low radioactivity levels, compact geometry and low operation voltages. They would allow an increase of the photosensitive area of the TPC, and might be suitable for a 4π coverage, since they might be operated inside an electric field. Commercially available SiPMs operate well at LXe temperatures and are comparable to the state of the art of PMTs, having photodetection-efficiency (PDE) values of $\sim$ 10-25% at 178 nm and gains of a few 10^6 [72].

A Monte Carlo simulation of the XENONnT TPC explores the possibility of PMTs replacement with SiPMs.
At first, we fully covered the top and bottom part of the TPC with SiPM, replacing the area previously filled by PMTs and PFTE reflector. Secondly, we added SiPMs also to the lateral walls of the TPC.

To simulate the coverage of the top and bottom plates of the TPC with SiPMs, we built a SiPM surface with the same radius of the PTFE reflector. For example in the Draft-Design the radius of the bottom ssurface is r = 684 mm. The photocathode is implemented as a completely opaque disk, so that every photon reaching its surface is absorbed and available to be converted in the signal.
In Table 5.7, we report the values of LCE for the four different geometries obtained in this first step.

geometry	Realistic	Optimistic	AlaLZ	Draft-Design
LCE	60.81%	60.46%	59.57%	59.77%

TABLE 5.7: LCE values for XENONnT with SiPMs in the bottom and top face of the TPC.

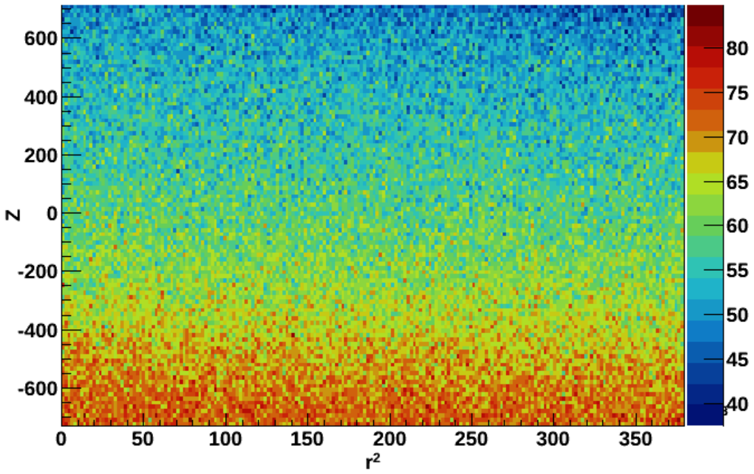

FIGURE 5.6: LCE map for the geometry Draft-Design. Optical photons were generated inside the TPC and collected by two surfaces, on top and bottom of the TPC. They mimic a coverage with SiPMs.

In Fig. 5.6 we show the LCE for the Draft-Design geometry with the implementation of SiPMs on the top and bottom face of the TPC.

The are various type of SiPMs and we study, for instance, a possible implementation with the Hamamatsu 12 × 12 mm (2 SiPM 10943- 3186), which is an array of 4 separate 6 mm, vacuum ultraviolet sensitive SiPMs, merged in one device [72]. Each 6 × 6 mm SiPM (segment) has its own 2 pins (cathode and anode). This gives the possibility of reading every segment separately or in various combinations. If the single read-out method would be employed inside a large-volume time-projection chamber, the high number of channels would be a disadvantage: every channel would need cabling, an amplifier and an ADC input channel. This provides the motivation to find a suitable method of reading more segments per channel [72]. For this reason, the SiPM has been tested by the XENON collaboration either in a single channel read out either in a multi-channel read out.
The read out of every single channel is not possible in term of electronics, every channel would need cabling, an amplifier and an ADC input channel and, considering the dimension of the TPC and of the single SiPM, that would involve a huge amount of cables. In a dual-phase TPC, the xy-reconstruction of an event is performed by using the information of the light intensity distribution across the photosensor array. A simulation of the XENON1T TPC, using a neural network for the position reconstruction trained with $5 \cdot 10^3$ photons, showed a typical resolution of 4.5 mm in the x-y plane [73]. Considering that, the area of the XENON1T PMTs is about 30 times bigger than the area of all the four segments of the given SiPMs, in XENONnT there will be no need to read the segments separately. The required xy-position resolution of a few mm allows to combine

more SiPM segments in one channel, reducing the total number of read out channels [72].

The values of LCE obtained for the various geometries must be corrected by the **Fill Factor**, namely the sensitive area per channel ratio. We calculate the active area for a tile made of 4 (6 × 6 mm) SiPMs over the total area. The fill factor of a single SiPM ($F.F._{SiPM}$) is :

$$F.F. = \frac{A_{active}}{A_{total}} = 61.8\% \tag{5.2}$$

Assuming to cover completely the top and bottom side with SiPM, the value of the LCE corrected by the fill factors are reported in Table 5.8.

geometry	Realistic	Optimistic	AlaLZ	Draft-Design
LCE	37.58%	37.36%	36.81%	36.93%

Table 5.8: LCE values for XENONnT with SiPMs in the bottom and top face of the TPC.

These values are of the same order of magnitude of the LCE obtained in the simulation of the XENON1T TPC instrumented with PMTs. An advantage of the use of a smaller detection module, such a tile of SiPM which is ∼ 17 times smaller than a PMT, is that the borders of the TPC can be covered better.

In XENON1T the outer ring of PMTs oversteps the external limit of the TPC, in this way it is possible to reduce the loss of light at the borders. Nevertheless, we see that the LCE value at the border is lower than in the middle (see Fig.5.4). In the implementation with SiPM, as seen in Fig. 5.6 for the Draft-Design, the dependence of the LCE value with r^2 is smaller. We obtain thus an higher resolution even for events at the border.

The next step was to simulate a 4π SiPMs coverage. For this purpose we added a SiPM surface also to the lateral walls of the TPC.

One of the advantages of SiPMs is that they can work also inside high electric fields. PMTs instead, when coupled with a high electric field, don't work properly.

With such an implementation, the sensible area grows considerably and consequently the LCE.

In Table 5.9 we report the values of LCE, corrected for the Fill-Factor, for a TPC covered entirely of SiPM. In Fig. 5.7 we show the LCE map for the geometry Draft-Design with the implementation of SiPMs also in the lateral walls of the TPC. We see that a 4π

geometry	Realistic	Optimistic	AlaLZ	Draft-Design
LCE	56.80%	56.54%	55.08%	56.39%

Table 5.9: LCE values (corrected by the Fill-Factor) for the XENONnT TPC covered by SiPMs in the four different geometries

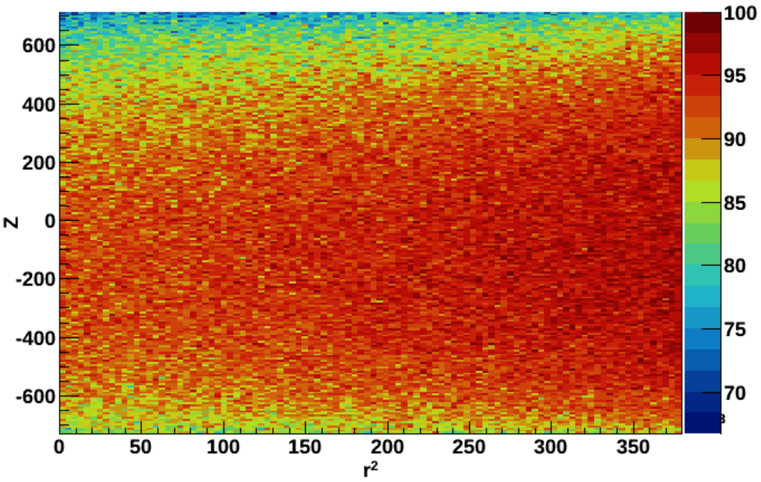

FIGURE 5.7: LCE map for the geometry Draft-Design. Optical photons were generated inside the TPC and collected by three surfaces, on top and bottom of the TPC and on the lateral walls.

coverage shows a LCE value larger at the center of the TPC. Considering that we use the internal part of the LXe as a fiducial volume, this is a very promising result.

5.5 NR Energy threshold and LCE

The value of the LCE is crucial if we want to estimate the energy threshold to a nuclear recoil interaction.

To convert the energy deposited in the active LXe, E_d, into light S1 and charge S_2 signal, we first need a model which predicts the amount of generated photons and electrons. The light yield $\mathcal{L}_y(\overline{r})$ is defined as the specific number of detected photoelectrons (PE) per keV, and it is traditionally referred to the 122 keV γ emitted by a ^{57}Co source, at zero electric field. The average photon yield, Ph_y, of this γ line is 63.4 ph/keV. For nuclear recoil (NR), the photon yield is parameterized in terms of the so-called relative scintillation efficiency in LXe, $\mathcal{L}_{eff}$. Similarly to the light yield, $\mathcal{L}_{eff}$ is defined with reference to Ph_y.

The average number of photons producted in a nuclear recoil interaction is:

$$N_{ph}^{NR} = E_d \cdot \mathcal{L}_{eff} \cdot Ph_y \cdot S_{NR} \tag{5.3}$$

where $S_{NR} = 0.95$ is the light yield suppression factor for NR, due to the electric field. Photons are converted into the S1 signal by applying the position-depedent light collection efficiency $f_{PE}(\overline{r})$, which is a function of the LCE. We compare the LCE of a TPC instrumented with PMTs on the top and bottom plate, and of a TPC with a 4π

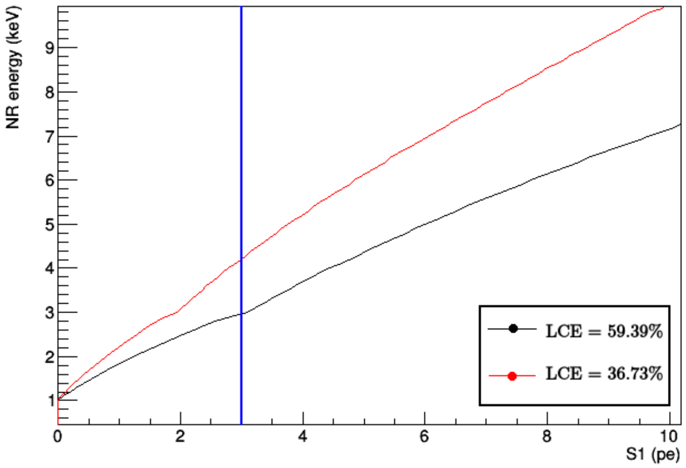

FIGURE 5.8: NR energy vs S1. The red line represents a LCE value of 36.93% (XENON1T), the black line a value of 59.39% (XENONnT). The blue vertical line is set at 3 pe, the lowest S1 detectable.

coverage with SiPMs. The LCE values for the Draft-Design geometry of XENONnT in the two scenarios are derived in section 5.4.

If the light is collected by PMTs, the probability for an emitted photon to be converted in a photoelectron signal, $f_{PE}, (\overline{r})$ can be expressed as:

$$f_{PE}(\overline{r}) = LCE(\overline{r}) \cdot PE \cdot QE \tag{5.4}$$

where QE is the average quantum efficiency of the PMT ($\sim 35\%$) and CE is the average collection efficiency from the photocathode to the first dynode ($\sim 90\%$).

If the light is collected by SiPMs, the $f_{PE}(\overline{r})$ becomes:

$$f_{PE}(\overline{r}) = LCE(\overline{r}) \cdot PDE \tag{5.5}$$

where PDE is the photon detection efficiency, which is defined in 4.3. Typical values of PDE are in the range $\sim 10-20\%$. We assume a value of PDE of 20%.

The LCE value, for the TPC instrumented with PMT, is 36.93%. This value is lower than the LCE value (corrected by the Fill Factor) in the Draft-Design with the 4π coverage of SiPMs, 56.39%. Of course, with a larger LCE value, more photons are converted into the S_1 signal, and the experiment becomes thus sensitive to lower energy deposit.

In Fig. 5.8 we show the relation between the S_1 signal and the energy deposited. So far in the XENON experiments we required to have at least 3 different PMTs with 1 pe, so the minimim S1 signal value accepted in the data analysis is 3 pe. We draw a blue vertical line in correspondence to this value of the S1 threshold.

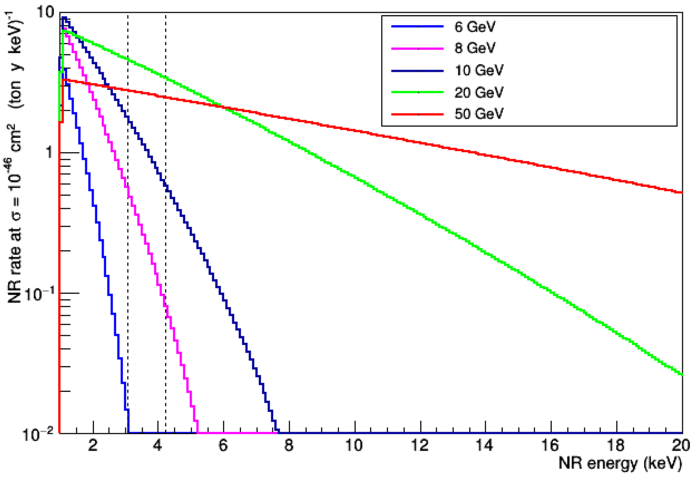

Figure 5.9: Expected wimp as a function of the NR enery for different values of masses.

With a 3 pe S1, the value of the nuclear recoil energy threshold for different values of LCE are reported in Table 5.10.

LCE	NR energy threshold [keV]
36.93%	4.22
56.39%	3.05

Table 5.10: NR energy threshold [keV] for different LCE values

We can now estimate the improvement in the expected number of WIMP interactions due to the capability to lower the detector threshold. In Fig. 5.9 we show the NR spectrum of the WIMP interaction for different WIMP masses, together with the two energy thresholds obtained in Table 5.10. In Table 5.11 we present the number of interactions with the same two thresholds, and their ratio. They are calculated assuming a WIMP-nucleon cross section $\sigma = 1 \cdot 10^{-46}$ cm^2, and they are expressed as events per tonne per year. In particular, for low mass WIMP, the increase in the number of detected interactions is significant, allowing for a large improvement in sensitivity to study the low mass WIMP region.

WIMP mass [GeV]	Thr = 3.05 keV	Thr = 4.22 keV	Ratio
6	0.0325	0	/
8	3.73	0.421	8.84
10	19.3	5.73	3.37
20	168	120	1.4
50	277	246	1.13

Table 5.11: Expected number of interaction for different NR energy threshold. They are calculated assuming a WIMP-nucleon cross section $\sigma = 1 \cdot 10^{-46}$ cm^2, and they are expressed as events per tonne per year.

5.6 Conclusions

SiPMs look to be very promising devices for next generation noble liquids dark matter search experiments. Their stronger advantage is the possibility of working also inside high electric fields.

This allows the instrumentation of the lateral walls of the TPC, offering an increase of 20% on the LCE value. The LCE is one of the crucial parameters for the formation of the signal S1. We showed that with a 4π TPC coverage of SiPMs we can reach a energy threshold for NR of about 3 keV. Considering low mass WIMP, we estimate that the improvement in the total number of detected events can be about a factor 9 for a 8 GeV WIMP, increasing significantly the sensitivity in the search for such a feeble signal.

Conclusions

The question about the composition of the Universe is today one of the most challenging open questions in physics. Despite the scientific achievement of the last decades in the astrophysical and cosmological fields, the majority of the Universe energy content is still unknown. Experimental results, based both on the direct and indirect detection of Dark Matter have not yet confirmed any positive signal from such a kind of matter. Due to the very small cross section for WIMP interactions, the number of expected events is very limited ($\sim$ 1 ev/tonne/year), thus requiring detectors with large target mass and low background level. The use of double phase, LXe/GXe, TPC represents one of the most promising techniques for this kind of search.
XENON1T, currently in data acquisition at LNGS, is the first tonne scale LXe-based detector, its aim is to detect a WIMP-nucleon interaction. With XENON1T, we aim to reach a sensitivity for the spin-independent WIMP-nucleon interaction of $1.6 \cdot 10^{-47}$ cm^2 in 2 t·y, which requires a background reduction by two orders of magnitude with respect to the XENON100 detector. The XENON1T TPC is surrounded by an active veto system to tag muons and muon-induced backgrounds. The Muon Veto consists of a water Čherenkov detector of $\sim$ 10m height and diameter, equipped with 84 8-inch photomultipliers and cladded with a reflective foil.
We studied different trigger configurations of the Muon Veto and we compared the results with a Monte Carlo simulation, obtaining a very good agreement. This gives the opportunity to safely use the simulation to study and compute the Muon Veto tagging efficiency. With the trigger requirements used in the Muon Veto during the current XENON1T *Science Run 0* (8 PMTs in coincidence, in a time window of 300 ns, with a threshold of 1 pe) we obtain a tagging efficiency of $\eta_{\mu} = 99.5\%$ for crossing muon events and $\eta_{shower} = 43\%$ for showering muons events.
Given these efficiencies, it is possible to calculate the expected background in the *Science Run 0*, which corresponds to $1.3 \cdot 10^{-3}$ events in 1 tonne fiducial volume, practically negligible.

The future upgrade of the experiment, named XENONnT, is already forseen by the collaboration. It will be conceptually identical to XENON1T but with a larger TPC and

bigger xenon target ($\sim 6\,t$), to improve the WIMP sensitivity by an order of magnitude. In this work a preliminary study on the geometries of the XENONnT TPC was carried out, together with the analysis of a possible replacement of PMTs with SiPMs.
The replacement with SiPMs allows the instrumentation also of the lateral walls of the TPC, offering an increase of 20% on the LCE value. The LCE is one of the crucial parameters for the formation of the signal S1. We showed that with a 4π TPC coverage of SiPMs we can reach a energy threshold for NR of about 3 keV. Considering low mass WIMP, we estimate that the improvement in the total number of detected events can be about a factor 9 for a 8 GeV WIMP, increasing significantly the sensitivity in the search for such a feeble signal.

Bibliography

[1] F. Zwicky. The coma cluster of galaxies. *Publications of the Astronomical Society of the Pacific*, pages 61–71, 1951.

[2] R. H. Sanders K. G. Begeman, A. H. Broeils. Extended rotation curves of spiral galaxies: Dark haloes and modified dynamics. *Monthly Notices of the Royal Astronomical Society*, 249(3):523–537, 1991.

[3] C. Alcock et al. The macho project: microlensing results from 5.7 years of large magellanic cloud observations. *The Astrophysical Journal*, 542(1):281, 2000.

[4] M. Markevitch D. Clowe, A. Gonzalez. Weak lensing mass reconstruction of the interacting cluster 1E0657-558: Direct evidence for the existence of dark matter. *The Astrophysical Journal*, 604(2):596, 2004.

[5] R.W. Wilson A.A. Penzias. A measurement of excess antenna temperature at 4080 mc/s. *The Astrophysical Journal*, 142:419–421, 1965.

[6] P. A. R. Ade et al. Planck 2013 results. xv. cmb power spectra and likelihood. *Astronomy & Astrophysics*, 571:A15, 2014.

[7] C. L. Bennett et al. Nine-year wilkinson microwave anisotropy probe (wmap) observations: final maps and results. *The Astrophysical Journal Supplement Series*, 208(2):20, 2013.

[8] A.R. Liddle 0. Lahav. The Cosmological Parameters 2014. *Review of Particle Data Group*, 2014.

[9] W. de Boer et al. Egret excess of diffuse galactic gamma rays interpreted as a signal of dark matter annihilation. *arXiv preprint astro-ph/0602325*, 2006.

[10] P. J. Peebles A. M. Ostriker. A numerical study of the stability of flattened galaxies: or, can cold galaxies survive? *The Astrophysical Journal*, 186:467–480, 1973.

[11] H. R. Quinn R. D. Peccei. Cp conservation in the presence of pseudoparticles. *Physical Review Letters*, 38(25):1440, 1977.

[12] M. S. Turner. Cosmic and local mass density of "invisible" axions. *Physical Review D*, 33(4):889, 1986.

[13] Mourad Tamazouzt. The primakoff effect at high energy. *Physics Letters B, Volume 211, Issue 4, p. 477-480*, 112(091303), 1988.

[14] K. Zioutas et al. First results from the cern axion solar telescope. *Physical review letters*, 94(12):121301, 2005.

[15] E. Zavattini et al. New pvlas results and limits on magnetically induced optical rotation and ellipticity in vacuum. *Physical Review D*, 77(3):032006, 2008.

[16] E. Aprile et al. (XENON Collaboration). First axion results from the xenon100 experiment. *Physical Review D*, 90(6):062009, 2014.

[17] K. Griest G. Jungman, M. Kamionkowski. Supersymmetric dark matter. *Physics Reports*, 267(5):195–373, 1996.

[18] P. Gondolo. Phenomenological introduction to direct dark matter detection. *arXiv preprint hep-ph/9605290*, 1996.

[19] E. Witten M. W. Goodman. Detectability of certain dark-matter candidates. *Physical Review D*, 31(12):3059, 1985.

[20] M. Yamaguchi T. Moroi, H. Murayama. Cosmological constraints on the light stable gravitino. *Physics Letters B*, 303(3):289–294, 1993.

[21] A. Vilenkin V. Berezinsky, M. Kachelriess. Ultrahigh energy cosmic rays without greisen-zatsepin-kuzmin cutoff. *Physical Review Letters*, 79(22):4302, 1997.

[22] E. Aprile et al. (XENON100). Dark matter results from 225 live days of xenon100 data. *Phys. Rev. Lett.*, 109(181301), 2012.

[23] D. S. Akerib et al. (LUX Collaboration). First results from the lux dark matter experiment at the sanford underground research facility. *Phys. Rev. Lett.*, 112(091303), 2014.

[24] D. Akerib et al. (LUX Collaboration). Results from a search for dark matter in the complete lux exposure. *arXiv.org*, 118(2), 2017.

[25] F. Agostini. Caratterizzazione e calibrazione dei fotomoltiplicatori del sistema di veto di muoni per l'esperimento xenon1t. Master's thesis, Alma Mater Studiorum - University of Bologna, 2013.

[26] R. Bernabei et al. The annual modulation signature for dark matter: Dama/libra-phase1 results and perspectives. *Advances in High Energy Physics*, 2014, 2014.

[27] K. Blum. Dama vs. the annually modulated muon background. *arXiv preprint arXiv:1110.0857*, 2011.

[28] R. Bernabei et al. No role for muons in the dama annual modulation results. *European Physical Journal C-Particles and Fields*, 72(7):1, 2012.

[29] A. Pierce N. Weiner I. Yavin S. Chang, J. Liu. Cogent interpretations. *Journal of Cosmology and Astroparticle Physics*, 2010(08):018, 2010.

[30] E. Armengaud et al. Search for low-mass wimps with edelweiss-ii heat-and-ionization detectors. *Physical Review D*, 86(5):051701, 2012.

[31] R. Agnese et al. Improved wimp-search reach of the cdms ii germanium data. *Physical review letters*, 92, 2015.

[32] G. Angloher and al. Results on light dark matter particles with a low-threshold cresst-ii detector. *The European Physical Journal C*, 76(1):25, 2016.

[33] G. Angloher et al. Results on low mass wimps using an upgraded cresst-ii detector. *The European Physical Journal C*, 74(12):1–6, 2014.

[34] R. Agnese et al. Silicon detector dark matter results from the final exposure of cdms ii. *Physical Review Letters*, 111(25):251301, 2013.

[35] C. E. Aalseth et al. Cogent: A search for low-mass dark matter using p-type point contact germanium detectors. *Physical Review D*, 88(1):012002, 2013.

[36] A. Gütlein. Feasibility study for a first observation of coherent neutrino nucleus scattering using low-temperature detectors. Master's thesis, Technische Universitat Munchen.

[37] K. Choi and al. (Super-Kamiokande Collaboration). Search for neutrinos from annihilation of captured low-mass dark matter particles in the sun by super-kamiokande. *arXiv:1503.04858v1*, 2015.

[38] E. Aliu et al. Veritas deep observations of the dwarf spheroidal galaxy segue 1. *arXiv preprint arXiv:1202.2144*, 2012.

[39] P. F. Michelson, W. B. Atwood, and S. Ritz. Fermi gamma-ray space telescope: High-energy results from the first year. *Rept. Prog. Phys.*, 73:074901, 2010.

[40] Z. Ahmed et al. Results from a low-energy analysis of the cdms ii germanium data. *Physical Review Letters*, 106(13):131302, 2011.

[41] S.C. Park C. Rott, K. Kohri. Superheavy dark matter and icecube neutrino signals: bounds on decaying dark matter. *arXiv preprint arXiv:1408.4575*, 2014.

[42] R. Abbasi et al. Search for dark matter from the galactic halo with the icecube neutrino telescope. *Physical Review D*, 84(2):022004, 2011.

[43] M. Aguilar et al. Electron and positron fluxes in primary cosmic rays measured with the alpha magnetic spectrometer on the international space station. *Physical review letters*, 113(12):121102, 2014.

[44] O. Adriani et al. Pamela results on the cosmic-ray antiproton flux from 60 mev to 180 gev in kinetic energy. *Physical Review Letters*, 105(12):121101, 2010.

[45] T. Gong Q.H. Cao, C.R. Chen. Leptophilic dark matter and ams-02 cosmic-ray positron flux. *arXiv preprint arXiv:1409.7317*, 2014.

[46] E. Aprile et al. (XENON Collaboration). Design and performance of the xenon10 dark matter experiment. *Astroparticle Physics*, 34(9):679–698, 2011.

[47] E. Aprile et al.(XENON Collaboration). The xenon100 dark matter experiment. *Astroparticle Physics*, 35(9):573–590, 2012.

[48] E. Aprile et al.(XENON Collaboration). Limits on spin-dependent wimp-nucleon cross sections from 225 live days of xenon100 data. *Physical review letters*, 111(2):021301, 2013.

[49] E. Aprile et al. (XENON Collaboration). The xenon1t dark matter search experiment. In *Sources and Detection of Dark Matter and Dark Energy in the Universe*, pages 93–96. Springer, 2013.

[50] T. Doke E. Aprile. Liquid xenon detectors for particle physics and astrophysics. *Reviews of Modern Physics*, 82(3):2053, 2010.

[51] P. Majewski K. Ni M. Yamashita E. Aprile, K.L. Giboni. Observation of anticorrelation between scintillation and ionization for mev gamma rays in liquid xenon. *Physical Review B*, 76(1):014115, 2007.

[52] J. Angle et al. First results from the xenon10 dark matter experiment at the gran sasso national laboratory. *Physical Review Letters*, 100(2):021303, 2008.

[53] D. S. Akerib et al. Limits on spin-independent interactions of weakly interacting massive particles with nucleons from the two-tower run of the cryogenic dark matter search. *Physical review letters*, 96(1):011302, 2006.

[54] J. Angle et al. Limits on spin-dependent wimp-nucleon cross sections from the xenon10 experiment. *Physical review letters*, 101(9):091301, 2008.

[55] A. Fowlie et al. Constrained mssm favoring new territories: The impact of new lhc limits and a 125 gev higgs boson. *Physical Review D*, 86(7):075010, 2012.

[56] Z. Ahmed et al. Search for weakly interacting massive particles with the first five-tower data from the cryogenic dark matter search at the soudan underground laboratory. *Phys. Rev. Lett*, 102(011301):0802–3530, 2009.

[57] D. Akimov et al. Wimp-nucleon cross-section results from the second science run of zeplin-iii. *Physics Letters B*, 709(1):14–20, 2012.

[58] E.Aprile at al. (Xenon Collaboration). Xenon100 dark matter results from a combination of 477 live days. *Phys. Rev. D 94, 122001 (2016)*, 2016.

[59] E. Aprile at al. (Xenon Collaboration). Conceptual design and simulation of a water cherenkov muon veto for the xenon1t experiment. *JINST 9, P11006 (2014)*, 2014.

[60] E.Aprile at al. (Xenon Collaboration). Xenon1t at lngs. *Proposal April*, 2010.

[61] E. Aprile at al. (XENON collaboration). Physics reach of the xenon1t dark matter experiment. *JCAP04(2016)027*, 2016.

[62] M. Aglietta et al. Muon "depth-intensity" relation measured by the lvd underground experiment and cosmic-ray muon spectrum at sea level. *Physical Review D*, 58(9):092005, 1998.

[63] M. Ambrosio et al. Measurement of the residual energy of muons in the gran sasso underground laboratories. *Astroparticle physics*, 19(3):313–328, 2003.

[64] The Geant4 Collaboration. Geant4 user's guide for application developers. version: geant4 9.6.0, 2012.

[65] P. Antonioli, C. Ghetti, E. V. Korolkova, V. A. Kudryavtsev, and G. Sartorelli. A Three-dimensional code for muon propagation through the rock: Music. *Astropart. Phys.*, 7:357–368, 1997.

[66] C. Patrignani et al. (Particle Data Group). Pdg, 2016.

[67] Brian Aull et al. Geiger-mode avalanche photodiodes for three-dimensional. *Imaging Lincoln Laboratory Journal*, 2002.

[68] SensLight. Introduction to the sipm. Technical report, 2011.

[69] P. Buzhan et al. An advanced study of silicon photomultiplier. *ICFA Instrumentation Bulletin.*

[70] Guillaume Plante. The xenonnt project. In *Dark Matter 2016 - UCLA - February 19, 2016*, 2016.

[71] D. S. Akerib et al. Lux-zeplin (lz) conceptual design report. 2015.

[72] Sandro D'Amato. Characterization of silicon photomultiplier arrays in liquid xenon and development of dedicated read-out electronics. master thesis, University of Zurich Department of Physics, 2016.

[73] Y. Wei (Xenon Collaboration). Internal communication. Technical report, 2016.